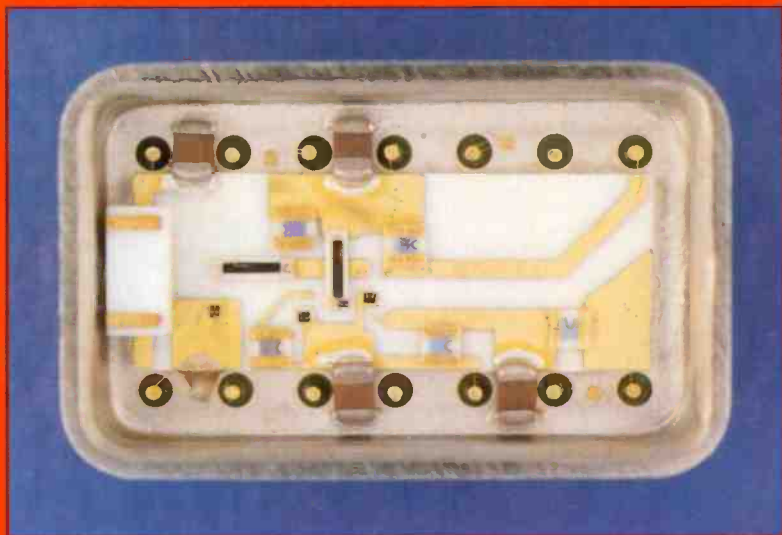


RCA

Review

PIN FET Optical Receiver



March 1984 Volume 45 No. 1

RCARCI 45(1) 1-173 (1984)

Cover: The photo shows an optical receiver module suitable for use in high speed (200-500 Mbits/s) optical communications systems. The receiver is in a hermetic 14-pin DIP package. It and a technique for receiver sensitivity measurement that will be useful in future optical communications work are described in the paper by Siegel and Channin in this issue of *RCA Review*.

RCA Review, published quarterly in March, June, September, and December by RCA Laboratories Princeton, New Jersey 08540. Entered as second class matter July 3, 1950 under the Act of March 3, 1879. Second-class postage paid at Princeton, New Jersey, and at additional mailing offices. Effective January 1, 1983, subscription rates as follows: United States: one year \$12.00, two years \$21.00, three years \$27.00; in other countries: one year \$14.00, two years \$24.50, three years \$31.50. Single copies up to five years old \$5.00

Contents

- 3 PIN-FET Receiver for Fiber Optics**
S. A. Siegel and D. J. Channin
- 23 The Effect of Carrier-Induced Index Depressions on Fundamental-Transverse-Mode Characteristics in DH Laser Structures**
D. Botez
- 33 Low Expansion Porcelain Coated Copper-Clad Invar Substrates**
K. W. Hang, A. N. Prabhu, J. Andrus, S. M. Boardman, and L. S. Onyshkevych
- 49 A Novel Memory Device for VLSI E²PROM**
S. T. Hsu
- 58 A Study of the Etching Kinetics of Low Carbon Steel Using the Ferric Perchlorate-Perchloric Acid System as a Model**
R. B. Maynard, J. J. Moscony, and M. H. Saunders
- 73 Ferric Chloride Etching of Low Carbon Steels**
R. B. Maynard, J. J. Moscony, and M. H. Saunders
- 90 Interaction with Metal Films on Glass: A New Method for Evaluating Solder Parameters**
S. Tosima, S. Harada, and E. O. Johnson
- 109 Extending the Content and Expanding the Usefulness of the Simple Gaussian Lens Equations—Part 3-A**
L. T. Sachtleben
- 165 Patents**
- 168 Authors**

RCA Corporation

Thornton F. Bradshaw Chairman and Chief Executive Officer
Robert R. Frederick President and Chief Operating Officer

Editorial Advisory Board

Chairman, K. H. Powers RCA Laboratories
J. K. Clemens RCA Laboratories
G. C. Hennessy RCA Laboratories
J. Kurshan RCA Laboratories
B. J. Lechner RCA Laboratories
R. D. Lohman RCA Laboratories
W. J. Merz Laboratories RCA, Ltd.
J. L. Miller RCA Laboratories
A. Pinsky RCA Laboratories
R. E. Quinn RCA Laboratories
C. C. Richard International Licensing
W. M. Webster RCA Laboratories
B. F. Williams RCA Laboratories

Editor **Ralph F. Ciafone**

Assoc.

Editor **Rita L. Strmensky**

Editorial Representatives

H. N. Crooks "SelectaVision" VideoDisc Operations
D. R. Higgs Missile and Surface Radar
E. Janson Consumer Electronics Division
M. Kaminsky RCA Service Company
T. E. King Engineering
E. Madenford Video Component and Display Division
R. Mausler National Broadcasting Company
M. G. Pietz Advanced Technology Laboratories
M. Rosenthal American Communications
J. Schoen Solid State Division
W. S. Sepich Commercial Communications Systems Division
D. Tannenbaum Government Communications Systems
D. Unger Global Communications
F. Yannotti Astro-Electronics

© RCA Corporation 1984. All rights reserved, except that express permission is hereby granted for the use in computer-based and other information-service systems of titles and abstracts of papers published in RCA Review.

PIN-FET Receiver for Fiber Optics

S. A. Siegel and D. J. Channin
RCA Laboratories, Princeton, NJ 08540

Abstract—This paper describes the development of a high performance PIN-FET transimpedance optical receiver module suitable for use in high speed (200–500 Mbit/s) optical communications systems. A flexible design approach was required to meet the diverse performance requirements of local area networks, emphasizing versatility of line codes and broad bandwidth, and to meet the high sensitivity and dynamic range requirements of long haul telecommunications systems. The paper reviews the optical receiver design and performance measurement techniques from a practical point of view and discusses the fabrication and testing of prototype hybrid circuits that meet all proposed design goals. The circuit was assembled in a hermetic DIP package and achieved an optical sensitivity of -35 dBm with a 250 MHz 3-dB rf bandwidth and a 20-dB dynamic range.

1. Introduction

This paper describes the development of a high performance PIN-FET transimpedance optical receiver module suitable for use in high speed (200–500 Mbit/s) optical communications systems. Optical receiver design and performance measurement techniques are reviewed from a practical point of view and the fabrication and testing of prototype hybrid circuits are discussed.

Particular attention is paid to optical sensitivity measurements. The sensitivity of an optical receiver is frequently measured in terms of its bit error rate (BER), which is the ratio of information bits correctly identified to the total number of bits transmitted. BER measurements are made with commercially available data generator/error detector test sets. As measured by this equipment, BER is really a *system* performance criteria in that such measurements

are sensitive not only to distortions of the data imposed by the receiver but to distortions imposed by the transmitter and the optical transmission system. It is useful to infer the optical sensitivity for a receiver directly from signal-to-noise (SNR) measurements, eliminating transmitter and transmission induced distortions. This data can be obtained at any transmission frequency with a spectrum analyzer and an oscilloscope. The calculation of receiver sensitivity from SNR has been described in detail by Smith and Personick¹ as well as others; our interest for this work was to relate this theory to an actual measurement technique applicable to the evaluation of the high speed receivers developed in this program.

2. Receiver Design

The design of an optical preamplifier suitable for use in high speed digital communication systems must offer wide bandwidth, large dynamic range, and low noise. The circuitry immediately following the photodiode is critical for achieving these goals. There are essentially three major front-end design approaches:

- (1) Terminate the photodiode with a simple load resistor.
- (2) Terminate the photodiode with a high impedance (i.e., the so-called integrating front-end).
- (3) Employ a transimpedance or negative feedback design.

A simplified input noise model for an optical receiver appears in Fig. 1. The total mean-square noise current appearing at the receiver input is the sum of three noise sources: the Johnson noise current (I_R) associated with the input resistance R_L , and the device leakage currents (I_{L1}) and (I_{L2}) associated with the photodiode and amplifier input noise, respectively. We can write

$$\langle i \rangle_{total}^2 \cong \frac{4KTB}{R_L} + 2qI_{L1}B + \frac{4KTB(2\pi B)^2 C_i^2}{g_m}, \quad [1]$$

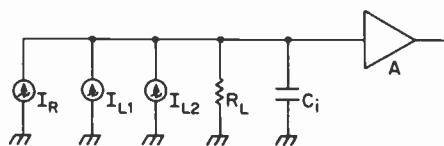


Fig. 1—Input noise model for optical receiver.

where B is the bit rate, K is Boltzman's constant, and C_i represents the total input capacitance seen by the amplifier A . Here,

$$C_i = C_d + C_{gs}, \quad [2]$$

where C_d is the photodiode device capacitance and C_{gs} is the FET gate-source input capacitance. Typically, $C_d \sim 0.5$ pF and $C_{gs} < 0.5$ pF. The third term in Eq. [1] is the gate leakage current for a GaAs FET input stage.²

The noise contribution due to the last two terms is minimized by choosing a GaAs FET with large transconductance (g_m) and small gate-source capacitance and a photodiode with small device capacitance and low dark current (I_{L1}). Thus, in practice, the total input noise is dominated by the thermal noise of the input resistor.

The simplest front-end design would be to choose an input load resistor so that

$$R_L < \frac{1}{2\pi BC_i} \quad [3]$$

which ensures that the bandwidth of the receiver is comparable to the data rate B . This requires minimizing C_i and choosing the lowest possible value for R_L . The following two techniques relax the constraints on R_L imposed by Eq. [3], thus increasing its value and reducing the noise as given by Eq. [1].

One approach is to ignore Eq. [3] and make R_L very large, e.g., on the order of a few megohms. This is the integrating front-end design in which the input admittance is dominated by the capacitance C_i which appears to integrate the received signals.³ The signal distortion imposed by this integration can be corrected by use of suitable equalization circuitry at the output of the receiver. The design of such circuitry is not straightforward, as the degree of equalization necessary depends on the input signal frequency spectrum and thus upon the data coding format as well. Another problem with high impedance front-ends is that dynamic range is reduced, because large voltages can appear across R_L even with relatively small photocurrents. This voltage could saturate subsequent input stages unless compensating bias circuitry is included in the design.

The second approach is the transimpedance or negative-shunt-feedback front-end. This is the design chosen for this work and indeed is the most commonly employed receiver configuration for optical fiber systems. The advantages of the transimpedance approach are a wide flat bandwidth, high dynamic range, and good noise

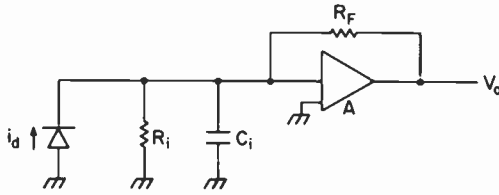


Fig. 2—Transimpedance circuit model.

performance. Fig. 2 shows a simplified transimpedance circuit model. C_i again represents the total input capacitance seen by the amplifier and R_i is now the open-loop resistance of the amplifier 1st stage. R_F is the feedback resistance providing the transimpedance function. The amplifier transimpedance is the current-to-voltage transfer function $T(\omega)$:

$$T(\omega) = \frac{R_F}{1 + j\omega \left(\frac{C_i R_L}{A} \right)}, \quad [4]$$

where

$$\frac{1}{R_L} = \frac{1}{R_i} + \frac{1}{R_F}. \quad [5]$$

The 3-dB cutoff frequency is

$$\omega_{3dB} = \frac{A}{R_F C_i}, \quad [6]$$

where A is the closed-loop voltage gain.⁴ For a practical receiver, $R_i \gg R_F$ and R_L is effectively equal to R_F . Comparing Eqs. [6] and [3] shows that, for a given bandwidth, R_F can be made effectively A times larger than the load resistor R_L in the simple resistive termination approach, with a corresponding decrease in thermal noise. Circuit optimization, thus, consists of choosing the largest value of R_L that meets the bandwidth requirement for the specified data rate. Aside from choosing low capacitance devices, minimization of the total circuit capacitance requires reducing the Miller capacitance seen by the FET, and this is accomplished by a cascade second-stage configuration. In addition, a buffer stage can be added to the output end of the feedback loop to further prevent any parasitic output capacitance from being reflected into the receiver input.

3. Theory of BER Measurement

Error probability in an optical receiver is evaluated in the presence of (1) signal dependent shot noise from the photodetector and transistor first stage, (2) Gaussian thermal noise from the net input resistant R_i , and (3) distortion due to intersymbol interference.⁵ We assume in our analysis that shot noise is minimal due to choice of a low leakage PIN photodetector and low base or gate leakage of the input bipolar or GaAs FET amplifier. We also eliminate intersymbol distortion by using a 1010 . . . data pattern as our test signal rather than a pseudorandom bit stream, and we assume a jitter-free clock recovery circuit. Thus, our analysis assumes that thermal noise dominates all input noise at the receiver and that it is well-characterized by Gaussian statistics.

Fig. 3 illustrates two types of electrical signals at the receiver input; each has a peak-to-peak voltage swing of A , but one signal rides on the 0-volt baseline while the other straddles it. The unipolar signal has a mean power of $A^2/2$ and the bipolar signal has a mean power of $A^2/4$. We shall let σ^2 represent the mean noise power in each case. Then, for the unipolar signal,

$$\text{SNR} = \frac{A^2}{2\sigma^2}, \quad [7]$$

and for the bipolar signal,

$$\text{SNR} = \frac{A^2}{4\sigma^2}. \quad [8]$$

In general

$$\text{SNR} = \alpha \frac{A^2}{4\sigma^2}. \quad [9]$$

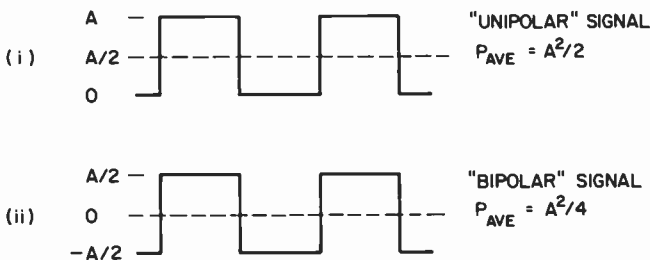


Fig. 3—Unipolar and bipolar signals. The dashed lines represent the decision threshold level.

We can define a decision level, represented by the dashed line in Fig. 3, above which the signal is high and below which the signal is low. The presence of noise in the actual received signal creates a probability of error in defining the state of the signal at a given time. We assume each state can be characterized by a probability density function (PDF) with Gaussian statistics. The total probability of an error, i.e., when either a high state or low state is incorrectly identified, is found by integrating the area where the two PDFs overlap.

Let us define a parameter Q such that

$$Q = \frac{|D - S|}{\sigma}, \quad [10]$$

where D is the decision level voltage, S the expected peak signal voltage, and σ the standard deviation of voltage level. Personick⁶ gives the probability of error, $P_{(E)}$, as

$$P_{(E)} = \frac{1}{\sqrt{2\pi}} \int_Q^\infty e^{-x^2/2} dx \sim \frac{1}{\sqrt{2\pi}Q} e^{-Q^2/2}. \quad [11]$$

The approximation can be written in a more useful form as

$$P_{(E)} = \frac{1}{2} \left[1 - \operatorname{erf} \frac{Q}{\sqrt{2}} \right]. \quad [12]$$

Since the dashed line in Fig. 3 represents the decision level, then for both unipolar and bipolar signals

$$Q = \frac{A}{2\sigma}. \quad [13]$$

It follows that for a unipolar signal, equating Eqs. [7] and [13] gives

$$\text{SNR} = 2Q^2, \quad [14]$$

and for a bipolar signal

$$\text{SNR} = Q^2. \quad [15]$$

For an arbitrary signal,

$$\text{SNR} = \alpha Q^2. \quad [16]$$

Most commercial receivers have an optical sensitivity specified for a BER (or $P_{(E)}$) of 1×10^{-9} . Eq. [12] gives a value of $Q = 6$ for a $P_{(E)}$ of 1×10^{-9} . If we use this value for Q , simple substitution gives SNR ratios of 18.6 dB and 15.6 dB for unipolar and bipolar signals, respectively. These figures represent the minimum SNR required to achieve a 1×10^{-9} BER.

The general procedure for measuring receiver sensitivity would be to attenuate the received optical signal until the SNR becomes $SNR_{min} = 10 \log(36\alpha)$ dB. [17]

The optical power at which SNR_{min} is obtained is the receiver sensitivity for an equivalent 1×10^{-9} BER.

For determining a receiver's sensitivity it is necessary to relate the BER to average optical power. For a PIN photodiode detector, the optical power P is related to the detector photocurrent i_p by⁷

$$P = \left(\frac{h\nu}{nq}\right) i_p = \frac{1}{R} i_p \tag{18}$$

where $h\nu/q$ is the photon energy in eV, n is the quantum efficiency, and R is the photodetector responsivity. The average optical power (at a 50% duty cycle) required to achieve an error rate as defined by the parameter Q , and thus by the SNR, is

$$P_{ave} = \frac{1}{R} Q[\langle i^2 \rangle]^{1/2}, \tag{19}$$

where $\langle i^2 \rangle$ is the mean-square noise current. If we assume that signal-dependent noise contributions are negligible compared to circuit noise, then $\langle i^2 \rangle$ is equal to the receiver front-end noise expressed in Eq. [1]. In a transimpedance receiver with R_F the dominant input resistance,

$$\langle i^2 \rangle = \frac{\sigma^2}{R_F}. \tag{20}$$

4. Technical Approach

Two circuit configurations were chosen for initial development. The first is a two-stage design incorporating an FET input stage followed by a bipolar emitter-follower output stage. This output configuration produces a low output impedance compatible with 50-ohm systems (Fig. 4). The feedback path in this circuit is ac coupled

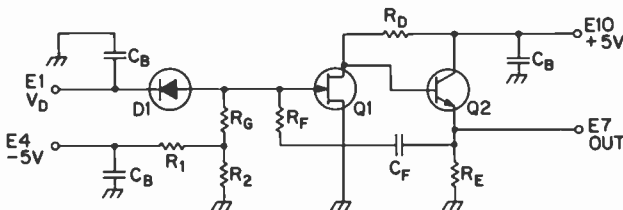


Fig. 4—Schematic diagram of two-stage optical receiver.

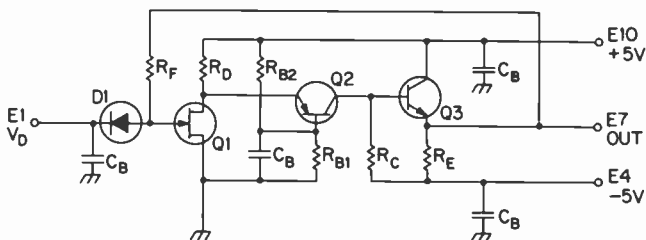


Fig. 5—Schematic Diagram of three-stage optical receiver.

to allow setting the dc bias levels of the two transistors independently. Because of this feature, this design was our basic testbed for determining optimal bias points for the various FETs evaluated.

The second circuit, shown in Fig. 5, is based on a well-known three-stage design.⁸ The common base second-stage configuration of the PNP bipolar transistor minimizes the Miller capacitance seen by the FET and produces a high open-loop gain. An emitter-follower output stage is again used to provide a low output impedance. Since this circuit employs a dc coupled feedback path, the dc voltage at the emitter of Q_3 is equal to the gate voltage of Q_1 . Hence both devices must be biased at proper levels to meet this constraint.

Bandwidth measurements were made by modulating a laser diode with a small rf signal and coupling its output light to the receiver photodiode via a one-meter length of mode-stripped optical fiber. As the rf signal was manually swept from a few kHz to 500 MHz, the output of the receiver was fed to an HP storage spectrum analyzer and recorded. The two-stage circuit with a 510-ohm feedback resistor (R_F) had a 200-MHz 3-dB bandwidth, while the three-stage design gave the same bandwidth with R_F twice as large.

The open-loop and closed loop frequency responses of the three-stage circuit are compared in Fig. 6. The closed loop waveforms were taken with R_F connecting the emitter of Q_3 to the gate of Q_1 (transimpedance mode). The open loop waveforms were obtained with the same feedback resistor now supplying a bias voltage to the gate of Q_1 (i.e., one end of R_F is now in ac ground). The photos demonstrate the performance that would be expected from an integrating type receiver with an input impedance equal to the feedback resistance of the transimpedance configuration.

The open-loop voltage gain (A_o) was obtained by applying an rf signal to the gate of the FET through a large (about 3 kilohm) resistance and measuring the amplitude of the receiver output. This measurement was made with the feedback resistance disconnected and the gate of the FET biased through a 10-kilohm resistor. A_o

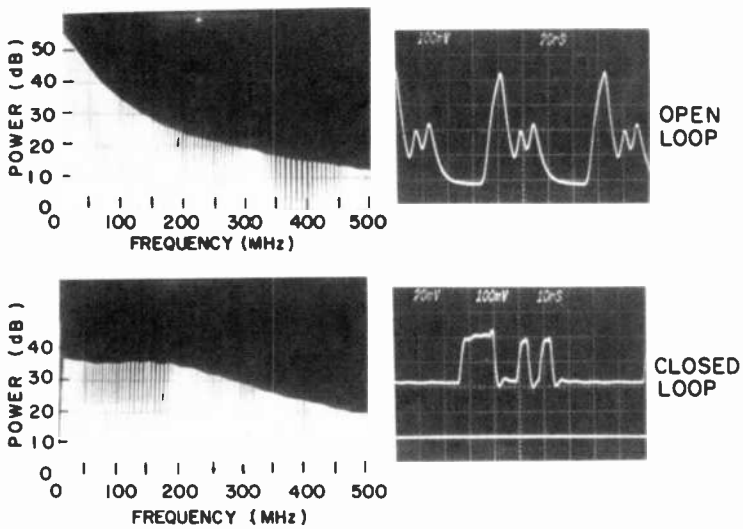


Fig. 6—Optical transimpedance receiver comparing open-loop and closed-loop frequency and pulse response.

was about 12 for the two-stage circuit and 16 for the three-stage cascade. Evidently the reduction of the Miller capacitance in the cascade design as well as its greater open-loop gain contributed to its greater bandwidth.

The breadboard circuits allowed easy component substitution. Fig. 7 shows the optical sensitivity of the two-stage circuit for various values of R_F . (A detailed discussion of sensitivity measurement appears below.) The data rate for each measurement was chosen to be within the 3-dB bandwidth of the receiver at each data point taken. At a data rate of 150 Mbit/s and 500-ohm feedback resistance, the two-stage circuit had an optical sensitivity of -31.5 dBm for return-to-zero (RZ) data formats and -30 dBm for nonreturn-to-zero (NRZ) formats. This performance was comparable to existing commercially available receiver modules, such as the RCA C30952G, that were evaluated during this program.

The data indicates how sensitivity increases as R_F increases due to a corresponding decrease in front-end noise. It is also evident that the bandwidth decreases with R_F , as predicted by Eq. [6]. Thus a substantial reduction in circuit capacitance is necessary to produce the broadest possible bandwidth with a large value of feedback resistance. Circuit development proceeded with low-capacitance hybrid circuits incorporating chip components mounted on alumina substrates.

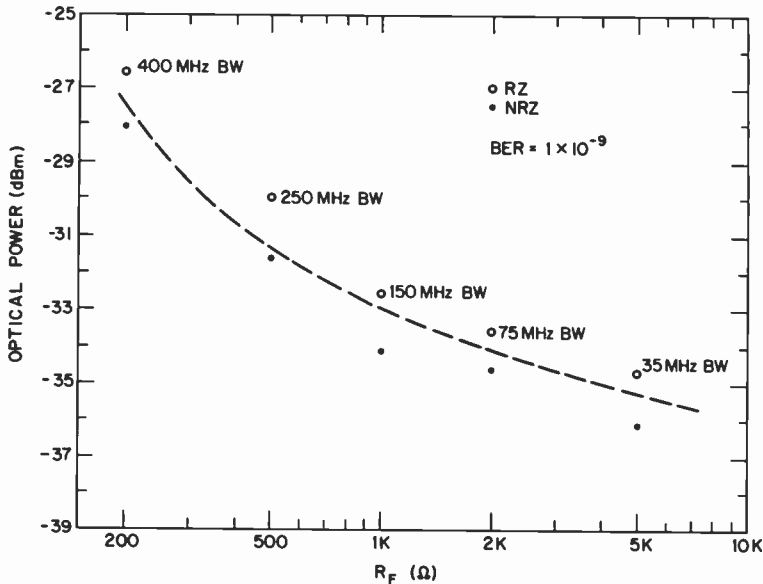


Fig. 7—Optical sensitivity of the two-stage circuit for various values of feedback resistance. The receiver 3-dB bandwidth is shown for each sensitivity measurement.

5. Sensitivity Measurements

Sensitivity measurements were performed by two methods. The first employs a Hewlett Packard 3762A/3763A data generator and error detector test set. This equipment is restricted to a maximum data rate of 150 Mbit/s. The second method infers receiver sensitivity from SNR data. While there is no restriction on data rate here, measurements were kept to 150 Mbit/sec and below so that results from both methods could be compared.

In both cases a repeating 1010 . . . word in RZ and NRZ formats was used in the tests, since at the time the measurements were made, our system lacked the level detection circuitry necessary for tracking data streams with varying dc levels such as a pseudo-random bit stream (PRBS). Optical signal power for these measurements was calculated from the known responsivity of the photodiode and the average small-signal photocurrent measured with a microammeter.

Signal power measurements were made by displaying the receiver output waveform on a spectrum analyzer and recording the power in the fundamental of the signal. Fig. 8 illustrates the appearance of the signal. Evidently, the power in the fundamental,

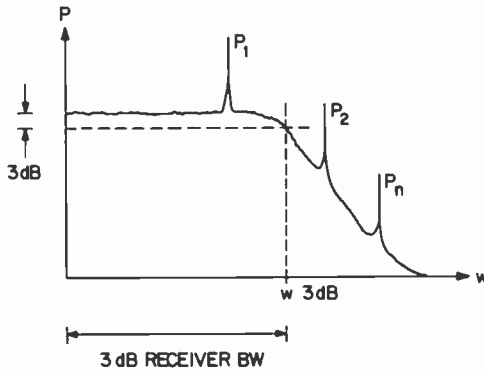


Fig. 8—Approach used for signal-to-noise measurement. Noise is normalized to 3-dB bandwidth and P_1, P_2, \dots, P_n are power harmonics. Signal power is defined as the power in the fundamental (P_1).

P_1 , dominates the total signal power in the 3-dB bandwidth of the receiver. We define the signal power for a 30-Mbit/s 1010 . . . data stream as the power in the 15-MHz fundamental (P_1). To verify this method, the average signal power was also calculated by integrating the receiver output waveforms as displayed on an oscilloscope. The results by the two methods differ by no more than 2 dB even in the case of distorted waveshapes with varying harmonic content (Fig. 9).

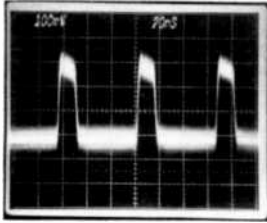
The average receiver output noise relative to the signal level was measured on a spectrum analyzer and was normalized to the 3-dB bandwidth of the receiver:

$$\text{Normalized noise} = \text{Ave. noise} + 10 \log \left[\frac{3\text{dB RCVR BW}}{(C_1)(\text{analyzer BW})} C_2 \right] \quad [21]$$

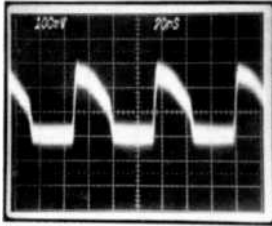
where C_1 and C_2 are spectrum analyzer correction factors.

This scheme is justified in a system where only the first harmonic of the input signal falls within the receiver 3-dB bandwidth. Fig. 10 shows bit error rates plotted for signal-to-noise ratios obtained for RZ and NRZ signals at 150 Mbit/s. For test purposes the receiver used for the measurement was an RCA C30952G wideband unit with a silicon PIN detector. The solid and dashed lines represent theoretical curves based on bipolar and unipolar signal formats, respectively. The curves were produced by using Eq. [12] and Eq. [16] to relate the SNR to Q with the parameter $\alpha = 1$ for bipolar signals, and $\alpha = 2$ for unipolar signals.

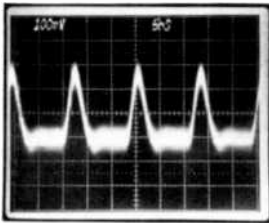
The average measured optical power for an 18.6-dB SNR (assuming $\alpha = 2$) was -27.8 dBm for Fig. 10. This number then rep-



(i)
 1^{st} HARMONIC POWER = +12 dBm
 AREA INTEGRAL = +14 dBm



(ii)
 1^{st} HARMONIC POWER = +14 dBm
 AREA INTEGRAL = +13 dBm



(iii)
 1^{st} HARMONIC POWER = +11 dBm
 AREA INTEGRAL = +12 dBm

Fig. 9—Determining signal power for three different waveshapes by comparing power in the first harmonic to the area integral.

resents the receiver's optical sensitivity for an equivalent 1×10^{-9} BER at this data rate.

At this data rate, it appears that the unipolar format fits the data best. This was an unexpected result in the case of the NRZ coding format, which should have a 50% duty cycle and thus in a capacitively coupled system should appear as a bipolar signal. Fig. 9 shows, however, that the actual data is slightly distorted and exhibits a duty cycle that makes it appear more like a unipolar signal. It is evident then that the BER data generated by the test set is sensitive to the transmitted waveshape and does not directly indicate the performance of the receiver alone. An accurate measurement of receiver sensitivity must take into account distortion of the transmitted optical signal. Since no real signal is perfectly unipolar or bipolar the best data fit would be obtained by choice of an α appropriate to the exact waveshape transmitted.

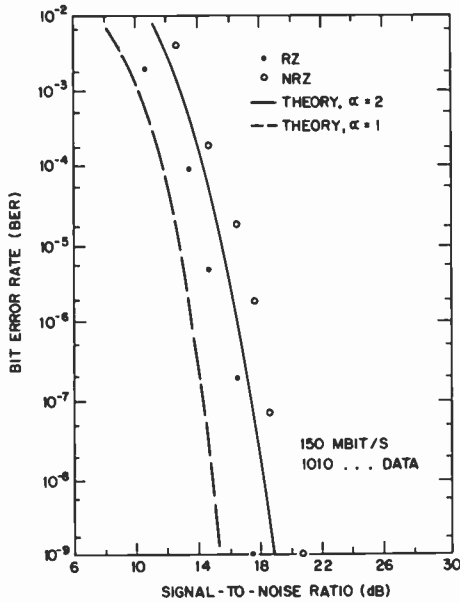


Fig. 10—Bit error rate as a function of signal-to-noise ratio at 150 MBit/s for RZ and NRZ data formats.

Fig. 11 shows BER plotted as a function of optical power for RZ and NRZ signals at 30 MBit/s. The receiver used was again the RCA C30952G unit. The data points were obtained with the Hewlett-Packard BER test set, and optical power was calculated from the responsivity of the photodiode and the average small-signal photocurrent. The solid lines are theoretical curves fit to a value for $\langle i^2 \rangle$ inferred from Eq. [19] at the 1×10^{-9} BER threshold where $Q = 6$.

6. Hybrid Design and Performance

Alumina substrates sized to fit inside a standard 14-pin DIP package and utilizing chip components were fabricated. All circuits were of the three-stage configuration. The circuits were assembled with the PIN diode mounted on a ceramic block perpendicular to the alumina substrate and positioned behind a glass window soldered to one end of the DIP package. This window allows light from an optical fiber or other source to couple to the photodetector while maintaining hermeticity. The hybrid circuits used a modified circuit layout that could accommodate an additional output buffer stage

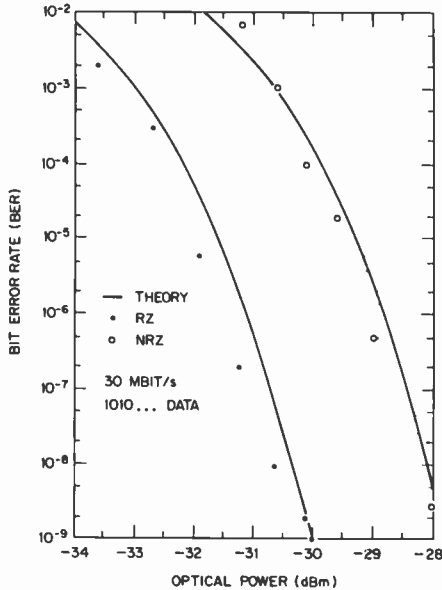


Fig. 11—Bit error rate as a function of average optical power at 30 MBIT/s for RZ and NRZ data formats.

(Q_4), as well as allow space for screen-printed thick-film resistors (all circuits to date, however, have used chip resistors). The feedback resistor in all cases was 4.7 kilohms. Fig. 12 is a photograph of an open DIP package.

7. Hybrid Performance

(A) Bandwidth

The nine prototype circuits constructed had 3-dB rf bandwidths ranging from 170 to 220 MHz. It was found that bandwidth variation was due to choice of the FET input stage, and one manufacturer's device (NEC) consistently gave 3-dB bandwidths of between 200 and 220 MHz, due apparently to a low C_{gs} .

(B) Dynamic Range

The range of optical power over which the receiver could detect a signal barely above the noise threshold, with a 10^{-9} bit error rate (BER) to the point where the receiver output was distorted by 10%

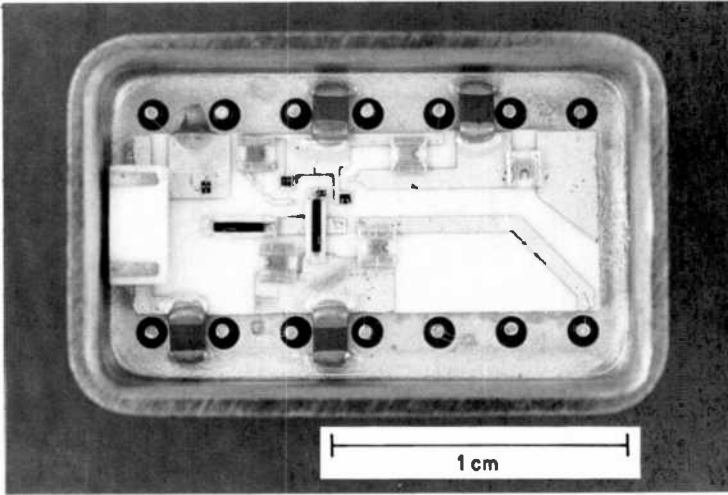


FIG. 12—Open hermetic 14-pin DIP package with hybrid circuit.

was typically 20 dB. A 150 MHz sinewave test signal was used for the test.

(C) Receiver Dark Noise

Dark noise measurements were made by comparing the receiver output noise power to a calibrated excess noise source (ENS). The data was then plotted as an output noise voltage normalized to a 1-Hz bandwidth. In all cases the output noise peaked at a frequency approximately equal to the 3-dB cutoff frequency. This peak was initially as high as $27 \text{ nV}/(\text{Hz})^{1/2}$ but was reduced to less than $20 \text{ nV}/(\text{Hz})^{1/2}$ in optimized circuits (see Fig. 13). Optimization was accomplished by carefully trimming R_c to reduce excess base current drive of Q_3 and still keeping the device active.

(D) Sensitivity

The optical signal power required for a 1×10^{-9} BER varied between -33 and -35 dBm for the nine circuits tested. RZ and NRZ results were comparable in all cases. Fig. 14 is a typical sensitivity plot for an optimized circuit. The curve represents theoretical performance based on the SNR measurement and assuming a bipolar ($\alpha = 2$) input signal.

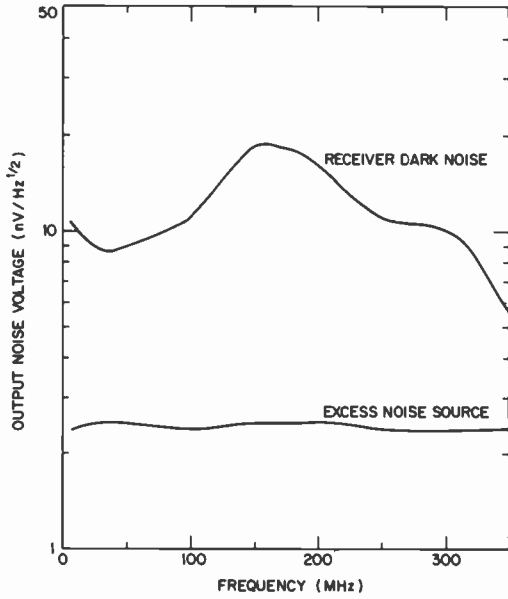


Fig. 13—Dark noise of three-stage receiver. The noise peak occurs near the receiver 3-dB bandwidth.

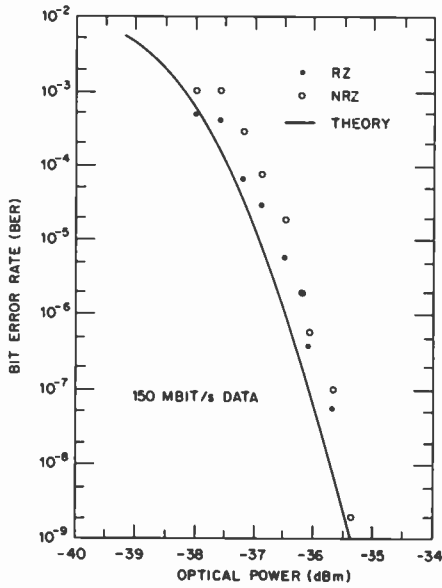


Fig. 14—Optical sensitivity of three-stage hybrid receiver for 150 Mbit/s RZ and NRZ data.

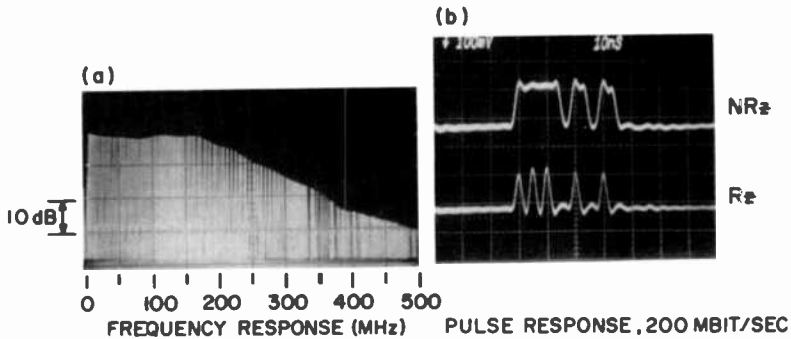


FIG. 15—Three-stage receiver performance: (A) frequency response and (B) NRZ and RZ data fidelity.

Fig. 15 shows the frequency response and data output of an optimized hybrid circuit.

8. Further Optimization

As stated previously, the revised circuit layout could accommodate an additional output buffer stage (Q_4). Fig. 16 is a schematic illustrating how Q_4 would be configured. It was felt that a transistor placed outside the feedback loop would effectively prevent any parasitic shunt capacitance at the receiver output from appearing, via the feedback resistor, at the receiver input. This would have the effect of increasing the receiver bandwidth and thus allow a higher value feedback resistance for a corresponding gain in sensitivity. In addition, Q_4 would make the output impedance virtually independent of variations in circuit component values and therefore more stable.

With Q_4 in the circuit and R_F remaining at 4.7 kilohms, the 3-dB bandwidth was increased to 300 MHz. The 150 Mbit/s sensitivity

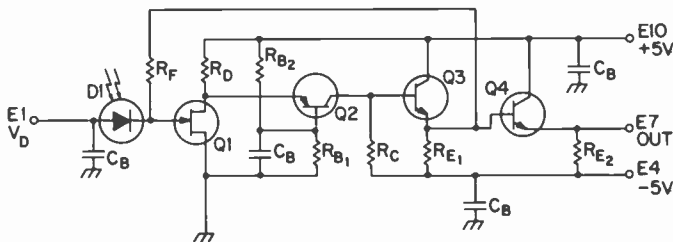


Fig. 16—Schematic of four-stage circuit showing buffer stage Q_4 .

was -33 dBm, a decrease of about -2 dBm from the optimized circuits without Q_4 . The sensitivity increased to between -35 and -36 dBm when R_F was increased to 10 kilohms. The circuit dynamic range remained unchanged.

The addition of Q_4 significantly reduced the hybrid's parasitic capacitance. Fig. 17 shows that the receiver bandwidth varies for different values of feedback resistance in the three-stage (dashed line) and four-stage (solid line) circuits. Note that for a given value of R_F the four-stage circuit has the greater bandwidth and that the difference between bandwidths becomes larger as the feedback resistance increases. The total circuit capacitance represented by the dashed line is about 0.13 pF per unit of closed-loop gain and by the solid line is 0.05 pF per unit of closed-loop gain. Thus, by adding Q_4 , the total circuit parasitic capacitance has been reduced by more than half. Fig. 18 shows the frequency response and output data response for the four-stage circuit.

9. Conclusion

The result of this program has been the design, fabrication, and testing of a versatile receiver-preamplifier module whose specifications meet the broad requirements of high performance fiber-optic systems. We have also successfully developed a technique for re-

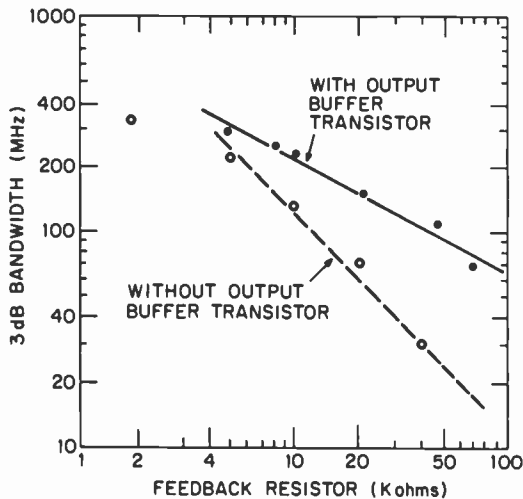


FIG. 17—Effect of buffer transistor Q_4 on three-stage performance.

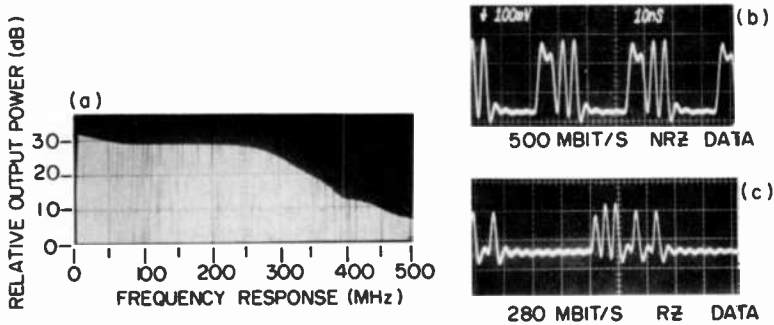


Fig. 18—Four-stage receiver performance: (A) frequency response, (B) 500 MBit/s NRZ data, and (C) 280 MBit/s RZ data.

ceiver sensitivity measurement that will be useful in future optical communications work.

The overall performance of the receiver developed is

- 300 MHz bandwidth
- 20 dB dynamic range
- -35 dBm optical sensitivity at 250 MHz bandwidth for a 1×10^{-9} BER
- 50 Ω compatible output impedance
- DIP package, hermetically sealed with fiber optic pigtail
- ± 5 volt operation
- Broadband PIN detector used (0.9 - 1.7 μm)

The receiver design can be tailored for a specific application, such as a wider bandwidth or greater sensitivity, and it can accommodate APD as well as PIN detectors. The module is also attractive for military applications requiring a hermetic package.

Acknowledgments

The work discussed here was part of joint efforts by RCA Laboratories in Princeton and RCA Electro Optics in Montreal to develop a fiber optic communications receiver for commercial applications, and a parallel effort by RCA Government Communications Division in Camden to develop components for military and government requirements. Close collaboration with the Montreal personnel, especially L. Cooke, B. Dion, S. Soltés, and R. Cardinal, was essential to the success of the program. Appreciation is expressed for substrate fabrication by R. J. Menna, assembly by S. P. Grober, and helpful advice from R. E. Askew.

References:

- ¹ *Semiconductor Devices for Optical Communications*, H. Kressel, Ed., Vol. 39, pp. 112–117, Springer-Verlag, Berlin (1980).
- ² See Ref. [1], pp. 112–117.
- ³ See Ref. [1], p. 125.
- ⁴ J. L. Hullett, S. Moustakas, "Optimum Transimpedance Broadband Optical Preamplifier Design," *J. Optical and Quantum Electronics*, 13, p. 65 (1981).
- ⁵ G. L. Cariolaro, "Error Probability in Digital Fiber Optic Communication Systems," *IEEE Trans. Information Theory*, IT-24, No. 2, p. 213 (1978).
- ⁶ See Ref. [1], p. 134.
- ⁷ G. Keiser, *Optical Fiber Communications*, p. 149, McGraw-Hill Book Co., New York (1983).
- ⁸ K. Ogawa, E. L. Chinnock, "GaAsFET Transimpedance Front End Design for a Wideband Optical Receiver," *Electron. Lett.*, 15, No. 20, p. 650, 27 Sept. 1979.

The Effect of Carrier-Induced Index Depressions on Fundamental-Transverse-Mode Characteristics in DH Laser Structures

D. Botez

RCA Laboratories, Princeton, NJ 08540

Abstract—Simple closed-form analytical approximations are found for the relative variations in transverse field-intensity confinement factor, Γ ; transverse field-amplitude confinement factor, b ; effective refractive index, N_{eff} ; and transverse beamwidth, θ_{\perp} , all as a function of Δ_r , the carrier-induced relative change in the dielectric-constant step of symmetric DH laser structures. The derived expressions are correct within 2% for Δ_r values as low as -30% . The effect of carrier-induced index depressions is strongest for thin-active-layer structures. The effect of Δ_r on asymmetric DH structures is also discussed. The analysis explains commonly observed experimental results from thin-active-layer ($d < 0.15 \mu\text{m}$) laser structures: the threshold current density increases faster than expected (with decreasing d); the transverse beam is narrower than expected; and slight asymmetries in DH structures can cause serious threshold increases.

Introduction

Recently, it has been found that changes in dielectric constant induced by the injected carriers in diode lasers are about an order of magnitude larger than previously thought. The bulk refractive index in the active layer is depressed by a quantity δn_1 , which is mainly due to shifts in the absorption edge with increasing injected-carrier concentration.¹⁻⁴ For AlGaAs/GaAs double-heterojunction^{2,3} (DH) and large-optical-cavity⁵ (LOC) laser structures, δn_1 at threshold is found to take values in the -0.015 to -0.06 range

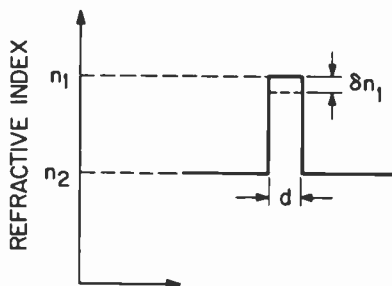


Fig. 1—Schematic representation of the transverse refractive-index profile in a symmetric DH laser structure. δn_1 is the carrier-induced dielectric-constant depression.

with the majority of values falling in the -0.02 to -0.03 range. For InGaAsP/InP DH^{3,6} and LOC^{4,7} laser structures, δn_1 at threshold is found to take values in the -0.03 to -0.10 range, with the majority of values falling in the -0.04 to -0.06 range. Such index depressions are not negligible when considering that index steps in DH structures are in the 0.2 to 0.4 range. For instance, for Al_{0.3}Ga_{0.7}As/GaAs DH structures, Kressel et al⁸ have reported an index step of $\cong 0.18$ measured on active devices, while Casey et al⁹ claimed an index step of 0.21 based on index measurements on passive material. The discrepancy can now be attributed to the carrier-induced index depression present in active devices.

It has already been shown that for LOC-type structures,⁵ where the index step between the active- and guide-layers is relatively small (i.e., 0.10 – 0.15), carrier-induced index depressions can significantly change the (lateral) effective-index profile and thus affect lateral mode discrimination and control.¹⁰ The purpose of this paper is to study the effect of carrier-induced index depressions on the key waveguiding parameters for the fundamental transverse mode (i.e., in the plane perpendicular to the junction) in DH-type laser structures: the field-intensity confinement factor, Γ ;¹¹ the field-amplitude confinement factor, b ;¹² and N_{eff} , the effective refractive index.^{11,13} Closed-form expressions are derived for the relative variations in Γ , b , N_{eff} and the transverse beamwidth, θ_{\perp} , as a function of relative variations in dielectric-constant step. Also presented is a discussion of the effect of index depressions on mode confinement in asymmetric DH laser structures.

Effect on Key Waveguiding Parameters

In Fig. 1 we show schematically the symmetric DH structure considered. Calculations are done only for the TE₀ mode, since it is the

most common mode of diode-laser operation. For the TM_0 mode, analytic approximations for Γ and b can be found in Ref. [14]. The parameter that best describes the DH structure in Fig. 1 is the normalized active-layer thickness, D

$$D \equiv \frac{2\pi}{\lambda} d \sqrt{n_1^2 - n_2^2}, \quad [1]$$

where d is the active-layer thickness; λ is the vacuum wavelength; and n_1 and n_2 are the refractive indices of the active- and cladding-layers, respectively. Since D is a function of the difference in dielectric constants, $\Delta\epsilon = n_1^2 - n_2^2$, it is most convenient to consider carrier-induced dielectric-constant variations rather than refractive-index variations. The following relationships are used

$$\delta\epsilon = \delta n_1^2 = 2 n_1 \delta n_1 \quad [2a]$$

$$\frac{\delta D^2}{D^2} = \frac{\delta n_1^2}{n_1^2 - n_2^2} = \frac{\delta\epsilon}{\Delta\epsilon} = \Delta_r \quad [2b]$$

where Δ_r is the relative variation in dielectric-constant step between the active and the cladding layers.

The confinement factor Γ (i.e., the percentage of the optical-mode field intensity that lies in the active layer) has been shown¹⁵ to be given by the closed-form expression

$$\Gamma \equiv \frac{D^2}{2 + D^2}, \quad 0 < D < \infty \quad [3]$$

with 1.5% maximum error. By using Eq. [2b] and differentiating Eq. [3], the relative variation in Γ caused by injected carriers can be shown to be

$$\frac{\delta\Gamma}{\Gamma} = (1 - \Gamma)\Delta_r \quad [4]$$

Eq. [4] is plotted in Fig. 2a, as a function of D and for two values of Δ_r , -10% and -20% . These Δ_r values are typical of what has been reported in literature. It can be shown that for $\Delta_r = -20\%$, Eq. [4] is at most 1% in error with respect to the exact calculation.¹⁶ Even if Δ_r were -30% , Eq. [4] is correct within 2%.

The field-amplitude confinement factor b (i.e., the percentage of the optical-mode field amplitude that lies in the active layer) is generally used as the multiplier of the dielectric-constant step in the effective-index, N_{eff} expression^{13,17}:

$$N_{eff}^2 = n_2^2 + b(n_1^2 - n_2^2). \quad [5]$$

By using a relationship between b and Γ and the Γ approximation

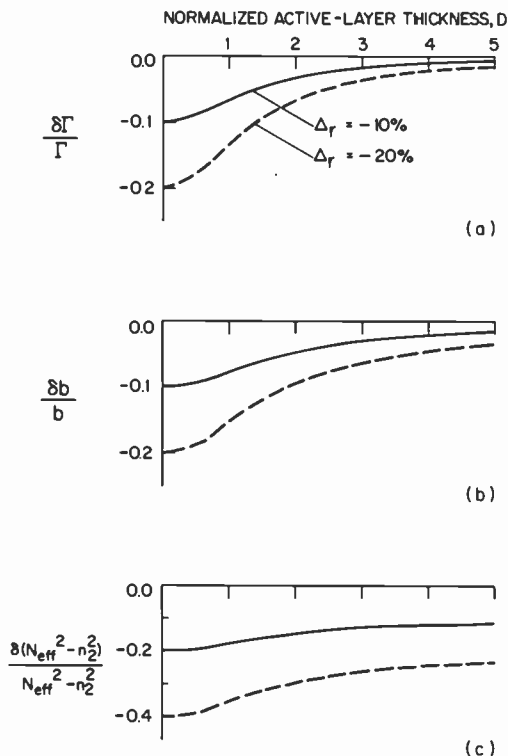


Fig. 2—The relative variations in: (a) the transverse field-intensity confinement factor Γ ; (b) the transverse field-amplitude confinement factor, b ; and (c) the difference between the effective dielectric constant and the cladding dielectric constant, for two values of Δ_r (the relative change of the dielectric-constant step in DH structures): -10% (solid line) and -20% (dashed line). These variations are shown as a function of D , the normalized active-layer thickness (for InGaAsP/InP structures $D \cong 6.6 d$ for $1.2 \mu\text{m} < \lambda < 1.6 \mu\text{m}$).

(Eq. [3]), Botez has found¹⁸ an analytical approximation for b that is accurate within 2% up to $D = 2$:

$$b \cong \frac{D^2}{4} \left(\frac{\sqrt{9 + 4D^2} - 1}{2 + D^2} \right)^2, \quad 0 < D < \pi. \quad [6]$$

More recently Chen and Wang¹⁹ have shown that by using the Γ approximation Eq. [3] and a variational technique, the b factor can be approximated within 1.2% by

$$b \cong 1 - \frac{\ln(1 + D^2/2)}{D^2/2}, \quad 0 < D < \infty. \quad [7]$$

Differentiating this expression, we find the relative b variation due to carrier-induced dielectric-constant variations:

$$\frac{\delta b}{b} = \left(\frac{\Gamma}{b} - 1 \right) \Delta_r. \quad [8]$$

These relative b variations are plotted in Fig. 2b for -10% and -20% values for Δ_r .

Finally, for lateral-mode confinement it is important to find the relative variations in effective refractive index. By differentiating Eq. [5] and using Eq. [8], we find

$$\delta N_{eff}^2 = \delta b(n_1^2 - n_2^2) + b \delta n_1^2 = \Gamma \delta n_1^2. \quad [9]$$

This is the well-known result originally proposed by Paoli²⁰ and then derived by other workers.^{13,17,21} Notice, however, that the above derivation for δN_{eff}^2 is much simpler than previously reported derivations.^{13,17,21}

When considering lateral wave confinement in a nonplanar device or buried-heterostructure device, the relevant quantity is the difference between the effective dielectric constant and the cladding-layer dielectric constant, that is, $N_{eff}^2 - n_2^2$. Its relative variation as a function of carrier-induced dielectric-constant depressions is expressed as follows:

$$\Delta(N_{eff}^2 - n_2^2) = \frac{\delta(N_{eff}^2 - n_2^2)}{(N_{eff}^2 - n_2^2)} = \frac{\Gamma}{b} \Delta_r, \quad [10]$$

where Eqs. [5] and [9] were used. Eq. [10] is plotted in Fig. 2c as a function of D for -10% and -20% values for Δ_r .

What we have succeeded in doing is to obtain simple closed-form expressions for the relative variations of Γ , b , and $N_{eff}^2 - n_2^2$ as a function of relative variations in dielectric-constant step. They are all plotted as a function of D in Fig. 2. For small D values (i.e., small d or small $n_1^2 - n_2^2$ values), the impact of the index depressions is strongest. As $D \rightarrow 0$, relative variations in Γ and b approach the Δ_r values, while $\Delta(N_{eff}^2 - n_2^2)$ approaches $2\Delta_r$ values. The main implication is that carrier-induced index depressions will be most felt for DH structures of thin active layers (i.e., $d \leq 0.15 \mu\text{m}$). The expression for the threshold current density, J_{th} , has a term containing Γ ,^{11,22} which accounts for half of J_{th} at the thickness for minimum threshold,²² d_o , and dominates for $d < d_o$. That is, for an

InGaAsP/InP laser with $\Delta_r = -20\%$, the influence of carrier-induced depressions is to increase J_{th} by 10% for $d \cong 0.15 \mu\text{m}$ and by 20% for $d < 0.15 \mu\text{m}$. Manning et al³ have found Δ_r values as large as -30% for AlGaAs DH lasers. That, in turn, implies J_{th} increases by as much as 30% for $d < 700 \text{ \AA}$ in AlGaAs devices. These assumptions appear very reasonable considering that $|\Delta_r|$ increases with increasing carrier density at threshold,³ N_{th} . Also implied is that for single-quantum-well structures the effect of carrier-induced index depressions on Γ and J_{th} should be quite significant, especially for narrow wells ($L_z < 200 \text{ \AA}$), since the N_{th} values for quantum-well structures can be several times larger than the N_{th} values for DH structures.^{23,24}

The relative variations in the quantity $N_{eff}^2 - n_2^2$ with Δ_r have implications for lateral mode control. In buried heterostructures such as buried-mesa or buried-crescent devices, the waveguide width w_o for maintaining only the fundamental mode is inversely proportional¹⁸ to $\sqrt{N_{eff}^2 - n_2^2}$. That is, a relative dielectric-constant change Δ_r of -20% in a structure of thin active layer will increase w_o by 20%. That, however, is practically not very significant since the experimental w_o values are roughly twice the theoretical values.¹⁸ However, if the mesa in a BH device is of the LOC-type, the lateral mode control may be affected by the carrier-induced index depressions, since in LOC structures the effect of index depressions^{5,10} is much more dramatic than in standard DH structures. As for nonplanar DH structures, for which lateral mode control is obtained via active-layer thickness variations, the effect of index depressions on mode control appears negligible as illustrated in Fig. 2c by the slow variation of $\Delta(N_{eff}^2 - n_2^2)$ with D . It appears that carrier-induced index depressions can have a significant impact on lateral mode control only in gain-guided structures⁶ (i.e., lateral mode defined by the injected carrier profile) or in index-guided structures for which the transverse confinement factor Γ varies significantly across the optical mode.^{5,10}

Effect on Transverse Beamwidth and Asymmetric-Structure Wave Confinement

Another parameter that is affected by carrier-induced index depressions is θ_{\perp} , the beamwidth (full width at half maximum) in the plane perpendicular to the junction. We have previously published²⁵ an accurate approximation for θ_{\perp} :

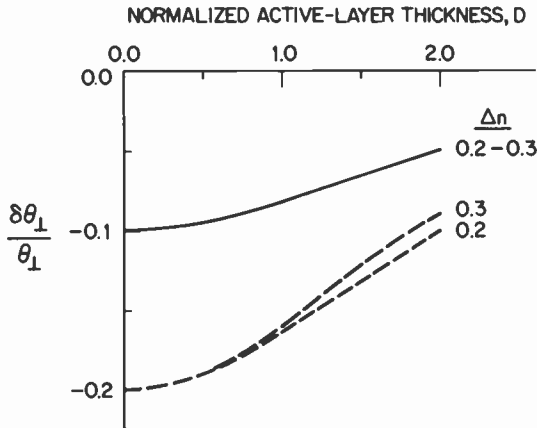


Fig. 3—The relative variations in the transverse beamwidth, θ_{\perp} , for two values of Δ_r (the relative change of the dielectric-constant step in DH structures): -10% (solid line) and -20% (dashed line). These variations are shown as a function of D , the normalized active-layer thickness (for InGaAsP/InP structure $D \cong 6.6 d$ for $1.2 \mu\text{m} < \lambda < 1.6 \mu\text{m}$). Δn is the refractive-index step (i.e., $\Delta n = n_1 - n_2$).

$$\theta_{\perp} \cong \frac{0.65 D \sqrt{n_1^2 - n_2^2}}{1 + 0.153 D^2 (1 + n_1 - n_2)}; \quad 0 < D < 2. \quad [11]$$

This expression is correct within 3% for D values up to 2, which cover the majority of practical cases (e.g., for InGaAsP/InP lasers, $D < 2$ corresponds to active-layer thicknesses less than $0.3 \mu\text{m}$). By differentiating Eq. [11], the relative variations in θ_{\perp} are found to be

$$\frac{\delta\theta_{\perp}}{\theta_{\perp}} \cong \frac{1 - 0.153 D^2 (n_1 - n_2)}{1 + 0.153 D^2 (1 + n_1 - n_2)} \Delta_r, \quad [12]$$

which is plotted in Fig. 3 for Δ_r values of -10% and -20% . Just as in the case of relative Γ variations (Eq. [4]), Eq. [12] is correct within 2% for Δ_r values as low as -30% . The trends in $\delta\theta_{\perp}/\theta_{\perp}$ with varying D , as displayed in Fig. 3, agree with the beamwidth data by Greene and Henshall²⁶ for which we have found²⁵ that calculated dielectric-constant steps ($\Delta\epsilon = n_1^2 - n_2^2$) corresponding to the measured beamwidths were significantly lower (-20 to -30%) for thin-active-layer ($d = 0.1\text{--}0.15 \mu\text{m}$) devices than for thick-active-layer ($d = 0.3\text{--}0.4 \mu\text{m}$) devices. That discrepancy can now be attributed to the effect of index depressions on θ_{\perp} . For thin active layers ($D < 1$) and a fixed Δ_r value of -20% , θ_{\perp} can decrease by as much as 20%; while for thicker active layers ($D \cong 2$), the θ_{\perp} decrease is only about

10%. Furthermore, for a given structure the value of $|\Delta_r|$ will increase with decreasing active-layer thickness, since Δ_r is roughly proportional³ to N_{th} , and N_{th} is well known to increase with decreasing active-layer thickness.^{11,22} For instance, it has been shown²⁵ that the volume current density J_{th}/d at the active-layer thickness for minimum threshold, d_o , is twice the value of J_{th}/d for large d 's ($d \geq 0.5 \mu\text{m}$). Since N_{th} is roughly proportional to J_{th}/d , it follows that it will behave similarly with varying d . Thus in an InGaAsP/InP laser of large active-layer thickness ($d > 0.3 \mu\text{m}$), θ_{\perp} will hardly be affected by index depressions; while for structures with $d \leq 0.15 \mu\text{m}$, θ_{\perp} will decrease by 20 to 30% from its values in a passive structure.

Another case of interest is asymmetric DH structures. Then an asymmetry factor η is defined:

$$\eta = \frac{n_1^2 - n_2^2}{n_1^2 - n_3^2} \quad [13]$$

with $n_1 > n_3 > n_2$. If a relative dielectric-constant variation Δ_r occurs (see Eq. [2b]), then the corresponding variation in asymmetry factor is

$$\frac{\Delta\eta}{\eta} = -\frac{\eta - 1}{1 + \eta\Delta_r} \Delta_r \quad [14]$$

For positive refractive-index increases, η decreases. In the case of index depressions, η increases and there is a lower limit on Δ_r :

$$\Delta_r > -\frac{1}{\eta}. \quad [15]$$

This limit appears since for $\Delta_r = -1/\eta$ the indices of the active layer and the high-index cladding layer are equal (i.e., $n_1 = n_3$) and thus optical confinement is lost. For example, if Δ_r can reach -20% values, the asymmetry factor η can have values only up to 5. The situation is quite similar to that in single heterostructure lasers for which optical confinement was lost at a certain injected-carrier concentration.¹¹ The field-intensity confinement factor is well approximated by¹⁴

$$\Gamma_a = \frac{\Gamma_a'}{1 + \Gamma_a'} \quad [16]$$

$$\Gamma_a' = \frac{2\sqrt{\eta}}{(1 + \sqrt{\eta})} \frac{D(D - \tan^{-1} \sqrt{\eta - 1})}{1 + \frac{(D - \tan^{-1} \sqrt{\eta - 1})}{\eta^2 \sqrt{(\eta - 1) + (D - \tan^{-1} \sqrt{\eta - 1})^2}}}$$

The equation is too complicated for obtaining a closed-form expression for the variation in Γ_a with Δ_r . One can compute relative Γ_a variations by using Eqs. [2b], [14], and [16]. We find that Γ_a is affected by index depressions very much the same as Γ in symmetric structures (Fig. 2a) except near the mode cutoff (i.e., close to the D value of $\tan^{-1} \sqrt{\eta - 1}$). For instance, in a structure with $n_1 = 3.60$, $n_2 = 3.30$, and $n_3 = 3.33$, a relative dielectric-constant change Δ_r of -20% will cause a Γ_a decrease of 42% at an active layer thickness of 500 \AA (passive mode cutoff thickness is 300 \AA). For $\delta\Gamma/\Gamma$ to be only -20% , as in symmetric DH structures, the active layer thickness has to increase to 700 \AA . The reason for these large variations is that Γ_a is not only affected by variations in D , but also by variations in η and in mode cutoff thickness, which increases with increasing index depressions. That spells caution for the growth of DH structures with very thin active layers ($d \leq 500 \text{ \AA}$), since it means that slight differences between the indices of the cladding layers will result in large increases in threshold current density. This fact has already been observed experimentally for thin-active-layer (TAL) OMVPE-grown DH structures.²⁷

Conclusion

In conclusion, we have derived simple and accurate closed-form analytical expressions for relative variations in Γ , b , N_{eff} , and θ_{\perp} as a function of Δ_r , the relative change in dielectric-constant step. It is found that the effects of Δ_r are strongest as the active-layer goes to zero. The results shed light on such experimental results as the threshold current density increasing faster than expected in structures with very thin active layers; a narrower transverse beam than expected for thin-active-layer structures; and slight asymmetries in DH structures causing serious threshold increases for thin-active-layer structures. The derived expressions should prove useful for laser-device design and understanding.

References:

- ¹ F. Stern, "Calculated Spectral Dependence of Gain in Excited GaAs," *J. Appl. Phys.*, **47**, p. 5382, Dec. 1976.
- ² C. H. Henry, R. A. Logan, and K. A. Bertness, "Spectral Dependence of the Change in Refractive Index Due to Carrier Injection in GaAs Lasers," *J. Appl. Phys.*, **52**, p. 4457, July 1981.
- ³ J. Manning, R. Olshansky, and C. B. Su, "The Carrier-Induced Index Change in AlGaAs and $1.3 \mu\text{m}$ InGaAsP Diode Lasers," *IEEE J. Quantum Electron.*, **QE-19**, p. 1525, Oct. 1983.
- ⁴ S. E. H. Turley, "Anomalous Effect of Carriers on Dielectric Constant of (In,Ga)(As,P) Lasers Operating at $1.3 \mu\text{m}$ Wavelength," *Electron. Lett.*, **18**, p. 590, 1983.

- ⁵ J. K. Butler and D. Botez, "Spatial Mode Discrimination and Control in High-Power Single-Mode Constricted Double-Heterojunction Large-Optical Cavity Diode Lasers," *Appl. Phys. Lett.*, **40**, p. 1118, 15 Dec. 1982.
- ⁶ J. C. Bouley, J. Charil, Y. Sorel, and G. Chaminant, "Injected Carrier Effects on Modal Properties of 1.55 μm GaInAsP Lasers," *IEEE J. Quantum Electron.*, **QE-19**, p. 969, June 1983.
- ⁷ S. Turley, "Optical Waveguiding in (In,Ga)(As,P) Inverted Rib Waveguide Lasers at 1.3 μm Wavelength," *IEEE J. Quantum Electron.*, **QE-19**, p. 1186, July 1983.
- ⁸ H. Kressel, H. F. Lockwood, and J. K. Butler, "Measurements of Refractive Index Step and of Carrier Confinement at (AlGa)As-GaAs Heterojunctions," *J. Appl. Phys.*, **44**, p. 4095, Sept. 1973.
- ⁹ H. C. Casey, Jr., D. D. Sell, and M. B. Panish, "Refractive Index of $\text{Al}_x\text{Ga}_{1-x}\text{As}$ between 1.2 and 1.8 eV," *Appl. Phys. Lett.*, **24**, p. 63, 15 Jan. 1974.
- ¹⁰ J. K. Butler and D. Botez, "Lateral Mode Discrimination and Control in High-Power Single-Mode Diode Lasers of the Large-Optical-Cavity (LOC) Type," submitted for publication to *IEEE J. Quantum Electron.*
- ¹¹ H. Kressel and J. K. Butler, *Semiconductor Lasers and Heterojunction LED's*, New York: Academic Press, 1977.
- ¹² J. Buus, "Detailed Field Model for DH Stripe Lasers," *Opt. Quantum Electron.*, **10**, p. 459, 1978.
- ¹³ J. K. Butler and D. Botez, "Mode Characteristics of Nonplanar Double-Heterojunction and Large-Optical-Cavity Laser Structures," *IEEE J. Quantum Electron.*, **QE-18**, **6**, p. 952, June 1982.
- ¹⁴ D. Botez, "Near and Far-Field Analytical Approximations for the Fundamental Mode in Symmetric Waveguide DH Lasers," *RCA Review*, **39**, p. 577, Dec. 1978.
- ¹⁵ D. Botez, "Analytical Approximation of the Radiation Confinement Factor for the TE_0 Mode of a Double Heterojunction Laser," *IEEE J. Quantum Electron.*, **QE-14**, p. 230, April 1978.
- ¹⁶ D. Botez, unpublished work.
- ¹⁷ W. Streifer and E. Kapon, "Application of the Equivalent-Index Method to DH Diode Lasers," *Appl. Opt.*, **18**, p. 3724, Nov. 15, 1979.
- ¹⁸ D. Botez, "Effective Refractive Index and First Order Mode Cut-off Condition in InGaAsP/InP DH Laser Structures ($\lambda = 1.2-1.6 \mu\text{m}$)," *IEEE J. Quantum Electron.*, **QE-18**, p. 865, May 1982.
- ¹⁹ K.-L. Chen and S. Wang, "An Approximate Expression for the Effective Refractive Index in Symmetric DH Lasers," *IEEE J. Quantum Electron.*, **QE-19**, p. 1354, Sept. 1983.
- ²⁰ T. L. Paoli, "Waveguiding in a Stripe-Geometry Junction Laser," *IEEE J. Quantum Electron.*, **QE-18**, p. 662, 1977.
- ²¹ J. Buus, "The Effective Index Method and its Application to Semiconductor Lasers," *IEEE J. Quantum Electron.*, **QE-18**, p. 1083, 1982.
- ²² D. Botez, "Optimal Cavity Design for Low-Threshold-Current Density Operation of Double-Heterojunction Diode Lasers," *Appl. Phys. Lett.*, **35**, p. 57, July 1, 1979.
- ²³ H. K. Dutta, "Calculated Threshold Currents of GaAs Quantum-Well Lasers," *J. Appl. Phys.*, **53**, p. 7211, Nov. 1982.
- ²⁴ A. Sugimura, "Threshold Currents for AlGaAs Quantum Well Lasers," to be published in *IEEE J. Quantum Electron.*
- ²⁵ D. Botez, "InGaAsP/InP Double-Heterojunction Lasers: Simple Expressions for Wave Confinement, Beamwidth and Threshold Current over Wide Ranges in Wavelength (1.1-1.65 μm)," *IEEE J. Quantum Electron.*, **QE-17**, p. 178, Feb. 1981.
- ²⁶ P. D. Greene and G. D. Henshall, "Growth and Characteristics of (Ga,In)(As,P)/InP Double Heterostructure Lasers," *IEE Solid-State and Electron Devices*, **3**, p. 174, Nov. 1979.
- ²⁷ D. E. Ackley, private communication.

Low Expansion Porcelain-Coated Copper-Clad Invar Substrates

K. W. Hang, A. N. Prabhu, J. Andrus, S. M. Boardman, and
L. S. Onyshkevych

RCA Laboratories, Princeton, N.J. 08540

Abstract—The development of a high temperature porcelain coated copper-clad invar substrate for use in applications involving large area, leadless ceramic chip carriers (LCCC) is described. A liquid-to-liquid thermal cycling study of the soldered LCCC assemblies on porcelain-coated steel substrates has shown fatigue cracking of solder joints and thick-film conductor delamination under the solder joints after a relatively small number of cycles. This is because of a large difference between thermal coefficients of expansion (TCE) of the substrate and the ceramic devices. To eliminate this TCE mismatch problem, a low expansion devitrifying glass composition has been formulated. This glass, when electrophoretically deposited on a Cu/Invar/Cu (16/68/16) metal core and fired, produces a composite having a refire capability of 850°C. An analysis of the thermal expansion characteristics of the metal core, glass, and composite has shown that the substrate TCE is similar to that of LCCC between typical operating temperatures. Firing of the thick films at a peak temperature of 850°C leads to well developed microstructures, thus making them suitable for high reliability applications. Variables affecting the substrate quality that have been investigated include physical properties of the glass powder, prepared metal surface characteristics, and deposition and firing parameters. A reduction in the incidence of voids at the metal core-porcelain interfaces is required for the substrates to be utilized in high voltage applications. The soldered LCCC assemblies on these low-expansion substrates have shown less susceptibility for solder fatigue damage during thermal cycling.

Introduction

The advantages of porcelain-coated metal as PC board substrates have long been recognized.¹ The conventional, commercially-available, glassy-type porcelain-enamels, however, exhibit re-fire temperatures that are too low for most thick-film inks. A devitrified high-temperature enamel coating was therefore developed at RCA Laboratories for low-carbon steel cores.² This material was shown to exhibit excellent properties³: re-fire temperatures to 950°C, very low defect counts, excellent porcelain/metal adhesion, outstanding edge and hole coverage, very low level of Na or K contamination, resistivities in excess of 10^{14} Ω -cm, as well as very high reliability and manufacturability. A full range of compatible base-metal and noble-metal thick-film inks complements the system and makes it useful for numerous electronic applications.

For a small number of special electronic applications, however, the steel-cored enamelled substrates are unusable, because of a mismatch in expansion coefficients with some IC packages, particularly with the leadless ceramic chip carriers (LCCC), which are fabricated using 94% Al_2O_3 substrates. This paper describes our initial effort to develop high temperature (devitrified) porcelain/metal substrates for electronics circuits containing LCCC's and similar devices.

Leadless Ceramic Chip Carriers on Porcelain/ Metal Substrates

The utilization of LCCC's is becoming increasingly important, as more and more integrated circuits are becoming available in such packages. The LCCC's are well matched to the Al_2O_3 substrates, which are widely utilized in hybrid circuits. The alumina substrates, however, are limited in size and usually too expensive for consumer-type (low cost) applications. It would be desirable to use the LCCCs on PC boards, or porcelain/metal substrates, which have no such limitations. These substrates, however, have the disadvantage of having a significantly larger thermal coefficients of expansion (TCE) in the X-Y directions than the ceramic chip carriers, as indicated in Table 1.⁵⁻⁸ When the LCCC's are soldered directly to the board, the soldered connections are forced to absorb the strain caused by the thermal-expansion-rate difference between the LCCC and the substrate. The strains developed, either during power cycling or environmental temperature cycling, are a reliability concern, since the cumulative fatigue damage can lead to solder joint failures.⁹⁻¹⁴

Table 1—Thermal Expansion Coefficients (TCE)

Material	TCE (RT-150°C) (ppm/°C)
94% Alumina	6
FR-2	15-20 (X-Y)
CEM-3	12-20 (X-Y)
FR-4	12-16 (X-Y)
Polyimide-Glass	11-14 (X-Y)
Copper	15-20
Alloy 42 (Fe-Ni, 42)	5
Cu/Invar/Cu (16/68/16)	6
Kevlar Fiber	-2
Quartz Fiber	0.5-0.6
Glass Fiber	4-5
Polyimide-Kevlar	6-7 (X-Y)
Epoxy-Kevlar	6-7 (X-Y)
Polyimide-Quartz	6-7 (X-Y)
Porcelain Coated Steel	10-12 (X-Y)
Porcelain Coated Cu/Invar/Cu	6 (X-Y)

The approaches being considered to overcome the TCE mismatch problem between the chip carrier and a substrate are indicated in Table 2.⁵ The two technologies listed in the Table are multilayer laminates (with etched/plated copper conductors) and porcelain coated Cu/Invar/Cu substrates, where thick film technology is utilized for forming conductor and dielectric layers. In the case of modified multilayer laminates, the TCE mismatch problem can be minimized by restraining the substrate from its normal expansion by bonding it to a low expansion core, by controlling the TCE of the substrate by integrating a low expansion material (such as Kevlar or quartz), or by making the substrate more compliant. In the case

Table 2—Approaches Used to Overcome TCE Mismatch Between Chip Carrier and Substrate

Method	Examples	Metallization
Restrain the Substrate— Bond to a Low-Expansion Core	Alloy 42	Etched/Plated Cu
	Cu/Mo/Cu	Etched/Plated Cu
	Cu/Invar/Cu	Etched/Plated Cu
	Epoxy/Carbon Fiber	Etched/Plated Cu
Inherent TCE Control	Kevlar-Epoxy	Etched/Plated Cu
	Kevlar-Polyimide	Etched/Plated Cu
	Quartz-Polyimide	Etched/Plated Cu
	Porcelain Coated Cu/Invar/Cu	Thick Film Cu, Au-Pt, Ag-Pd
Compliant Films on Laminates	Elastomer Coated FR-4	Etched/Plated Cu

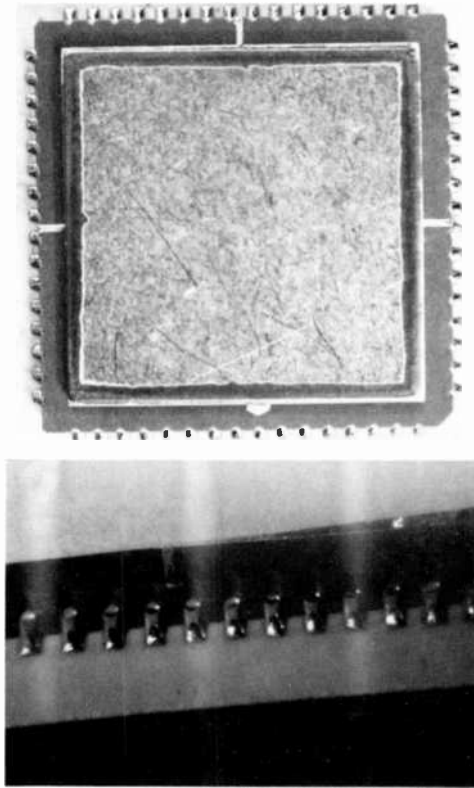
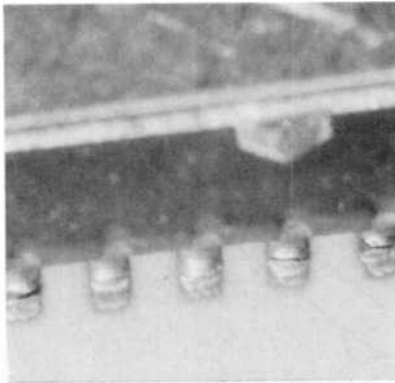


Fig. 1—LCCC assembly on porcelain-coated steel.

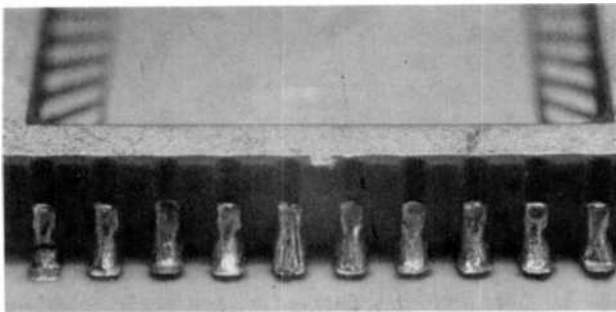
of the porcelain coated Cu/Invar/Cu substrates, TCE matching with the LCCC is achieved through the inherent low expansion of the composite in the X-Y direction.

Thus, the porcelain-metal substrates, with a low-expansion metal core (such as Cu/Invar/Cu) are very promising for circuits with LCCCs.⁷ The one factor that has so far held back the widespread use of these substrates has been the nonavailability of high-reheat-temperature materials for Cu/Invar/Cu cores. The commercially available porcelains on Cu/Invar/Cu have re-fire temperatures generally below 700°C. When fired at such low temperatures, the microstructures of conductor and multilayer dielectric films are not fully developed. Therefore thick-film-related failures have been observed during thermal cycling of leadless ceramic chip carrier assemblies on such substrates.

The objective of our efforts was to develop high-temperature porcelain-coated Cu/Invar/Cu substrates for high reliability ceramic



(a)



(b)

Fig. 2—Thermal cycled LCCC solder joints on porcelain-coated steel: (a) solder cracks and (b) thick-film delamination.

chip carrier applications. This meant developing a substrate that could be re-fired at temperatures greater than 800°C. The program involved (1) a study of LCCC solder reliability on RCA porcelain coated *steel* substrates¹⁵; (2) formulation of a lower expansion, devitrifying, porcelain composition with a high temperature reheat capability and establishing electrophoretic deposition parameters and metal preparation techniques for it; and, (3) surface-mounting leadless ceramic chip carriers on these substrates and performing the necessary temperature cycling of such units. The preliminary results of this study are reported here.

LCCC Solder Joint Reliability on Porcelain Coated Steel Substrates

The substrates used were fabricated by electrophoretically depositing a devitrifying frit composition on a low-carbon steel core and

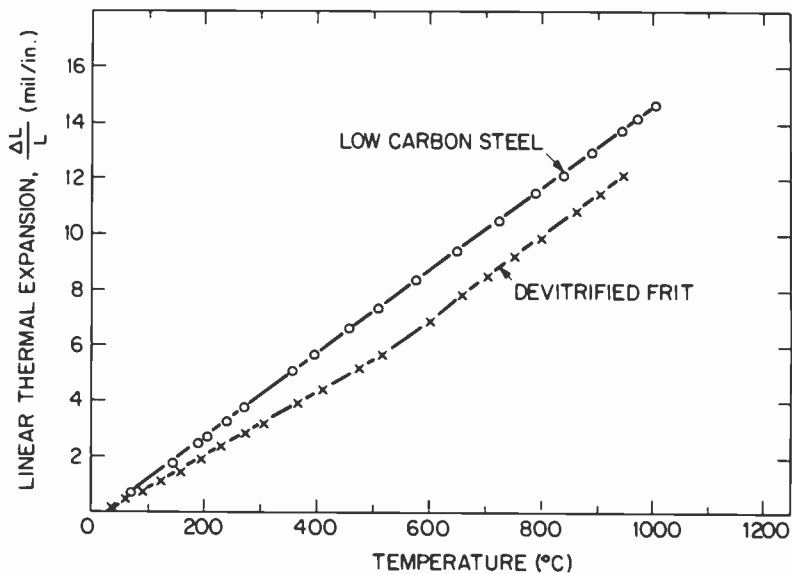


Fig. 3—Thermal expansion of low carbon steel and devitrified frit.

firing at a peak temperature of 900°C.¹⁵ Thick film copper conductor footprints were utilized for chip carrier attachment. A compatible copper conductor ink² was screen printed using a stainless steel screen and fired in nitrogen in a conveyORIZED furnace at a peak temperature of 900°C. Leadless ceramic chip carriers, with 64 pins, on 1-mm spacing, were used for the initial study. A 60/40, Sn/Pb solder paste was deposited on the conductor footprints, the chip carriers were placed, the assemblies were dried in air, and then reflow-soldered. One such assembly is shown in Fig. 1.

Studies of the initial joints (Fig. 1) do not indicate any solder cracks in the samples after assembly. However, solder joint cracking can be clearly seen (Fig. 2) in parts which underwent thermal cycling. These assemblies were subjected to liquid-to-liquid thermal cycling, which consisted of holding at -55°C for 2 minutes in a cold bath of dry ice and acetone, followed by transferring in less than 8 seconds to a hot bath of fluorinert and holding at 125°C for 2 minutes. The parts were then examined for failures due to cracking of solder joints and for thick-film delamination. After ~100 thermal cycles, a large number of solder joints cracked. A similar study, which used 40-pin chip-carriers, indicated solder cracking after ~150 thermal cycles and thick-film delamination under the solder joints after ~200 thermal cycles.

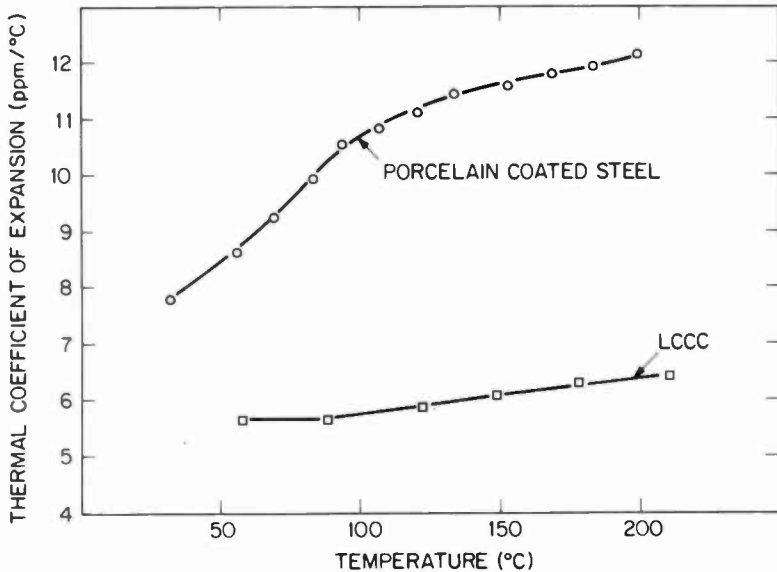


Fig. 4—TCE of porcelain-coated steel and LCCC.

The high TCE of the porcelain-steel composite is primarily due to the high TCE of the low-carbon steel, as shown in Fig. 3, where expansion data (measured by a dilatometer) are plotted as a function of temperature for the steel and the coating. The porcelain expansion rate is lower than that of the steel, so that the devitrified material can be under compression. In Fig. 4, the thermal coefficient of expansion of the composite substrate is compared to that of the 94% alumina used in the LCCC's. Between room temperature and 200°C, the difference in expansion rates of the porcelain-coated steel and the 94% alumina increases as temperature increases. As expected, this expansion rate difference leads to fatigue damage.

Fabrication of Porcelain-Coated Cu/Invar/Cu Substrates

In addition to providing a better TCE match with LCCC's, coated copper-clad Invar substrates also give increased thermal and electrical conductivity and eliminate the ferromagnetic effects of the steel. Invar is a low-expansion alloy; if clad with copper on both sides, it can be designed to match the desired thermal expansion curves of the LCCC's over the operating temperature range; the Cu/Invar/Cu laminates are commercially obtainable from the Texas Instruments Corporation.¹⁴ The best match to the 94% Al_2O_3 is accomplished by selecting a 16% Cu/68% Invar/16% Cu ratio.

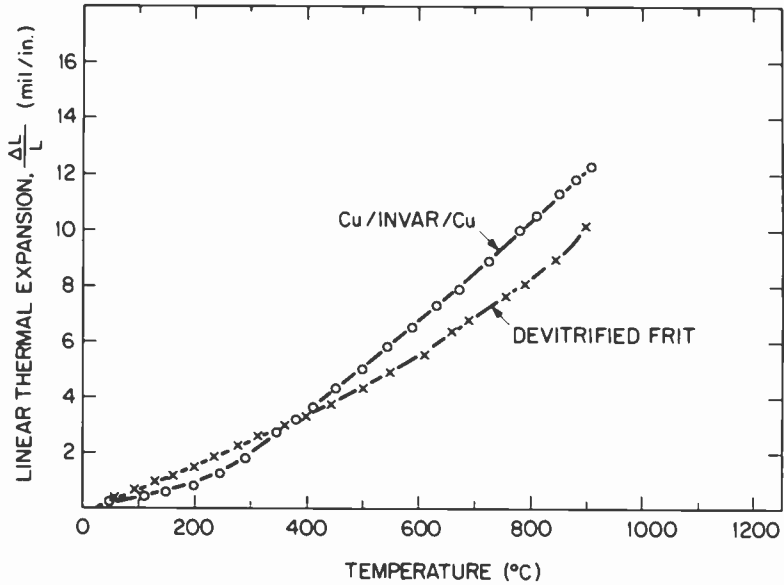


Fig. 5—Thermal expansion of Cu/Invar/Cu (16/68/16) and low-expansion devitrified frit.

The linear thermal expansion of this composite is shown in Fig. 5. Notice, that the expansion is not linear (as is that of steel, shown in Fig. 3), but fairly low from room temperature (RT) to ~200°C,

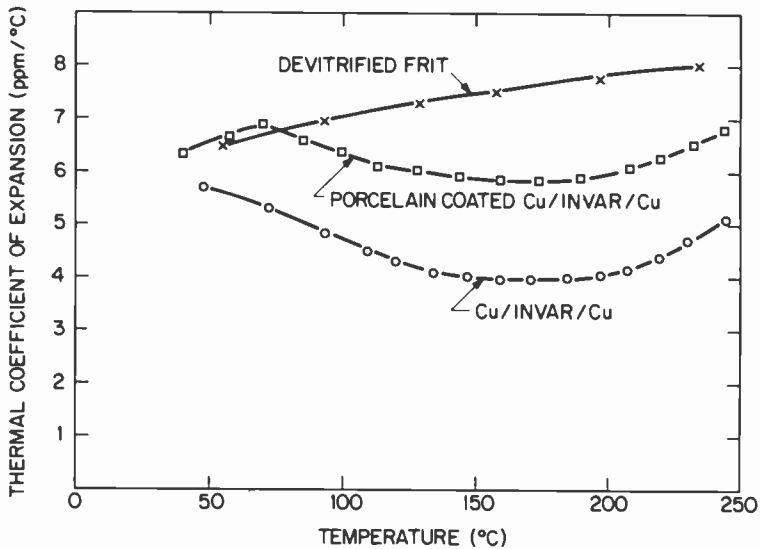


Fig. 6—TCE of porcelain-coated Cu/Invar/Cu, devitrified frit, and Cu/Invar/Cu.

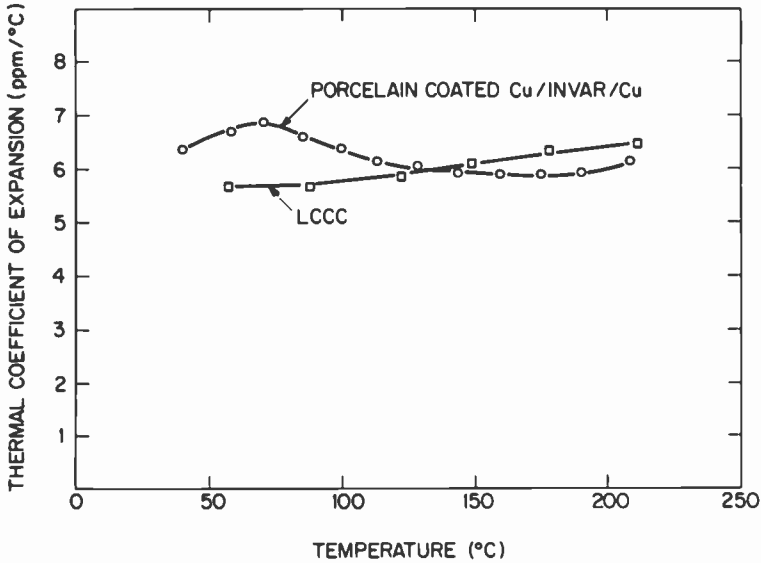


Fig. 7—TCE of porcelain-coated Cu/Invar/Cu and LCCC.

while raising rapidly above 200°C, and reaching values similar to that for steel at about 800°C. Because of this nonlinear behavior, designing a porcelain coating for the Cu/Invar/Cu core is rather difficult. If one chooses a composition with an expansion rate lower than that of Cu/Invar/Cu below 200°C, then the composite will have an expansion rate much lower than that of alumina. To have a composite with a TCE similar to Cu/Invar/Cu between RT and 200°C, the porcelain expansion rate has to be greater than that of Cu/Invar/Cu. However, at the sealing temperature, such a composition should have a TCE lower than that of Cu/Invar/Cu, so that the coating is under compression. The thermal expansion characteristics of the porcelain composition designed to meet these requirements are shown in Fig. 5. As can be seen, between RT and 200°C the expansion rate is greater than that of Cu/Invar/Cu. The composition of this material is a modification of the devitrifying frit used for coating low carbon steels.¹⁵ A compromise has been made in the composition, so that it exhibits a low TCE, while maintaining its devitrification characteristics to produce a smooth and inert coating.

The TCE of the composite is compared to the TCE's of the core metal and porcelain in Fig. 6. In the temperature range indicated, the TCE of Cu/Invar/Cu varies from 3.9 to 5.7 ppm/°C and the TCE of the porcelain varies from 6.4 to 8.0 ppm/°C. The composite TCE

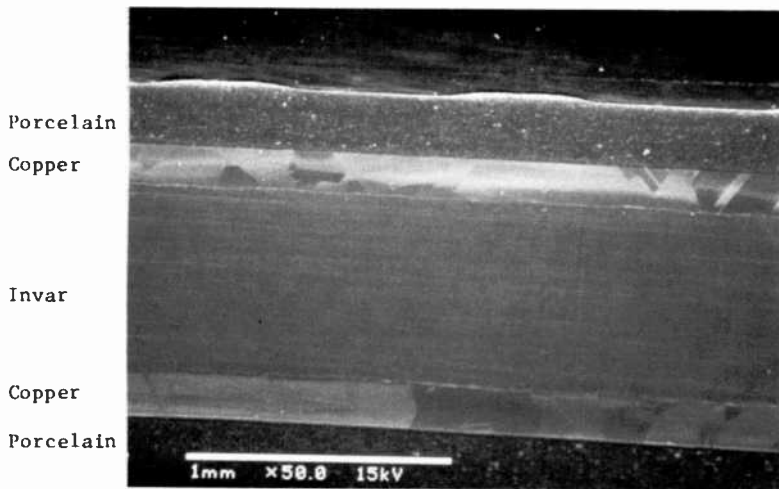


Fig. 8—Cross sectional micrograph of porcelain-coated Cu/Invar/Cu.

ranges from 5.8 to 6.8 ppm/°C. As expected, the expansion rate of the composite generally follows that of the core. The TCE of the composite is compared to that of an LCCC in Fig. 7. The expansion rates of the LCCC and those of the coated Cu/Invar/Cu composite are quite comparable and hence the fatigue damage of the solder joints during thermal cycling of chip carrier assemblies on these substrates should be much lower than that observed for porcelain-coated steel substrates.

The fabrication steps for the porcelain-coated Cu/Invar/Cu substrates are, in general, similar to those for steel-cored boards,² with some notable exceptions. Thus, a new (proprietary) metal preparation process had to be developed, to assure good adhesion between the porcelain and the Cu surface. The frit is prepared in a process very similar to that used for the steel-compatible porcelains,¹⁵ involving melting of raw materials, quenching, and dry and wet milling. The coating powder is deposited upon the Cu/Invar/Cu core by electrophoretic methods. The resulting dense powder compact is dried and then rapidly fired at ~850°C, to obtain a finished porcelain coating.

Physical Properties of the Porcelain-Coated Cu/Invar/Cu Substrates

The adhesion of the porcelain to the copper surface is quite good. The substrates can be subjected to multiple firings at 850°C without

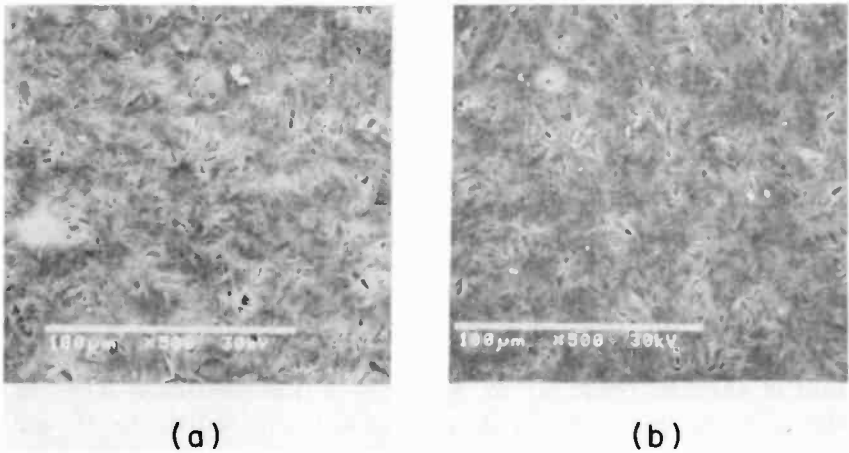


Fig. 9—SEMs of porcelain surface (a) after one and (b) after ten firings at 850°C.

incurring any delamination at the copper-porcelain interface. However, the porcelain does not adhere well to the edges where Invar metal is exposed. If the edges are masked off during glass deposition, the exposed edges can be used for electrical grounding. Fig. 8 shows a cross-section of a porcelain-Cu-Invar substrate. A fairly sharp interface between the porcelain and copper is visible. How-

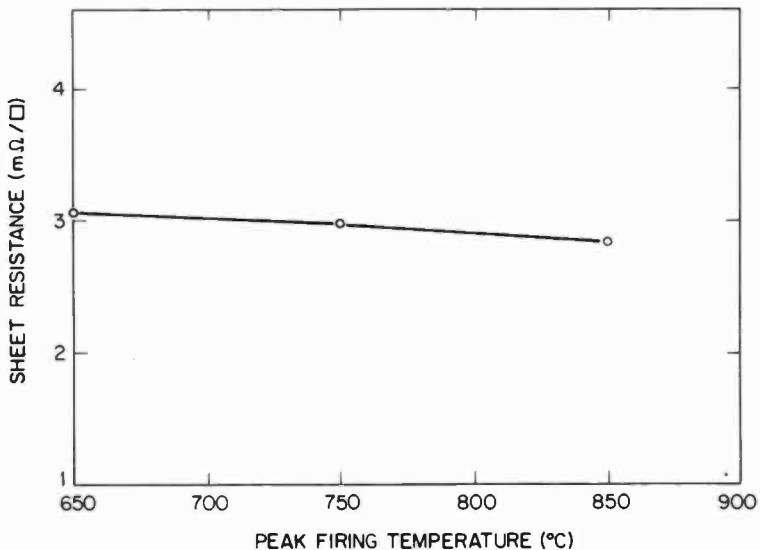


Fig. 10—Effect of peak firing temperature on thick-film copper sheet resistance.

ever, we have seen some incidences of interfacial voids between copper and porcelain. Such defects are substantially reduced when the core material is changed to oxygen free high conductivity (OFHC) copper, suggesting that some degassing occurs from the laminated metal structure.

Fig. 9 shows scanning electron micrographs of the porcelain surface after 1 and 10 refirings at 850°C. With the initial samples, it was observed that the first refiring at 850°C produced some surface-topography changes (recrystallization), but subsequent refirings produced no further changes. Thus, the initial firing of the substrate has to be lengthened to assure fully stabilized surfaces.

Since the expansion coefficients of the new porcelain are close to that of alumina (from RT to 200°C), it is possible to use many of the thick films developed for alumina on this substrate. In our thermal cycling experiments, the DuPont 9923 ink was utilized for forming conductor patterns. The sheet resistances of the copper films, fired at peak temperatures ranging from 650° to 850°C in nitrogen, are indicated in Fig. 10. Even when fired at 650°C, the sheet resistance is quite low, about 3.05 mΩ/□. Upon firing at 750°C and 850°C, there is a decrease in the sheet resistivity. This decrease, however, is quite small, the sheet resistance of the copper film fired at 850°C being 2.8 mΩ/□.

The sheet resistance alone cannot be used as a measure of microstructural development in the conductor films. Even though the sheet resistance differences are small between the films fired at 650° and 850°C, the low-temperature-fired films are inferior in terms of film density, and therefore adhesion, bondability, and environmental stability. This becomes evident from scanning electron micrographs of the copper films fired at 650°, 750°, and 850°C (Fig. 11). In the case of films fired at 650°C, very little sintering of the copper particles has taken place, and, as a result, the films have very high surface porosity. When fired at 750°C, particle sintering has progressed to some extent, but there still is considerable porosity. However, when fired at 850°C, a well-developed microstructure is obtained. Firing at 850°C leads not only to well sintered contacts, but also results in considerable growth of particles, thus giving a dense film with little porosity. Firing ten times at 850°C leads to some further growth of the larger particles at the expense of the smaller ones. However, these changes are not that significant, suggesting that most of the required sintering of copper particles takes place during the first firing at 850°C.

A scanning electron micrograph of a cross-section of the conductor and porcelain is shown in Fig. 12. The copper film is quite dense

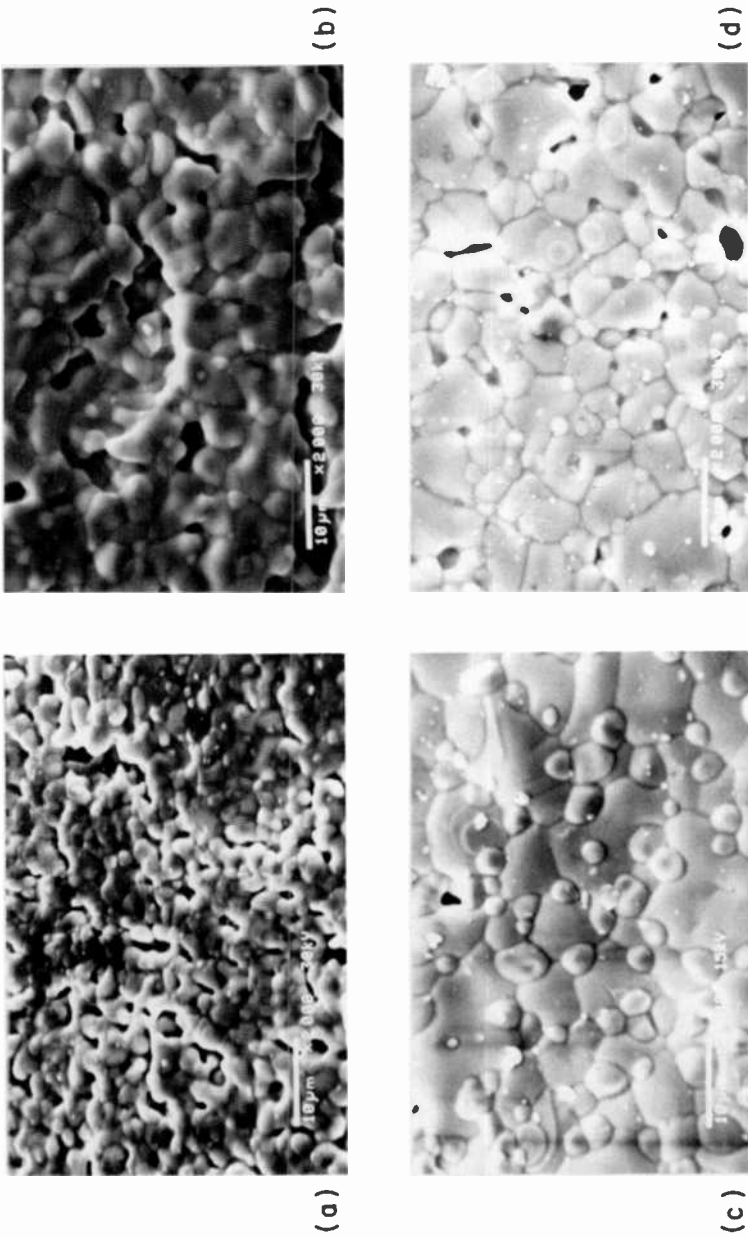


Fig. 11—SEMs of surfaces of copper thick films fired at (a) 650°C, (b) 750°C, (c) 850°C, and (d) 10 times at 850°C.

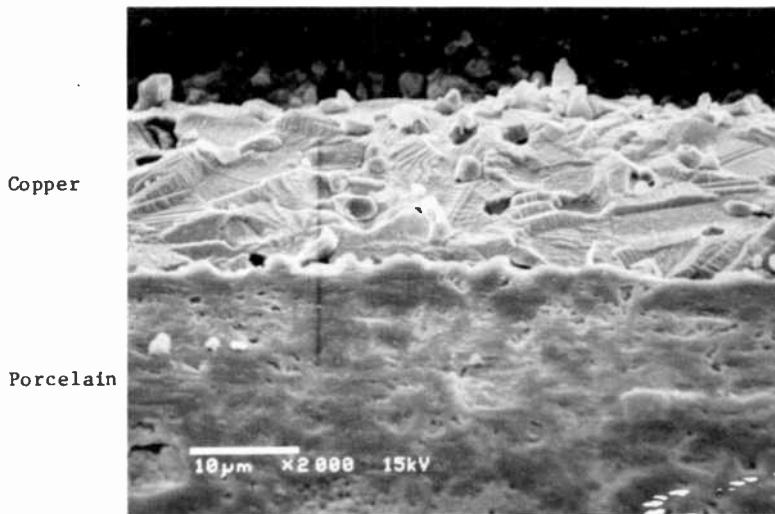


Fig. 12—SEM showing cross section of thick-film copper and porcelain.

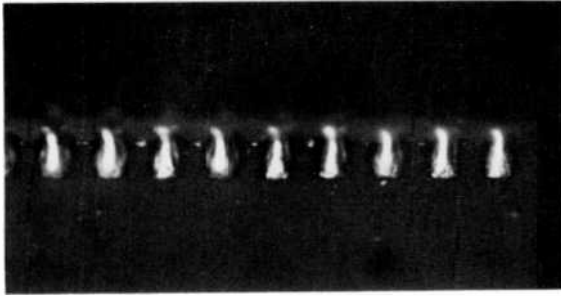
and the interface between copper and porcelain is quite sharp. Since the porcelain is quite inert, very little copper diffuses into the porcelain body during thick film firing. This is desirable, as the diffusion of various thick-film materials into the porcelain could lead to a degradation of its electrical properties.

Thermal Cycling of Porcelain-Coated Cu/Invar/Cu Substrate—LCCC Solder Assemblies

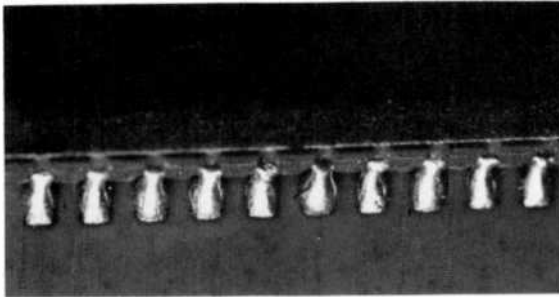
The procedure used for attaching ceramic chip carriers (40-pin, 1mm spacing) to the porcelain coated copper-clad Invar substrates was similar to the procedure described earlier for the porcelain/steel substrates. The conductor footprints were formed by firing the copper ink at 850°C. Fig. 13 shows the solder joint integrity of the as-soldered parts and the same parts after 200 and 600 thermal cycles. There are no visible cracks in the solder joints even after the 600 cycles. There is also no thick film delamination from the substrate.

Conclusions

The results presented in this paper confirm the previous findings that, in order to decrease solder cracking problems during thermal cycling, the TCE of the substrate has to be similar to the ceramic chip carrier. Therefore, for applications involving surface mounted, large area, leadless packages, it is possible to use porcelain-coated



(a)



(b)

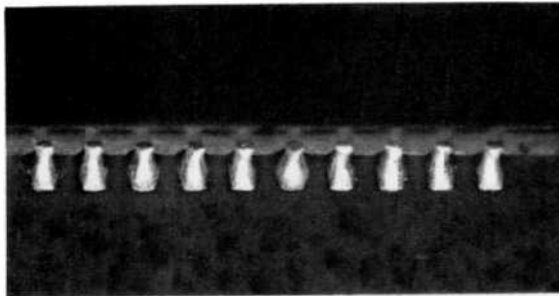


Fig. 13—LCCC solder joints on porcelain coated Cu/Invar/Cu: (a) as-soldered, (b) after 200 thermal cycles, and (c) after 600 thermal cycles.

copper-clad Invar substrates and expect the soldered assemblies to survive a large number of thermal cycles, without significant deterioration in the solder joints. Secondly, by having a high temperature reflow capability (above 800°C) the thick film properties can be adequately developed, thus minimizing thick-film-related failures.

The high temperature, low expansion, porcelain-coated Cu/Invar/Cu substrates described in this paper combine the high temperature reheat stability and the thermal expansion characteristics of alu-

mina with the advantages of the porcelain-coated substrates, such as low cost and superior mechanical and thermal properties. Therefore they can be utilized in applications involving leadless ceramic chip carrier assemblies on large area substrates. However, further work is necessary to reduce the incidence of interfacial voids between the core and the porcelain, so that these substrates can be utilized for high voltage applications. Additional work is anticipated in the areas of environmental stability and long-term electrical properties.

Acknowledgments

The authors wish to thank W. Anderson for preparing the glass and R. Schelhorn for helpful discussions and for supplying some of the materials used in this study.

References:

- ¹ L. Onyshkevych, "Developments with Porcelain Enamel Steel Substrates for Electronic Applications," *Proc. Porcelain Enamel Institute*, Vol. 42, 1980, pp. 166-177.
- ² *RCA Review*, Vol. 42, No. 2., June 1981 (This entire issue is devoted to the RCA developed porcelain-steel substrate technology).
- ³ A. N. Prabhu, K. W. Hang, and L. S. Onyshkevych, "Porcelain Coated Steel Substrate with Compatible Base Metal Thick Film System," *Proc. 1982 International Microelectronics Conf.*, May 1982, Tokyo, pp. 226-233.
- ⁴ J. A. Bauer and R. F. Kolc, "Growth in Applications of Chip Carriers," Chip Carrier Interconnection Technology Workshop, IEPS, New York, June 1981.
- ⁵ H. W. Markstein, "Surface-Mount Substrates: The Key in Going Leadless," *Electronic Packaging and Production*, June 1983.
- ⁶ W. G. Riemann and L. C. Gates, "Polyimide-Quartz Fabric Printed Circuit Boards for Mounting Leadless Chip Carriers," *IPC Technical Review*, March 1983.
- ⁷ R. Schelhorn, "New Metal Core Materials for Porcelainized Substrate Applications," *ISHM Proceedings*, Oct. 1981.
- ⁸ R. F. Kolc, "Applications of Porcelain Metal Core Substrates," *IEPS Proceedings*, Nov. 1981.
- ⁹ R. W. Korb and D. A. Ross, "Direct Attachment of Leadless Chip Carriers to Organic Matrix Printed Wiring Boards," *IEEE-CHMT Transactions*, Sept. 1983.
- ¹⁰ J. R. Taylor and D. J. Pedder, "Joint Strength and Thermal Fatigue in Chip Carrier Assembly," *ISHM Proceedings*, Nov. 1982.
- ¹¹ D. E. Riemer and J. D. Russell, "The Optimized Solder Bond for Ceramic Chip Carriers on Ceramic Boards," *ISHM Proceedings*, Oct. 1983.
- ¹² C. A. Harper and W. W. Staley, "Some Critical Materials Factors in the Application of Leadless Chip Carrier Packages," *Electronic Packaging and Production*, Aug. 1981.
- ¹³ R. L. Schelhorn, "Thick Film Multilayer Chip Carriers Circuit Fabrication on Porcelainized Metal Core Substrates," *NEPCON West Proceedings*, 1982.
- ¹⁴ F. J. Dance, "Copper-Clad Invar for Reliable Packaging and Interconnection of Leadless Ceramic Chip Carriers," *IEPS Proceedings*, Oct. 1983.
- ¹⁵ K. W. Hang, J. Andrus and W. M. Anderson, "High-Temperature Porcelain-Coated-Steel Electronic Substrates—Composition and Properties," *RCA Review*, 42, p. 159, June 1981.

A Novel Memory Device for VLSI E²PROM

S. T. Hsu

RCA Laboratories, Princeton, NJ 08540

Abstract—The structure and the characteristics of an offset floating gate electrically alterable nonvolatile memory MOSFET are presented. This device exhibits excellent asymmetrical write/erase properties, very long memory retention time, and good endurance. The offset floating gate memory MOSFET's can be arranged in an X-Y matrix to provide an E²PROM array having a common diffusion line for adjacent columns of devices. Therefore, the cell size of the E²PROM array can be very small.

1. Introduction

An electrically alterable read only memory (E²PROM) can dramatically increase the flexibility and applicability of an electronic system. The data stored in and the memory program for an E²PROM in an electronic system can be very easily updated. They can even be altered by a remote control device.

The memory cell of an E²PROM can be either an MNOS or a floating-gate MOS transistor. Since the procedure for fabricating MNOS devices is not compatible to that of MOS or bipolar integrated circuits, integration of the NMOS memory device as part of the VLSI circuit is not very attractive. There are many types of floating gate E²PROM cell structures¹⁻⁵. Since each memory cell may consist of one or more than one device, the memory cell size can be relatively large. The E²PROM cell presented in this paper is a simple offset floating-gate nonvolatile memory transistor that exhibits excellent asymmetrical write/erase characteristics. Therefore, when this device is used as the memory cell in an E²PROM array, a common diffusion line can be used as the drain or the source of the two adjacent columns of memory cells. As a result, the area occupied by one memory cell of this device can be less than half the area of a single transistor E²PROM memory cell. This device is, therefore, very useful for VLSI E²PROM circuits.

2. Device Structure

The device is a floating-gate nonvolatile memory transistor. The floating gate is offset to cover part of either the n^+ diffusion source or drain regions. For the sake of simplicity we shall refer to the n^+ diffusion layer overlapped by the floating gate as the drain. In reality either n^+ diffusion region can be the source or drain of the transistor. A cross section of the device is shown in Fig. 1. Fig. 1(A) shows a silicon-on-insulator structure, such as SOS; Fig. 1(B) shows the cross section of a bulk silicon offset floating-gate memory transistor. The two n^+ diffusion regions are source and drain regions. Approximately half the channel region is covered by the floating gate. The surface potential of the portion of the channel region labeled l_1 is controlled by the control gate. The surface potential of region l_2 is controlled by both control gate and the charges at the

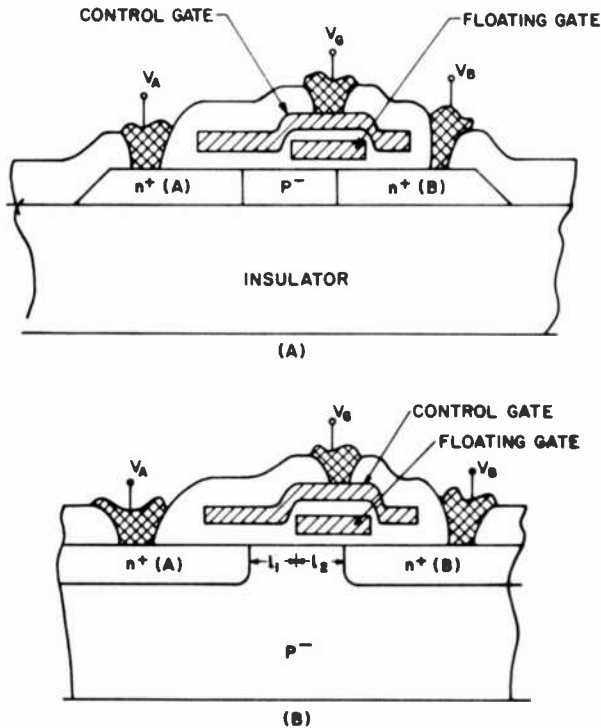


Fig. 1—Cross sections of floating-gate nonvolatile memory transistors: (A) silicon-on-insulator structure and (B) bulk silicon structure.

floating gate. This device can be operated in gate injection (GIMOS) mode⁴⁻⁶ or substrate injection mode^{1-3,7} depending on the thickness and the interface properties of insulators on and under the floating gate. For the gate injection mode, current flowing through the oxide on the floating gate is larger than that which flows through the oxide under the floating gate. If the current that flows through the oxide on the floating gate is smaller than that flowing through the oxide under the floating gate, the device is operated in the substrate injection mode. Since the distance between the floating gate and the source, A, is very large, no electron or hole can flow between these two electrodes under normal write/erase conditions.

When voltages V_G , V_A , and V_B are applied to the gate and A and B $n +$ diffusion layers, respectively, the voltage at the floating gate, V_F , is given by

$$V_F = \frac{Q_F + C_G V_G + C_A V_A + C_B V_B}{C_G + C_A + C_B + C_S}, \quad [1]$$

where C_G , C_A , C_B , and C_S are the capacitances between the floating gate and the control gate, source A, drain B, and substrate, respectively. Q_F is the charge stored at the floating gate. We assume that there is no voltage drop within the floating gate and that the substrate is grounded. The work function difference and the interface state charges are also neglected.

The voltage differences from the floating gate to the control gate, V_{FG} , to the source, V_{FA} , and to the drain, V_{FB} , are given by

$$V_{FG} = V_F - V_G = \frac{Q_F + C_A V_A + C_B V_B - (C_A + C_B + C_S) V_G}{C_G + C_A + C_B + C_S}, \quad [2]$$

$$V_{FA} = V_F - V_A = \frac{Q_F + C_G V_G + C_B V_B - (C_G + C_B + C_S) V_A}{C_G + C_A + C_B + C_S}, \quad [3]$$

$$V_{FB} = V_F - V_B = \frac{Q_F + C_G V_G + C_A V_A - (C_G + C_A + C_S) V_B}{C_G + C_A + C_B + C_S}. \quad [4]$$

From these equations and knowing the thickness of the insulators and the interface properties, we can calculate the electron and hole currents that flow through the oxide in each pair of electrodes and can obtain the charge stored at the floating gate, Q_F . We shall not discuss these properties here.

When the negative charge stored at the floating gate is Q_f per unit area, the threshold voltage of the floating gate section of the

device is increased. It can be shown that when the gate is biased with V_G , the charge density at the surface channel of the floating gate section is

$$Q_s = \frac{C_s}{C_g + C_s} [Q_f + C_g (V_G - V_s)], \quad [5]$$

where V_s is the surface potential. The lower case subscripts represent the unit area capacitance or charge density of the corresponding quantities. When the device is at the high threshold voltage state, the surface potential should be smaller than the Fermi potential, ϕ_F , of the bulk silicon under all operation conditions, i.e.,

$$V_{GH} = \phi_F + \frac{C_g + C_s}{C_g C_s} \sqrt{2\epsilon q n_i \phi_F} \exp\left(\frac{q\phi_F}{2kT}\right) - \frac{Q_f}{C_g}, \quad [6]$$

where n_i is the intrinsic carrier density of the silicon.

When this memory transistor is arranged in an X - Y matrix for an electrically alterable read-only memory, the array can be written in many different schemes. One of the write/erase schemes is to group erase all memory transistors to the low threshold state and then write each memory cell individually. We shall examine the following three bias conditions.

Case 1: $V_G = 0$, $V_A = V_{EE/2}$, $V_B = V_{EE}$

Substituting these values of V_G , V_A , and V_B into Eqs. [2] to [4], we obtained

$$V_{FG} = \frac{Q_F + [(C_A/2) + C_B] V_{EE}}{C_G + C_A + C_B + C_S}, \quad [7]$$

$$V_{FA} = \frac{Q_F - [(C_G + C_B + C_S)/2] V_{EE}}{C_G + C_A + C_B + C_S}, \quad [8]$$

$$V_{FB} = \frac{Q_F - [C_G + (C_A/2) + C_S] V_{EE}}{C_G + C_A + C_B + C_S}. \quad [9]$$

Case 2: $V_G = 0$, $V_A = V_{EE}$, $V_B = V_{EE}/2$

Under this bias condition the voltages V_{FG} , V_{FA} , and V_{FB} are given by

$$V_{FG} = \frac{Q_F + [C_A + (C_B/2)] V_{EE}}{C_G + C_A + C_B + C_S}, \quad [10]$$

$$V_{FA} = \frac{Q_F - [(C_G + C_B + C_S)/2] V_{EE}}{C_G + C_A + C_B + C_S}, \quad [11]$$

$$V_{FB} = \frac{Q_F - [(C_G - C_A + C_S)/2] V_{EE}}{C_G + C_A + C_B + C_S}. \quad [12]$$

Case 3: $V_G = V_A = V_{EE}/2$, $V_B = V_{EE}$

The interelectrode voltages in this case are

$$V_{FG} = \frac{Q_F + [(C_B - C_S)/2] V_{EE}}{C_G + C_A + C_B + C_S}, \quad [13]$$

$$V_{FA} = \frac{Q_F + [(C_B - C_S)/2] V_E}{C_G + C_A + C_B + C_S}, \quad [14]$$

$$V_{FB} = \frac{Q_F - [(C_G/2) + (C_A/2) - C_S] V_{EE}}{C_G + C_A + C_B + C_S}. \quad [15]$$

The voltage V_{FG} given by Eq. [7] is very large compared to that given by Eqs. [10] and [13]; therefore, the condition of Case 1 is sufficient to cause gate injection. No gate injection can take place under the bias condition of Cases 2 and 3.

For substrate injection operation, only the voltage V_{FB} is important. It is obvious that the voltage V_{FB} given by Eq. [9] is much larger than that given by Eqs. [12] or [15]. Again, the bias condition of Case 1 can result in substrate injection, while both the bias conditions of Case 2 and Case 3 do not result in a high enough field for substrate injection. There is no charge transfer between the substrate and the floating gate in Cases 2 and 3. However, in this case, the memory is group erased to the high threshold voltage and individually written to the low threshold states.

This memory transistor can be arranged in a X - Y array by using common $n+$ source or drain diffusion lines as bit lines and common control gates as word lines. A 3×3 array is shown in Fig. 2 to demonstrate array operation. As can be seen, the sources of the devices in a given column of memory transistors are connected to the drains of the devices in the adjacent columns to form a bit line, b_j . The gate electrodes of all the memory transistors in a given row are connected together to form a word line W_i .

The array can be group erased to the "0" state (low threshold voltage) by simply applying V_{EE} to the word lines and grounding

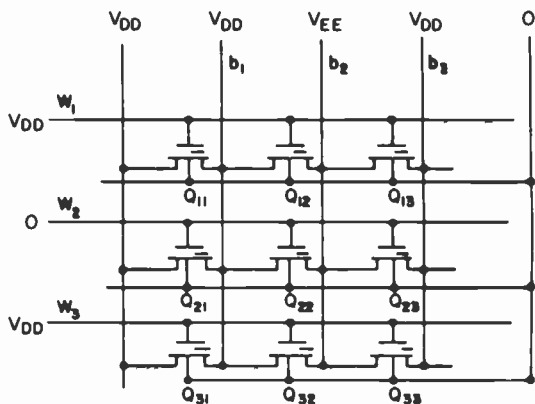


Fig. 2—3 × 3 array of memory transistors.

all other electrodes. To write a “1” (high threshold voltage) to cell Q_{22} , the following biases are required:

$$\begin{aligned}
 V_{wj} &= 0, & \text{when } j &= 2 \\
 &= V_{DD}, & \text{when } j &\neq 2 \\
 V_{bi} &= V_{EE}, & \text{when } i &= 2 \\
 &= V_{DD}, & \text{when } i &\neq 2
 \end{aligned}
 \tag{16}$$

$$V_{sub} = 0.$$

Under these biases, Q_{22} is biased at the condition of Case 1. Q_{23} is biased in condition of Case 2, and all other memory transistors in row 2 are biased at $V_G = 0$ and $V_A = V_B = V_{DD}$. All memory transistors except Q_{22} in column 2 are biased to Case 3 condition. The rest of the memory transistors are biased at $V_G = V_A = V_B = V_{DD}$. Consequently only the floating gate of Q_{22} will be charged with negative charges. There will be no charge transferred to or from the floating gate of any other memory transistor. The same selective write process can be applied to any other memory transistor.

3. Experimental Data

Offset floating gate GIMOS memory devices have been made on SOS substrates. The length l_1 and l_2 , are equal to 4 μm and 3 μm , respectively. The floating gate overlaps the n+ region by 1 μm . The thickness of the upper and lower layer of oxides are equal to 720 \AA and 210 \AA , respectively.

The asymmetrical characteristics of a typical device are shown in Figs. 3 and 4. In Fig. 3 the threshold voltage of the device is plotted as a function of V_E . The operating conditions are shown in the insert

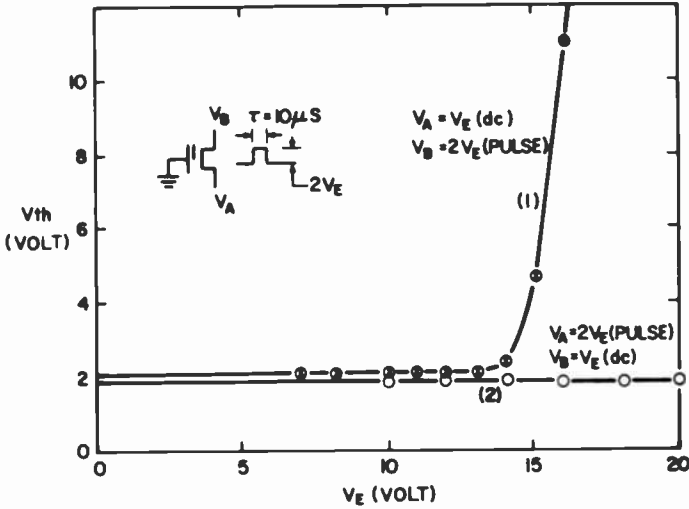


Fig. 3—Threshold voltage of memory device (SOS) as a function of voltage V_E .

of the figure. For the sake of convenience, the threshold voltage was defined as the gate voltage required to produce 1- μ A drain current when the drain voltage is equal to 2 volts. The threshold voltage of the device was measured after each pulse was applied to the tran-

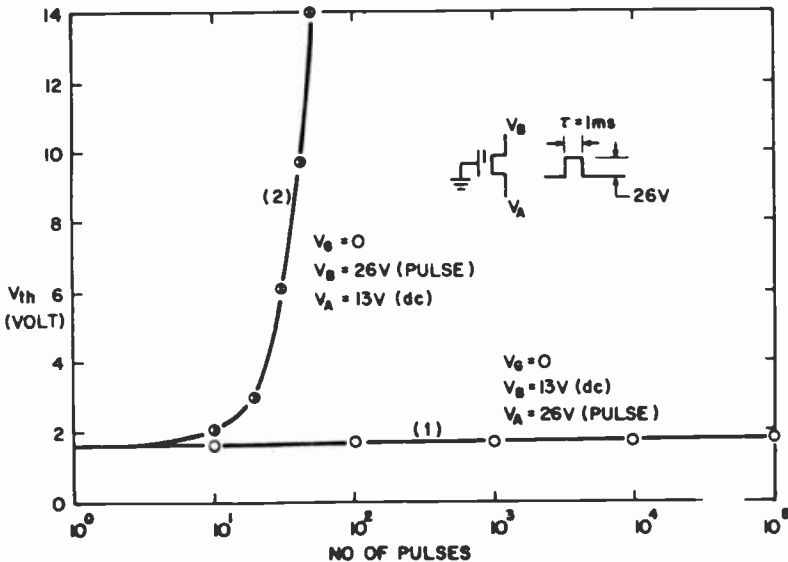


Fig. 4—Threshold voltage of memory device (SOS) as a function of the number of pulses applied.

sistor. If there was a threshold voltage change, the threshold voltage of the transistor was adjusted back to its original value before the next pulse was applied. When the pulse is applied to node B the device can be written if V_E is greater than 13 V. When the pulse is applied to node A, there is no threshold voltage change even if V_E is equal to 20 V.

Fig. 4 shows the threshold voltage of the transistor as a function of number of pulses applied. We selected $V_E = 13$ V, and a pulse width of 1 ms. This data also shows that the device can be written only by applying a high voltage to the control gate and the drain of the transistor.

We programmed p-channel and n-channel SOS offset floating gate GIMOS transistors to threshold voltages of -15 V and $+10$ V, respectively. The devices were stored at 150°C with all electrodes connected together for 1908 days. The threshold voltages of these two devices became -14.0 V and $+9.5$ V, respectively. The threshold voltage of an n-channel SOS GIMOS transistor was written to $+10$ V from its virgin threshold voltage of $+1.2$ V. A voltage of 10 V was applied to the gate with source and drain grounded at 150°C ambient. After 1231 days the threshold voltage of the device was measured to be equal to 9.4 V. The retention time is extremely long. It was also observed that this device is able to sustain more than 30000 write/erase cycles without significant degradation of the device characteristics.

4. Conclusion and Discussion

The offset floating gate SOS GIMOS transistor exhibits excellent asymmetrical write/erase characteristics. The device has very long retention time and exhibits good endurance. This type of nonvolatile memory transistor is suitable for very high density $E^2\text{PROM}$ applications. Although no bulk offset floating gate GIMOS transistors were fabricated, it is expected that they would have the same properties.

During the write and erase operations of this type of $E^2\text{PROM}$, there is no channel current flow in any of the memory transistors. The power consumed by the $E^2\text{PROM}$ during the write/erase operation is very small. Therefore, the high-voltage write/erase signals can be generated on chip. A single-power-supply offset floating gate $E^2\text{PROM}$ is possible. Although the write voltage is large, as was shown in Figs. 3 and 4, a lower write voltage can be achieved by reducing the thickness of the oxide layers and/or building in elec-

tron and hole injectors.⁴ The retention time would be shorter for thinner oxide devices, however.

Acknowledgment

The author would like to express his deep appreciation to M. Jones who fabricated the devices and to J. M. Cartwright who performed the electrical measurements.

References:

- ¹ Y. Tarui, Y. Hayashi, and Nagai, "Electrically Reprogrammable Nonvolatile Semiconductor Memory," *IEEE J. Solid-State Circuits*, **SC-7**, p. 369, 1972.
- ² R. Muller, H. Nietsch, B. Rossler, and E. Wolter, "An 8192-bit Electrically Alterable ROM Employing a One-Transistor Cell with Floating Gate," *IEEE J. Solid-State Circuits*, **SC-12**, p. 507, 1977.
- ³ W. Johnson, G. Pedegos, A. Renninger, G. Kuhn, and T. Ranganath, "A 16kB Electrically Erasable Non-volatile Memory," *IEEE Int. Solid-State Conf. Tech. Digest*, p. 152, 1980.
- ⁴ D. DiMaria, K. DeMeyer, and D. Dong, "Electrically-Alterable Memory Using a Dual Electron Injector Structure," *IEEE Electron Device Lett.*, **EDL-1**, p. 179, 1980.
- ⁵ H. S. Lee and C. H. Teng, "High Electric Field Generated Electron Traps in Oxide Grown from Polycrystalline Silicon," *Appl. Phys. Lett.*, **37**, No. 12, p. 1080, 1980.
- ⁶ S. T. Hsu, "GIMOS—A Nonvolatile MOS Memory Transistor," *RCA Rev.*, **42**, p. 424, 1981.
- ⁷ J. Yeagain and C. Kao, "A High Density Floating Gate EEPROM Cell," *IEEE Int. Electron Devices Meeting Tech. Digest*, p. 24, 1981.

A Study of the Etching Kinetics of Low Carbon Steel Using the Ferric Perchlorate-Perchloric Acid System as a Model

Richard B. Maynard, J. J. Moscony, and M. H. Saunders
Video Component and Display Division, Lancaster, PA 17604

Abstract—The etching of low carbon steel using a ferric perchlorate-perchloric acid medium at constant ionic strength was studied as a simplified model of the system using acidified ferric chloride. Several observations indicate the reaction rate is limited by the rate of encounter of ferric hexaaquo ions with the steel substrate surface. The rate of disappearance of ferric hexaaquo ions is dependent upon the first-order ferric hexaaquo ion concentration and surface area, and inversely dependent upon solution volume and viscosity. The enthalpy of activation (~ 2.8 kcal/mole) is in the range for diffusion of small molecules in solvents of low viscosity. Additionally, the reaction is not inhibited or catalyzed by ferrous ions. A mechanism is proposed to account for these observations.

Introduction

A comparatively recent development in manufacturing technology is the photochemical machining of metals. Briefly, this process consists of applying a patterned stencil onto the surface of an appropriate metal substrate and chemically removing the exposed substrate areas with a suitable etchant. Subsequent removal of the stencil from the substrate produces a finished piece possessing the desired shape or pattern.

During the etching phase of this process, acidified ferric chloride solutions are commonly employed as the chemical etchant. Ferric chloride is cheap and of low toxicity and will react with a variety of metals and alloys. It is particularly useful for etching low carbon

steels which are currently utilized for producing shadow masks for CRT devices.

Although the parameters for the continuation and maintenance of the etching process have been determined on an empirical basis over the years, little appears to be known of the reaction kinetics. An elucidation of the etching kinetics would provide valuable chemical insight into the mechanism(s) responsible and the thermodynamic properties of the system. A search of the available scientific literature revealed many publications on the photo-etching of printed and integrated circuits, but very few dealing with precision piece-parts in ferric chloride etchant.¹ Thus, a study of the reaction kinetics of ferric chloride with low carbon steels appeared warranted.

As the initial step, we decided to study a simplified model of the etching process. Accordingly, we report here results of a study of the beaker etching of low carbon steels in ferric perchlorate-perchloric acid.

Experimental

Ferric and ferrous perchlorates were obtained from Alfa and all other chemicals from GFS Chemicals. All were reagent grade and used as received. Deionized water was used throughout.

Rectangular pieces of 1008 rimmed steel measuring $36 \times 55 \times 0.15$ mm were cleaned by soaking in hot caustic solution, after which they were thoroughly rinsed with deionized water and dried. Variations in the observed rate constant as great as ~15% were noted for steel obtained from different coil numbers.* Accordingly, steel pieces from the same coil were used when varying a particular parameter. No variation in reaction rate due to steel orientation was observed.

The reaction apparatus consisted of a tall one-liter beaker contained in a Plexiglas-CPVC assembly. A grooved Plexiglas cover was fitted over the top of the beaker and secured with wing nuts. The cover was drilled for a sampling port, thermometer port, and a port for the Teflon stirring rod. A piece of steel was attached via the slot in the Teflon stirring rod and connected to a variable speed stirring motor. The entire assembly was weighted and placed in a

* Variations are mainly due to differences in the microstructure of the surface of the steel resulting from the samples' previous history of cold working and heat treatment. In addition to our study, this is also known to have a significant effect on rates of corrosion. For example, see Z. A. Foroulis, *Corros. Sci.*, 5, p. 39 (1965); L. Felloni, *Corros. Sci.*, 8, p. 133 (1968).

constant temperature water bath controlled to $\pm 0.05^\circ\text{C}$ by a Tempette TE-7 heater controller.

In a typical experiment, a one-liter solution 0.75 M in perchloric acid and 5.0×10^{-3} M in ferric perchlorate with lithium perchlorate added to maintain an ionic strength of 1.0 was prepared. A 500-ml portion was thermally equilibrated via stirring with a strip of Mylar sheet attached to the stirring rod. Upon reaching constant temperature, the Mylar strip was replaced with a rectangular piece of 1008 rimmed steel. A 1.00-ml sample of solution was immediately removed and sampling continued once every ten minutes until a total of 15 samples were obtained covering 140 minutes of reaction time. Each sample was analyzed for ferric hexaaquo ion concentration at 240 nm with a Hitachi Model 100-20 Digital Spectrophotometer. Total volume of solution removed was $<4\%$ of the total volume of the reacting solution. The solution was initially stirred at 75 rpm until the 70 minute sample was removed. Then stirring was increased to 125 rpm for the remainder of the sampling period. The above procedure was repeated with the second 500-ml solution except the order of stirring speeds was reversed. However, for the acid concentration and ionic strength variation runs, the stirring speed was kept at 100 rpm for a reaction time of 100 minutes. It was found that at stirring rates above 175 rpm, vortexing began to occur. Consequently, 175 rpm was the highest stirring speed used in any particular run. Stirring speed was maintained to ± 1 rpm with a Power Instruments Model 1891-AM Digital Phototachometer. Pseudo-first-order rate constants were obtained from the ionic concentrations of the samples by plotting $\ln ([\text{Fe}^{3+}]_0/[\text{Fe}^{3+}]_t)$ versus time and evaluating the slope of each appropriate line segment via linear regression analysis. Average observed rate constants were determined from at least three kinetic runs.

Results

The rate of reaction of the ferric hexaaquo ion, Fe^{3+} , with low carbon steel depends, in principle, on the concentration of ferric hexaaquo ions in solution and on the physical characteristics of the steel surface. The simplest expression for the rate of disappearance of the ferric hexaaquo ion from solution is

$$-d[\text{Fe}^{3+}]/dt = k_1[\text{Fe}^{3+}]^\alpha f(\text{Fe}) \quad [1]$$

in which $f(\text{Fe})$ takes into account all the steel surface characteristics that influence this rate. The quantity k_1 is the heterogeneous rate constant and α the reaction order of the ferric hexaaquo ion.

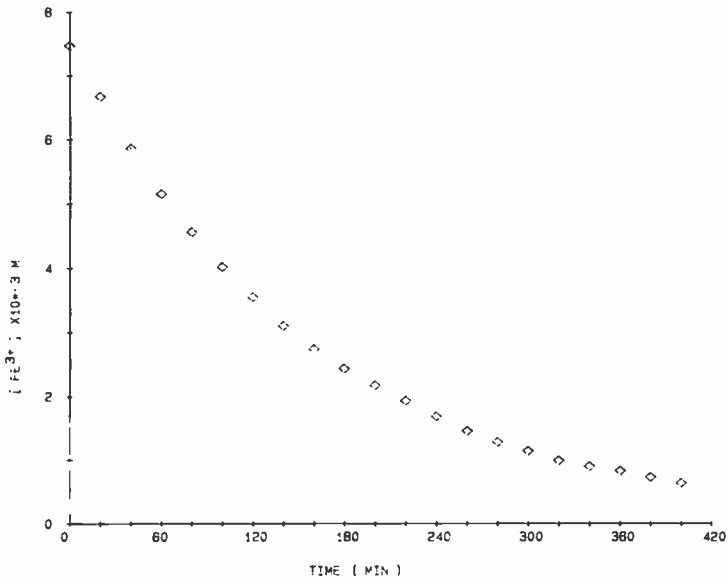


Fig. 1—Plot of the ferric hexaaquo ion concentration versus reaction time for an initial concentration of 7.47×10^{-3} M at 29.8°C and a stirring speed of 75 rpm.

Under the conditions employed to study this reaction, the amount of steel utilized was in excess of the amount of ferric hexaaquo ions capable of totally reacting with it. This being the condition necessary for the reaction to be pseudo-zero-order in iron, we can further simplify Eq. [1] to yield

$$-d[\text{Fe}^{3+}]/dt = k_{obs}[\text{Fe}^{3+}]^\alpha \quad [2]$$

where k_{obs} is the observed rate constant. The manner in which $[\text{Fe}^{3+}]$ varies with time determines the order of the reaction with respect to ferric hexaaquo ion. Since it is usually much easier to measure a concentration than a rate, Eq. [2] is integrated. For the most common case, where $\alpha = 1$, we obtain

$$\ln[\text{Fe}^{3+}]_t = \ln[\text{Fe}^{3+}]_o - k_{obs}t \quad [3]$$

where k_{obs} is the pseudo-first-order rate constant. Thus for a first-order reaction in ferric hexaaquo ion, a plot of $\ln([\text{Fe}^{3+}]_o/[\text{Fe}^{3+}]_t)$ versus time would give a straight line with a slope equal to the pseudo-first-order rate constant.

Fig. 1 is a plot of ferric ion concentration versus time for a reaction initially 7.47×10^{-3} M in ferric ion. For this particular run, samples were taken at 20 minute intervals over a reaction time of

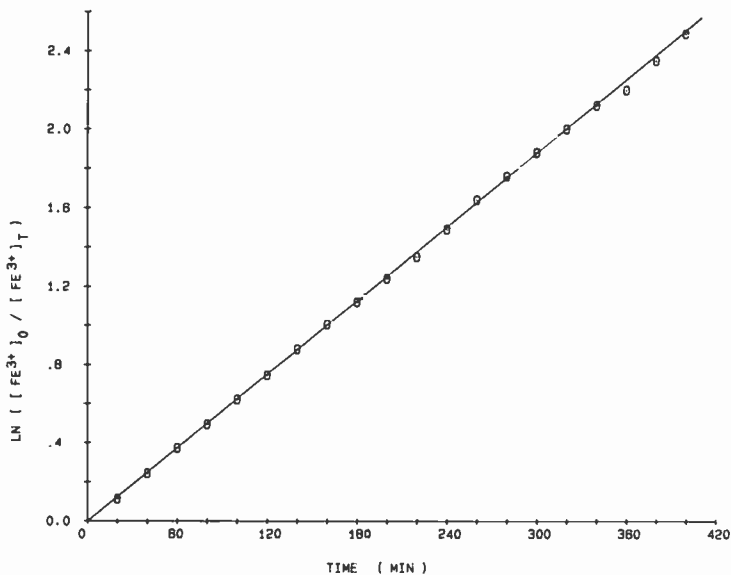


Fig. 2—Plot of $\ln([Fe^{3+}]_0/[Fe^{3+}]_t)$ versus reaction time for the data contained in Fig. 1.

400 minutes and at a stirring rate of 75 rpm. Plotting this data using Eq. [3] produces the straight line plot shown in Fig. 2. This shows that the reaction is first-order in ferric hexaaquo ion over at least 3-1/2 half-lives, or >90% ferric ion consumed in the reaction.

Table 1 contains average observed rate constants obtained at three different initial ferric hexaaquo ion concentrations. These results indicate that the reaction is first-order in the ferric ion, at least over the concentration range of 1.0×10^{-3} – 9.6×10^{-3} M.

Fig. 3 is a typical example illustrating the internal consistency in the experimental protocol utilized. If each opposite side of the parallelogram is of near identical slope and all sides of identical

Table 1—Average Observed Rate Constants at 29.8°C.

Initial $[Fe^{3+}]$ Concentration (M)	Stirring Speed (rpm)	Average Observed Rate Constant (min^{-1})
9.61×10^{-3}	75	$6.46 \pm 0.11 \times 10^{-3}$
	125	$8.80 \pm 0.06 \times 10^{-3}$
4.50×10^{-3}	75	$6.30 \pm 0.12 \times 10^{-3}$
	125	$8.61 \pm 0.06 \times 10^{-3}$
1.0×10^{-3}	75	$6.0 \pm 0.1 \times 10^{-3}$
	125	$8.0 \pm 0.1 \times 10^{-3}$

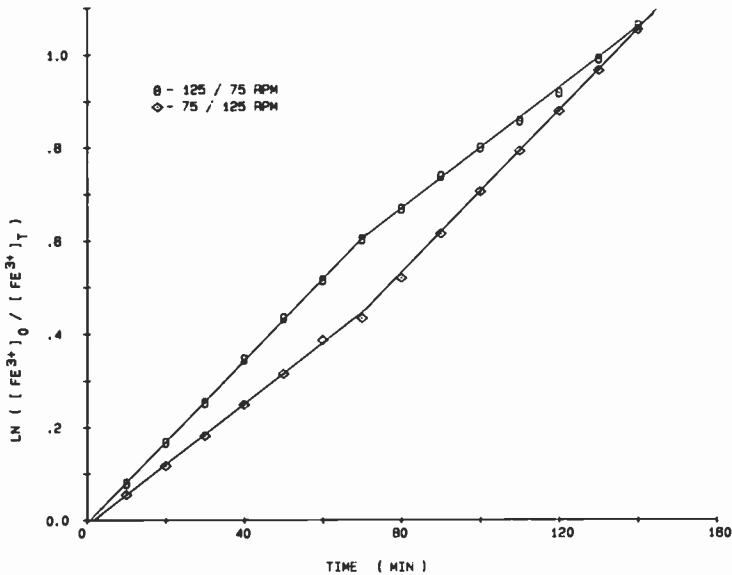


Fig. 3—A representative plot illustrating consistency of kinetic data as described in experimental section.

length, then each particular pair of data points associated with a single etching run should intersect at the 140 minute sampling point. Generally, each pair of stirring speed combinations intersected at or near this point.

The dependency of the observed rate constant upon stirring speed is shown in Fig. 4. Immediately apparent is the increase in the observed rate constant as the stirring speed is increased. This observation is consistent with a reaction following encounter-limited kinetics.* Improved agitation should decrease the thickness of the boundary layer and increase the rate at which ferric ions reach the metal surface.

Further examination of Fig. 4 clearly shows a break in the data points below 75 rpm. Data collected at 75 rpm and above up to 175 rpm falls almost exactly on a straight line. Below 75 rpm, the data falls below this straight line in a roughly linear fashion. Values lower than 25 rpm were not obtained, in part because of the difficulty in maintaining a constant stirring speed with the apparatus used and in part because extrapolation to zero gave the expected

* The rate of encounter is composed of contributions from the mass transport rate of bulk solution to the solution-substrate interface and the rate of diffusion across this interface to the steel surface. In the context of the present work we make no attempt to separate these contributions. Instead we combine them together as the "rate of encounter" or "encounter limited."

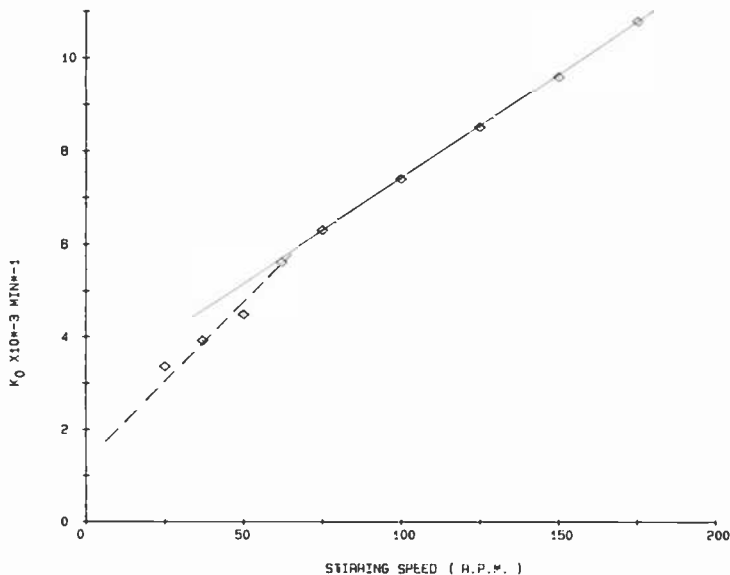


Fig. 4—Dependency of observed rate constant (min^{-1}) on stirring speed at 29.8°C.

low value.† Apparently in the stirring range below 75 rpm, inefficient stirring of the bulk solution occurs.

To determine what effect, if any, ferrous ions had upon the observed rate constant, a series of kinetic runs were executed in which the initial concentration was varied from $2.5 \times 10^{-3} \text{ M}$ to $2.0 \times 10^{-2} \text{ M}$. The results of these runs are contained in Table 2. When all of the observed rate constants are considered together, no discernable systematic behavior as a function of initial ferrous ion concentration is observed.

As a further check of the consistency of these results, a linear regression was performed utilizing the four observed rate constants at the various initial ferrous ion concentrations. Intercepts of 6.26×10^{-3} and 8.47×10^{-3} were obtained at 75 and 125 rpm, respectively. These values compare quite closely with the observed rate constants obtained with no initial ferrous ions present.

Although the presence of ferrous ions has no effect upon the observed rate constant, they are apparently involved in some fashion with the chemistry occurring on the steel surface. This is based on the qualitative observation that increasing the initial ferrous ion

† Even with no stirring the reaction should occur at a finite rate owing to pure diffusion of ferric ions to the metal surface.

Table 2—Average Observed Rate Constant as a Function of Initial Ferrous Concentration at 29.8°C.

Initial [Fe ²⁺] Concentration (M)	Stirring Speed (rpm)	Average Observed Rate Constant (min ⁻¹)
0	75	6.30 ± 0.10 × 10 ⁻³
	125	8.51 ± 0.10 × 10 ⁻³
.0025	75	6.10 ± 0.35 × 10 ⁻³
	125	8.32 ± 0.10 × 10 ⁻³
.0050	75	6.46 ± 0.26 × 10 ⁻³
	125	8.39 ± 0.10 × 10 ⁻³
.010	75	6.10 ± 0.11 × 10 ⁻³
	125	8.63 ± 0.33 × 10 ⁻³
.020	75	6.15 ± 0.34 × 10 ⁻³
	125	8.17 ± 0.08 × 10 ⁻³

concentration formed a heavier coating of a dark colored material on the surface of the steel. This was especially noticeable in runs where an initial ferrous ion concentration ≥ 0.010 M was utilized. A coating on the steel surface might be expected to decrease the surface area available for attack by ferric ions. However, our results did not show any noticeable inhibitory effect on the observed rate constants.

The dependence of the observed rate constant on perchloric acid concentration over the range 0.01–0.90 N was investigated. The observed rate constant was found to be independent of perchloric acid concentration over the range 0.05–0.90 N. This is consistent with the ferric hydrolysis being kept to a minimum. For example, at 0.05 N we found ~1–2% of the total ferric content to be composed of ferric hydrolysis products.

At perchloric acid concentrations between 0.01–0.05 N we were unable to obtain reproducible kinetic runs. These solutions would be initially clear upon mixing, but would gradually acquire a yellow color due to ferric hydrolysis after only a short time at 29.8°C. In addition, solutions allowed to stand for several hours would not etch the rimmed steel, even though spectrophotometric analysis revealed a majority of the solution to contain ferric hexaquo ion.

In addition to varying perchloric acid concentration, we also varied ionic strength over the range 1.0–3.0 with both lithium and sodium perchlorate. The results contained in Table 3 show a non-linear decrease in observed rate constant as the ionic strength increases. A probable cause for the observed behavior is a change in the activity coefficient of the ferric hexaquo ion. This may be due to several factors such as ionic association,² a decrease in ionic mobility,³ or an increase in solution viscosity.⁴

Table 3—Average Observed Rate Constant Versus Ionic Strength at 29.8°C and 100 rpm.

Ionic Strength	Average Observed Rate Constant (NaClO ₄) (min ⁻¹)	Average Observed Rate Constant (LiClO ₄) (min ⁻¹)
1.0	$6.35 \pm 0.05 \times 10^{-3}$	$6.44 \pm 0.10 \times 10^{-3}$
2.0	$6.25 \pm 0.37 \times 10^{-3}$	$6.16 \pm 0.05 \times 10^{-3}$
3.0	$5.46 \pm 0.12 \times 10^{-3}$	$5.47 \pm 0.06 \times 10^{-3}$

Although the range of solution viscosities encountered in this work was very limited, a qualitative correlation with the observed rate constant was noted. Linear regression analysis of the log-log plot in Fig. 5 gives an exponent value of -1.34 ± 0.33 at 75 rpm and -1.00 ± 0.38 at 125 rpm indicating a roughly inverse relation between solution viscosity and observed rate constant.

Several additional parameters affecting the observed rate constant were investigated. Fig. 6 is a log-log plot of the dependence of the observed rate constant on solution volume. It shows that an increase in solution volume produces a decrease in the observed rate constant. Linear regression analysis of the data results in an exponent value of -0.74 ± 0.07 at 75 rpm and -0.76 ± 0.03 at 125 rpm.

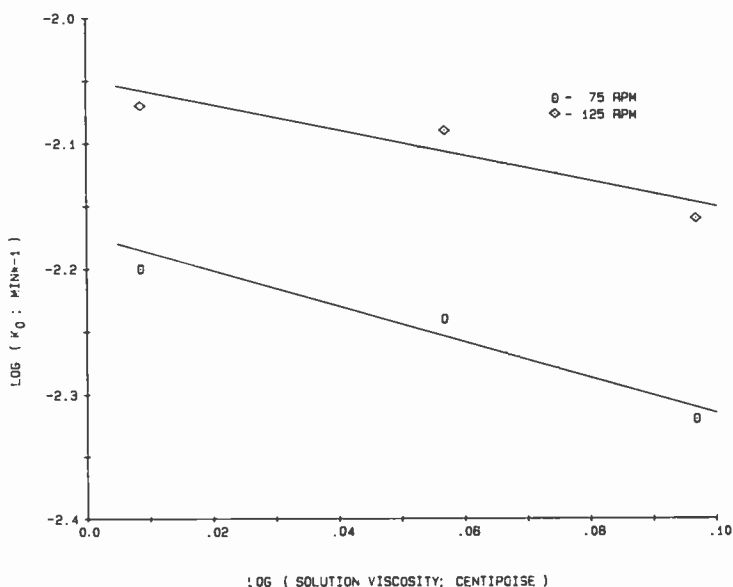


Fig. 5—Log-log plot of observed rate constant versus solution viscosity at 29.8°C.

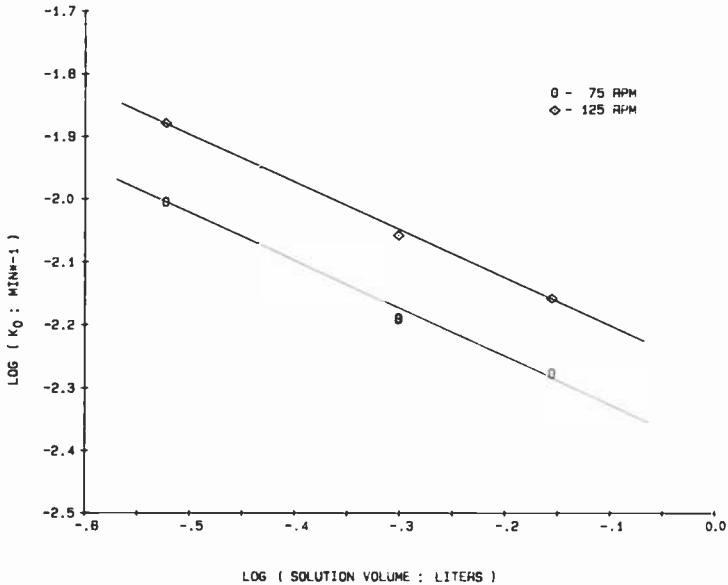


Fig. 6—Log-log plot of observed rate constant versus solution volume at 29.8°C.

Fig. 7 is a log-log plot of the dependence of the observed rate constant on surface area of the steel sample. The surface area was calculated based upon the approximation that each piece of steel was a rectangular solid of infinitely small thickness and that surface roughness was essentially constant from one piece to the next. It was found that the observed rate constant was independent of the orientation of the rectangular pieces relative to the vertical stirring axis. Substituting AK or FS steel produced no change in the observed rate constants determined utilizing 1008 rimmed steel. An examination of Fig. 7 reveals that doubling the surface area of the steel doubles the observed rate constant. Linear regression analysis of the data contained in the log-log plot gives an exponent value of 1.03 ± 0.09 at 75 rpm and 1.02 ± 0.11 at 125 rpm.

The final experimental parameter investigated was the effect of temperature upon the observed rate constant. Shown in Table 4 are the average observed rate constants obtained over the temperature range of 29.8°C to 50.1°C. At the higher temperatures (40.2°C and 50.1°C) hydrogen evolution became more noticeable with bubble formation on the steel surface occurring to a great extent. Although diligent tapping of the stirring rod appeared to minimize rate inhibition due to partial surface coverage, a separate series of runs

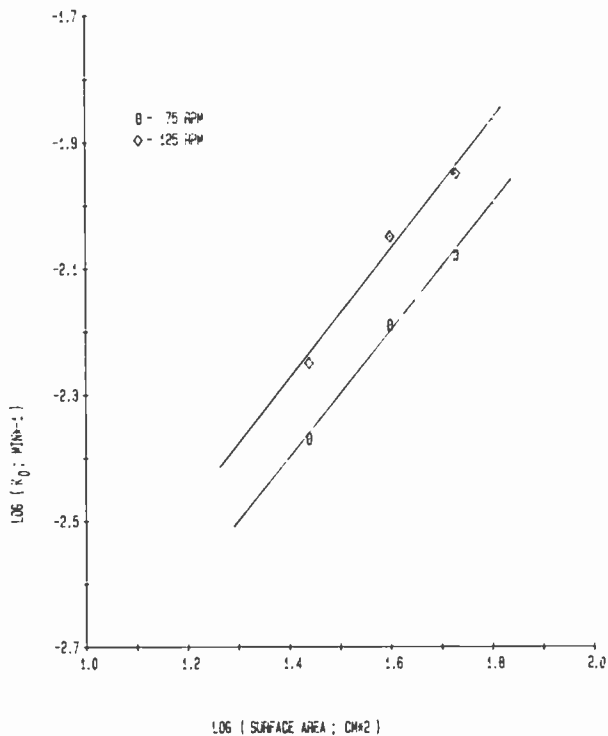


Fig. 7—Log-log plot of observed rate constant versus area of steel piece at 29.8°C.

at 50.1°C were made in which the perchloric acid concentration was lowered from 0.75 to 0.050 N. This result is also contained in Table 4 and shows the observed rate constants at the two acidities to be virtually identical.

The effect of absolute temperature T upon the rate constant k can be described⁵ by the empirical relation

Table 4—Average Observed Rate Constant as a Function of Temperature at Ionic Strength = 1.0.

Temp °K	Average Observed Rate Constant at 75 rpm (sec ⁻¹)	Average Observed Rate Constant at 125 rpm (sec ⁻¹)
303.0 (29.8°C)	$8.60 \pm 0.10 \times 10^{-5}$	$1.10 \pm 0.02 \times 10^{-4}$
313.4 (40.2°C)	$1.07 \pm 0.02 \times 10^{-4}$	$1.38 \pm 0.02 \times 10^{-4}$
323.3 (50.1°C)	$1.25 \pm 0.06 \times 10^{-4}$	$1.56 \pm 0.02 \times 10^{-4}$
323.3 (50.1°C)*	$1.25 \pm 0.02 \times 10^{-4}$	$1.54 \pm 0.04 \times 10^{-4}$

* [HClO₄] = 0.050 N

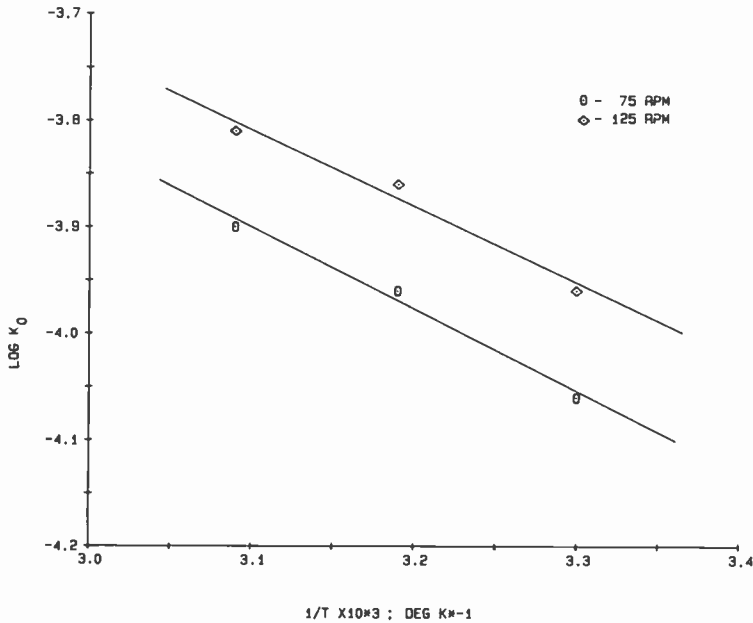


Fig. 8—Temperature dependence of observed rate constant (Arrhenius plot of $\log k$ versus $1/T$).

$$k = A \exp(-E_a/RT) \quad [4]$$

where E_a is the activation energy and A the pre-exponential factor which is related to entropy. Since E_a and A are generally constant over a moderate temperature range, a plot of $\log k$ versus $1/T$ is linear with slope $-E_a/2.3R$ and intercept $\log A$. An Arrhenius plot at two different stirring speeds is shown in Fig. 8 and the activation energies obtained from that plot in Table 5. Since both values are within 2σ of each other, they were averaged to give an activation energy of ~ 3.5 kcal/mole.

Additionally, the free energy (ΔF^\ddagger), enthalpy (ΔH^\ddagger), and entropy (ΔS^\ddagger) of activation can be obtained via the relation

Table 5—Activation Parameters

Stirring Speed (rpm)	E_a (kcal/mole)	ΔH^\ddagger (kcal/mole)	ΔS^\ddagger (eu)
75	3.71 ± 0.27	3.06 ± 0.16	-19.8 ± 0.5
125	3.28 ± 0.51	2.63 ± 0.43	-20.8 ± 1.4

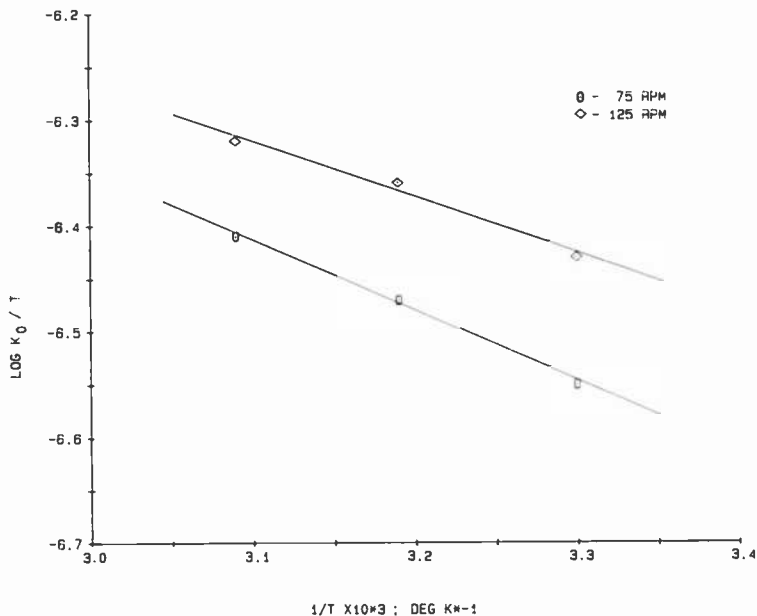


Fig. 9—Temperature dependence of observed rate constant (Eyring plot of $\log(k/T)$ versus $1/T$).

$$k = \frac{KT}{h} \exp\left(\frac{-\Delta F^\ddagger}{RT}\right) = \frac{KT}{h} \exp\left(\frac{-\Delta H^\ddagger}{RT}\right) \exp\left(\frac{\Delta S^\ddagger}{R}\right) \quad [5]$$

where K is Boltzmann's constant, h is Planck's constant, and T is absolute temperature. An Eyring plot of $\log(k/T)$ versus $(1/T)$ is linear with slope $-\Delta H^\ddagger/2.3R$ and intercept $\Delta S^\ddagger/2.3R$. Such a plot is shown in Fig. 9 The enthalpy and entropy of activation at two different stirring speeds are also contained in Table 5. Again, averaging of values gives a ΔH^\ddagger of ~ 2.8 kcal/mole and ΔS^\ddagger of ~ -20 eu.

Discussion

The experimental results presented above indicate a reaction rate that is limited by the rate of encounter of ferric hexaaquo ions with the steel substrate. In particular, we have observed the following qualitative kinetic characteristics* expected for an encounter-limited reaction:

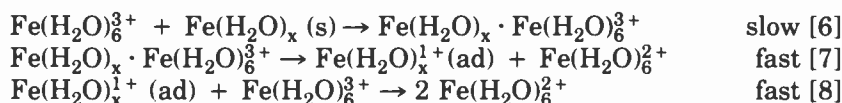
* In order to rigorously prove that a mass-transfer limited reaction is operating under the conditions we have imposed would require an exact analysis of mass transfer to the steel surface as a function of agitation and solution viscosity. Unfortunately, the geometry of the steel we have utilized is sufficiently complicated to preclude such an analysis. For solutions to several simpler geometries see: V. G. Levich, *Physicochemical Hydrodynamics*, Prentice-Hall, Englewood, NJ, 1962, Chapters 2 and 3.

- (1) the observed rate constant is dependent upon stirring speed and surface area of the steel and inversely dependent upon solution volume.
- (2) although not accurately determined, the observed rate constant varies inversely with solution viscosity over a very limited range of viscosities.
- (3) the enthalpy of activation is low.⁶

In addition to the above results related to the encounter-limited aspect of the reaction, we obtained the following results regarding the chemical transformations involved:

- (1) the rate of the reaction is first order in ferric hexaaquo ion.
- (2) the reaction is not inhibited or catalyzed by the addition of excess ferrous ion.
- (3) the small amounts of other metals contained in different low carbon steels, which could dissolve into solution, do not catalyze or inhibit the reaction.
- (4) the observed rate constant is independent of acid concentration over the range of 0.050–0.90 N.

Consideration of these results leads us to propose the following plausible mechanism for the reaction of the ferric hexaaquo ion with steel substrate:



The proposed mechanism consists of the encounter-limited rate-determining step (Eq. [6]) of the ferric hexaaquo ion with the hydrated steel surface, followed by adsorption and a fast electron transfer to form a reactive monovalent iron species. This rapidly reacts with another ferric hexaaquo ion forming additional ferrous products. The negative value for the entropy of activation (Table 5) is consistent with the rate-determining step shown in Eq. [6]. Additionally, it should be recognized that the rate-determining step, as depicted in Eq. [6], is composed of the mass transport and diffusion processes required to transport a ferric hexaaquo ion in the bulk solution to the surface of the steel substrate.

Since the kinetic data will give information on the mechanism only up to and including the rate-determining step, the fast reactions following it are conjecture. However, several pieces of additional evidence do provide plausibility for Eqs. [7] and [8] as possible reaction steps. First, the formation of a monovalent iron species

adsorbed onto the surface has been implicated in a number of corrosion studies as a reactive intermediate.⁷ Although we can't rigorously exclude a soluble Fe(I) species desorbed from the steel surface, we consider it rather unlikely due to the reactivity of such a species. The majority of results lend support for the transitory existence of this species. Secondly, the reaction stoichiometry requires two ferric ions to be reduced for each iron atom oxidized. Since the reaction is first order in ferric hexaquo ion, this indicates the second ferric hexaquo ion reacts in a fast step following the rate-limiting step. Lastly, it is of interest to note that desorption of the ferrous species must be faster than adsorption, since added ferrous ion produces no inhibitory effect upon the observed rate constant.

It is apparent from the above analysis that a variety of chemical and hydrodynamic factors are involved in the reaction rate. According to our proposed mechanism, the faster ferric ions can be transported from the bulk phase to the surface of the steel, the faster the rate of reaction should become, at least up to the point where the rate of transport and adsorption becomes comparable to the rate of desorption and transport away of reaction products.

Although the model system utilized in this study is a great simplification of the actual process, it does provide insight into the dynamics of the etching process. In the next paper in this issue of *RCA Review* we describe results of beaker etching low-carbon steels in concentrated ferric chloride solution.

References:

¹ D. M. Allen, A. J. Hegarty, and D. F. Horne, "Surface Textures of Annealed AISI 304 Stainless Steel Etched by Aqueous Ferric Chloride-Hydrochloric Acid Solutions," *Trans. Inst. Met. Finish.*, **59**, p. 25 (1981).

² J. E. Prue, "Ion Pairs and Complexes: Free Energies, Enthalpies and Entropies," *J. Chem. Ed.*, **46**, p. 12 (1969).

³ W. Jost, *Diffusion in Solids, Liquids, and Gases*, p. 472, Academic Press, Inc., New York (1952).

⁴ Walter J. Moore, *Physical Chemistry*, p. 939, 4th ed., Prentice Hall, New Jersey (1972).

⁵ Ralph G. Wilkins, *The Study of Kinetics and Mechanisms of Reactions of Transition Metal Complexes*, pp. 79-81, Allyn and Bacon, Inc., Boston (1974).

⁶ Enthalpies of activation for diffusion of molecules of low molecular weight in solvents of low viscosity are small, generally in the range 1-4 kcal/mole. See S. W. Benson, *Foundation of Chemical Kinetics*, Vol. 1, p. 253, C. H. Bamford and C. F. H. Tipper, Eds., Elsevier, Amsterdam (1969).

⁷ For several recent results, see G. T. Barstein and D. H. Davies, "The Electrochemical Behavior of Scratched Iron Surfaces in Aqueous Solutions," *J. Electrochem. Soc.*, **128**, p. 33 (1981); M. Keddani, O. R. Mattos, and H. Takenouti, "Reaction Model for Iron Dissolution Studied by Electrode Impedance," *ibid.*, **128**, p. 257 (1981); S. M. Reshetnikov, "Mechanism of Anodic Dissolution of Iron in Inhibited Hydrochloric Acid Solution," *Z. Prikl. Khim.*, **54**, p. 586 (1981).

Ferric Chloride Etching of Low Carbon Steels

Richard B. Maynard, J. J. Moscony, and M. H. Saunders

Video Component and Display Division, Lancaster, PA 17604

Abstract—Beaker etching kinetics of low carbon steels (mainly 1008 rimmed steel) in ferric chloride-hydrochloric acid etchant are reported. A mechanism consisting of predominately transport-limited kinetics at low Baumé ($\sim <40^\circ$ Bé) and predominately surface-limited kinetics at high Baumé ($\sim >54^\circ$ Bé) is proposed. Activation parameters are: 32.0° Bé, $\Delta H^\ddagger = +3.07 \pm 0.13$ kcal/mole, $\Delta S^\ddagger = -25.3 \pm 0.3$ eu; 57.0° Bé, $\Delta H^\ddagger = +10.9 \pm 0.5$ kcal/mole, $\Delta S^\ddagger = -7.2 \pm 1.2$ eu. Chloride ion concentration was found to inhibit etch rate, particularly at high Baumé. Surface finish of etched pieces exhibit a transition Baumé region where surface roughness abruptly increases from ~ 6 -7 microinches to well over 25 microinches. The transition Baumé region increases with an increase in temperature.

Introduction

The use of acidified ferric chloride solutions for etching metals is a widely utilized industrial process for producing burr-free precision piece-parts. In addition, it is one of several etchants utilized by the printed circuit industry in the production of printed and integrated circuit boards. Ferric chloride as an etchant is not only cheap and of low toxicity, but also reacts with a variety of metals and alloys. At RCA, it is currently utilized in the production of shadow masks for CRT devices from low carbon steels.

Recently we have become interested in the etching kinetics of ferric chloride with low carbon steels in the hope of gaining chemical insight into the mechanism and thermodynamic properties of this system. Our initial study focused on a simplified system using ferric perchlorate-perchloric acid as the etching medium.¹ This

etchant was utilized to simplify the number of ferric species present and to allow the reaction to be followed via UV spectrophotometry. From the results of that study, we postulated a mechanism consistent with an encounter-limited reaction rate between ferric ions and a steel substrate.

To model the actual process more precisely, we then substituted for the ferric perchlorate-perchloric acid etching medium a concentrated ferric chloride solution acidified with hydrochloric acid. In this paper we describe results of beaker etching low carbon steels (mainly 1008 rimmed steel) with ferric chloride etchant as a function of etchant concentration, temperature, and added chloride ions.

Experiment

Rectangular pieces of various steels measuring 36×52 mm were used. All were 0.15 mm in thickness except the FS steel which was 0.10 mm thick. All were cleaned by soaking in hot caustic solution, thoroughly rinsed with deionized water, and dried. Ferric chloride concentration was obtained via measurement of etchant density utilizing hydrometers calibrated with the heavy Baumé scale. Both specific gravity and molar concentration of ferric chloride can be interpolated by reference to standard tables.

Stock solutions of ferric chloride etchant were obtained and analyzed for ferrous chloride, ferric chloride, and free acid concentration. Higher Baumés were obtained by boiling water off the stock etchant and lower Baumés prepared by appropriate dilution with hydrochloric acid and deionized water. Except where noted, free acid concentrations were adjusted to 0.040 M.

Viscosity measurements were performed with a Brookfield LVF Viscometer with a modified ultra-low viscosity adapter. The modified adapter contained a titanium insert with an internal diameter of 2.4 cm and a Teflon #1 LV spindle used in place of the ultra-low spindle. The modified adapter was calibrated with a Brookfield viscosity standard. All viscosity measurements were taken at a shear rate of 60 rpm with the scale covering a range of 0–50.5 centipoise.

The reaction apparatus consisted of a tall one-liter beaker contained in a Plexiglas-CPVC assembly. A grooved Plexiglas cover was fitted over the top of the beaker. The cover was drilled for a thermometer port and for a Teflon stirring-rod port. A piece of steel was attached via a slot in the Teflon stirring rod and connected to a variable speed stirring motor. The entire assembly was weighted and placed in a constant-temperature water bath controlled to $\pm 0.05^\circ\text{C}$ by a Tempette TE-7 heater controller.

In a typical experiment, a 0.5 liter solution of etchant was ther-

mally equilibrated to the desired temperature by stirring with a strip of Mylar attached to the Teflon stirring rod. Upon reaching constant temperature, the Mylar strip was replaced with a pre-weighed rectangular piece of steel. Depending on the temperature and Baumé, the steel was allowed to react until ~ 0.1 – 0.4 grams had etched away, a time generally in the range 2–6 minutes. Upon completion of an etch run, the steel sample was immediately rinsed with deionized water, dried and weighed. At least three pieces of steel were etched at each temperature and Baumé utilizing the same etchant sample. Stirring speed was maintained to ± 1 rpm with a Power Instruments Model 1981-AM Digital Phototachometer. Surface roughness measurements were made on a Bendix Type QC profilometer. Baumé measurements were made with Baumé hydrometers calibrated to 0.1° .

Etch rates ($\text{g}/\text{cm}^2\text{-sec}$) were calculated from the weight of material etched away per apparent surface area of sample and reaction time. Heterogeneous rates (cm/sec) were determined by dividing etch rates by the specific gravity of the steel.

Results

Fig. 1 shows the average etch rates* for beaker etching 1008 rimmed steel at five temperatures covering the range 40 – 80°C (104 – 176°F) and degrees Baumé over the range 30 – 58 . Standard deviations are generally on the order of 1 – 4% of the reported value for the curves over 40 – 70°C . However, at 80°C , standard deviations in excess of 10% were noted for many of the reported etch rates. This was mainly the result of an increase in experimental difficulties encountered at this temperature. As a result, the values contained in the 80° curve show considerably more scatter than those obtained at lower temperatures. Minor eccentricities in the stirring rod on the order of several millimeters appeared to have no discernable effect upon etch rate.

In separate experiments it was found that pieces of steel etched under identical conditions for different times (1 – 5 minutes) had nearly identical etch rates. No dependence of etch rate upon the order of samples etched during a kinetic experiment was noted.

A representative sample from each kinetic experiment was measured for surface roughness. The results covering the Baumés of interest are shown in Fig. 2. At each temperature a sharply defined transition from smooth (<10 microinches) to rough (>10 microinches) surface finish is observed. The transition Baumé at which

* Except where noted, all kinetic experiments utilized a stirring rate of 100 rpm.

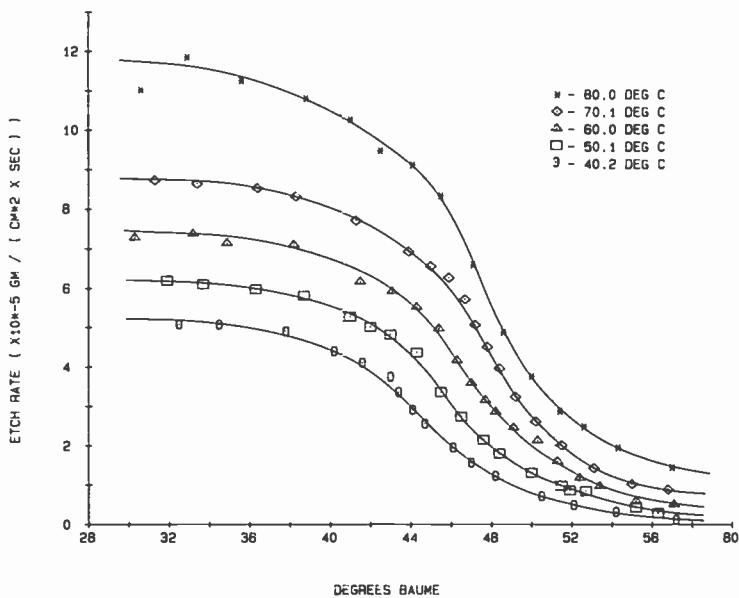


Fig. 1—Average etch rates (g/cm²-sec) for 1008 rimmed steel as a function of Baumé and temperature.

this occurs is temperature dependent, increasing approximately one degree Baumé for every 10°C increase in temperature up to 70°C. Only a slight increase is then observed upon increasing the temperature from 70° to 80°C. Coincident with the increase in surface roughness is the appearance of smut upon the steel surface. The nonuniformity in the surface coverage by the smut is probably a contributing factor to the rough finish. Additionally, the roughness appears to increase with temperature.

From the temperature dependent data in Fig. 1, activation parameters were determined from heterogeneous rate constants obtained in the following manner. A "best-fit" curve was hand fitted to each temperature-dependent set of data points from 40.2° to 70.1°C in Fig. 1. Due to the scatter in the data points at 80.0°C these were not included in the calculation of activation parameters. The rate constants at 32.0° and 57.0° Bé were taken directly off each curve. Each rate constant was divided by the specific gravity of 1008 rimmed steel (7.87 g/cm³) to give the heterogeneous rate constants contained in Table 1.

The effect² of absolute temperature T upon the heterogeneous rate k_h can be described by the empirical relation

$$k_h = A \exp \{ -E_a/RT \} \quad [1]$$

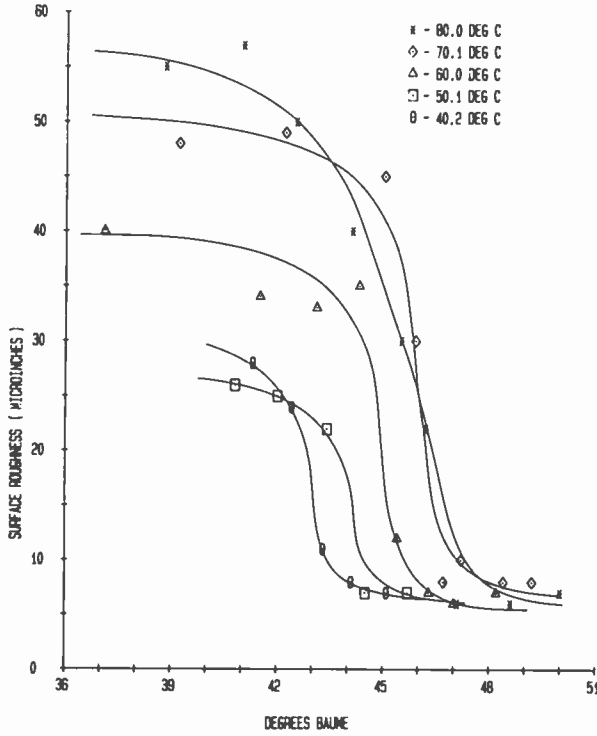


Fig. 2—Average surface roughness for 1008 rimmed steel as a function of Baumé and temperature.

where E_a is the activation energy and A the pre-exponential factor which is related to entropy. Since E_a and A are generally constant over a moderate temperature range, a plot of $\log k_h$ versus $1/T$ is linear with slope $-E_a/2.3R$ and intercept $\log A$. An Arrhenius plot of 32.0° Bé is shown in Fig. 3 and activation energies obtained at 32.0° and 57.0° Bé are contained in Table 2.

Table 1—Observed Heterogeneous Rate Constant as a Function of Temperature for 1008 Rimmed Steel at a Stirring Rate of 100 RPM.

Temp (°K)	Observed Heterogeneous Rate Constant at 32.0° Bé ($\times 10^{-6}$ cm/sec)	Observed Heterogeneous Rate Constant at 57.0° Bé ($\times 10^{-7}$ cm/sec)
313.4 (40.2°C)	6.54	2.06
323.3 (50.1°C)	7.85	3.94
333.2 (60.0°C)	9.34	6.49
343.3 (70.1°C)	11.0	10.5

Table 2—Activation Parameters

Baumé	E_a kcal/mole	ΔH^\ddagger kcal/mole	ΔS^\ddagger (eu)
32.0°	+3.69 ± 0.12	+3.07 ± 0.13	-25.3 ± 0.3
57.0°	+11.5 ± 0.5	+10.9 ± 0.5	-7.2 ± 1.2

Alternatively, the free energy (ΔF^\ddagger), enthalpy (ΔH^\ddagger), and entropy (ΔS^\ddagger) of activation can be obtained from the relation

$$k_h = \frac{KT}{h} \exp\left(\frac{-\Delta F^\ddagger}{RT}\right) = \frac{KT}{h} \exp\left(\frac{-\Delta H^\ddagger}{RT}\right) \exp\left(\frac{\Delta S^\ddagger}{R}\right) \quad [2]$$

where K is Boltzmann's constant, h is Planck's constant, and T is absolute temperature. An Eyring plot of $\log(k_h/T)$ versus $1/T$ is linear with slope $-\Delta H^\ddagger/2.3R$ and intercept $\Delta S^\ddagger/2.3R$. Such a plot at 57.0° Bé is shown in Fig. 4. Enthalpy and entropy of activation energies at 32.0° and 57.0° Bé are tabulated in Table 2.

The effect of added chloride ions, as either hydrochloric acid or lithium chloride, was investigated and the results are given in Table 3. Three different Baumés were chosen as representative of the low, medium, and high Baumé regions. The resultant etch rates

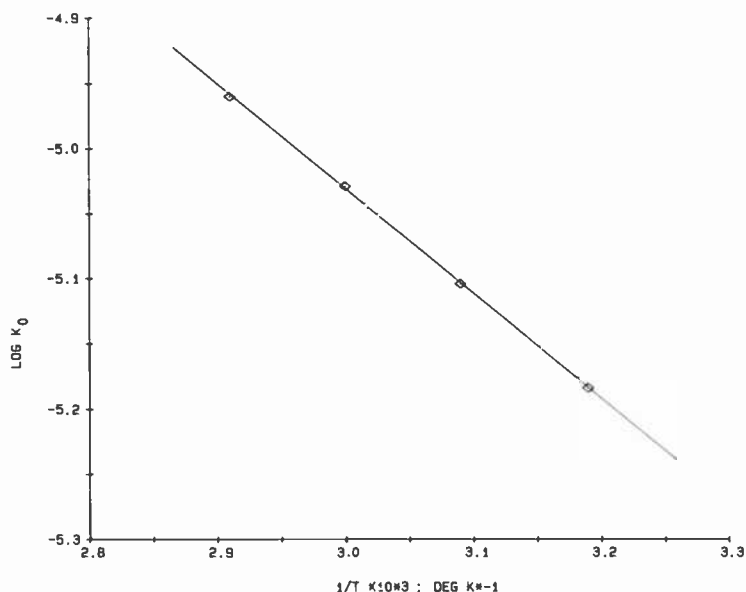


Fig. 3—An Arrhenius plot of $\log k$ versus $1/T$ (°K) at 32.0° Baumé for 1008 rimmed steel.

Table 3—Etch Rates for 1008 Rimmed Steel at 50.1°C and 100 RPM (Initial Free Acid Concentration 0.010 M)

Added		Baumé	Etch Rate ($\times 10^{-5}$ g/cm ² -sec)	% Change from Standard Etch-Rate Curve
HCl (M)	LiCl (M)			
Low Baumé Region				
0.23		40.7	5.27 \pm 0.13	-1.3
	0.23	40.8	5.21 \pm 0.14	-1.9
0.46		39.9	5.41 \pm 0.13	-2.2
	0.46	40.0	5.25 \pm 0.10	-4.7
Medium Baumé Region				
0.012		47.3	2.34 \pm 0.02	+1.3
	0.012	47.4	2.29 \pm 0.06	+1.5
0.058		47.5	2.28 \pm 0.04	+3.6
	0.058	47.5	2.25 \pm 0.01	+2.3
0.23		47.4	2.20 \pm 0.01	-2.6
	0.23	47.6	2.13 \pm 0.04	-0.9
0.46		46.4	2.48 \pm 0.02	-11.1
	0.46	46.5	2.45 \pm 0.02	-10.6
High Baumé Region				
0.053		53.7	0.688 \pm 0.006	+1.3
	0.053	53.3	0.764 \pm 0.017	+2.7
0.11		53.7	0.621 \pm 0.004	-8.5
	0.11	54.0	0.568 \pm 0.007	-9.8
0.21		54.5	0.484 \pm 0.012	-14.4
	0.21	54.4	0.461 \pm 0.008	-18.4

were then compared to corresponding etch rates at the same Baumé obtained from the data in Fig. 1.

Upon examination of the results in Table 3 two trends become evident. First, the etch rate at a particular Baumé is dependent upon added chloride ion concentration irrespective of whether it is added as hydrochloric acid or lithium chloride. This appears to indicate that etch-rate depression is not a function of free-acid concentration. Apparently, the only role free-acid concentration plays is to insure a low pH to prevent ferric hydrolysis and the subsequent formation of solid iron hydroxides. Secondly, as the Baumé is increased, the concentration of added chloride ion necessary to decrease the etch rate decreases. For example, in the low Baumé region (40° Bé), an added chloride ion concentration of 0.46 M produces, at most, a slight etch-rate depression. However, in the high Baumé region (54° Bé), an added chloride ion concentration of 0.11 M decreases the etch rate approximately 10%. Further reductions are noted at higher chloride ion concentrations.

Besides 1008 rimmed steel, several other low carbon steels were briefly investigated. Table 4 gives the heterogeneous etch rates for five other low carbon steels etched in ferric chloride under similar

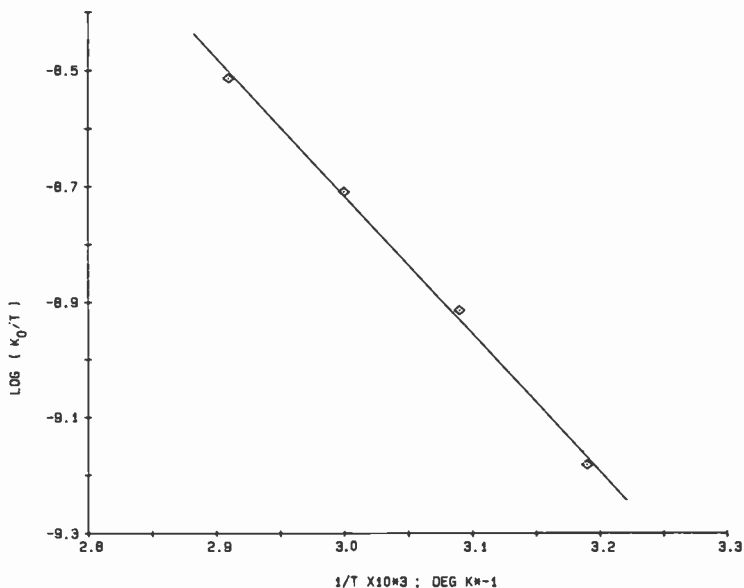


Fig. 4—An Eyring plot of $\log (k/T)$ versus $1/T$ ($^{\circ}\text{K}$) at 57.0° Baumé for 1008 rimmed steel.

conditions of Baumé and temperature. All five steels etched at approximately the same rate as 1008 rimmed steel.

The similarity in etching characteristics of low carbon steels is readily seen in Figs. 5 and 6. Shown in Fig. 5 are etch rates for two steels as a function of Baumé at 70.1°C . Within the accuracy of our experiments, the etch rates for both steels are identical. Fig. 6 shows surface roughness measurements as a function of Baumé at 70.1°C . As observed for 1008 rimmed steel, a sudden increase in surface roughness is observed for 1005AK steel. Both steels show this increase at approximately the same Baumé.

Table 4—Heterogeneous Etch Rates for Various Steels at 46.7° Bé and 70.1°C

Steel	Heterogeneous Etch Rate ^a ($\times 10^{-6}$ cm/sec)
1008 rimmed	7.27 ± 0.25
1005AK	7.19 ± 0.10
1001AK	7.37 ± 0.17
FS ^b	6.78 ± 0.17
ARMCO-IF	6.85 ± 0.21
AK-AOD	7.27 ± 0.22

^a stirring speed = 100 rpm

^b 4 mils thick

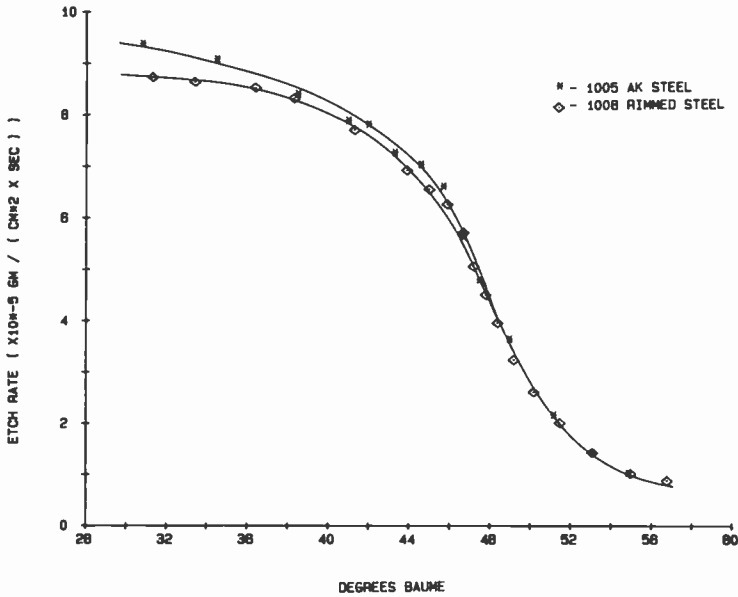


Fig. 5—Average etch rates ($\text{g}/\text{cm}^2\text{-sec}$) for 1005AK and 1008 rimmed steel as a function of Baumé at 70.1°C .

In addition to etch rates, we were also interested in the variation of viscosity of the etchant as a function of Baumé and temperature. These results are summarized in Fig. 7. As expected, the viscosity of the etchant increased as the Baumé increased. This results from the increase in dissolved material (ferric chloride) per unit volume which subsequently requires an increase in the force applied per unit area to maintain the same velocity gradient.³

Unexpected, however, was the appearance of a shoulder in the high Baumé region at high temperature. This gradually grew into a peak and shifted to a higher Baumé as the temperature decreased. Apparently a reorganization of the interactions between the ferric chloro species present and the solvent occurs over this particular Baumé region. We did observe, upon lowering the Baumé from $\sim 60^\circ$ through the region where the peak occurred, that more water than usual was required to produce the Baumé lowering. This suggests a change in the partial molar volume of the solvent resulting from a change in the solution structure. This could be the result of changes in the hydration sphere of a ferric chloro species which would alter the shape and/or size of the ferric chloro molecule. In turn, this would require the water molecules in the bulk solution to reorganize in order to accommodate this new species, producing the requisite change in partial molar volume.

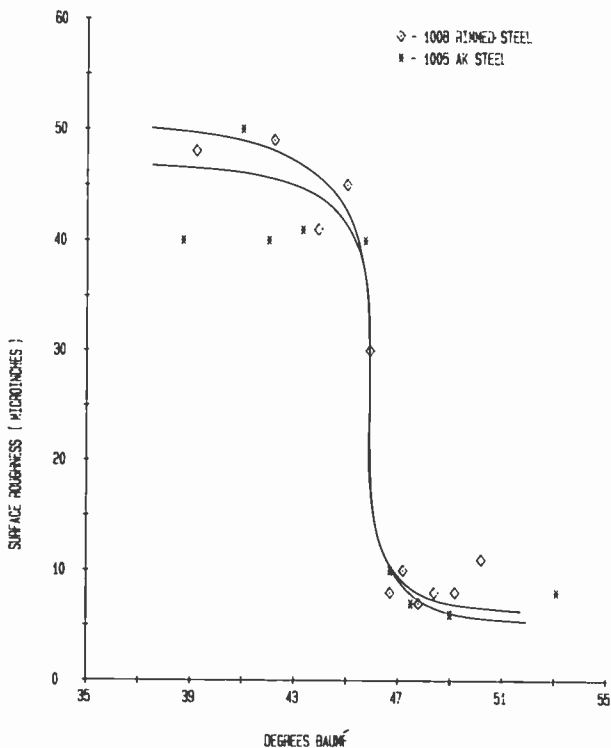


Fig. 6—Average surface roughness for 1005AK and 1008 rimmed steel as a function of Baumé at 70.1°C.

Discussion

The shape of the curves in Fig. 1 suggests to us a reaction where the mechanism is different at low and high Baumés. In these Baumé regions the etch rate changes very gradually, indicating the predominance of one mechanism over the other. Etch rates at intermediate Baumés are then composed of varying degrees of the two mechanisms producing a rapidly changing etch rate as Baumé is varied.

In the low Baumé region (32.0° Bé), an enthalpy of activation of $+3.07 \pm 0.13$ kcal/mole and an entropy of activation of -25.3 ± 0.3 were found. Diffusion of small molecules in solvents of low viscosity typically display enthalpy-of-activation values in the range $+1$ to 4 kcal/mole.⁴ Also found in this Baumé region was a strong dependence of etch rate upon stirring (see Fig. 8) and surface area of the steel sample (see Table 5). These results suggest a reaction rate that is limited by the rate of encounter of ferric chloro species

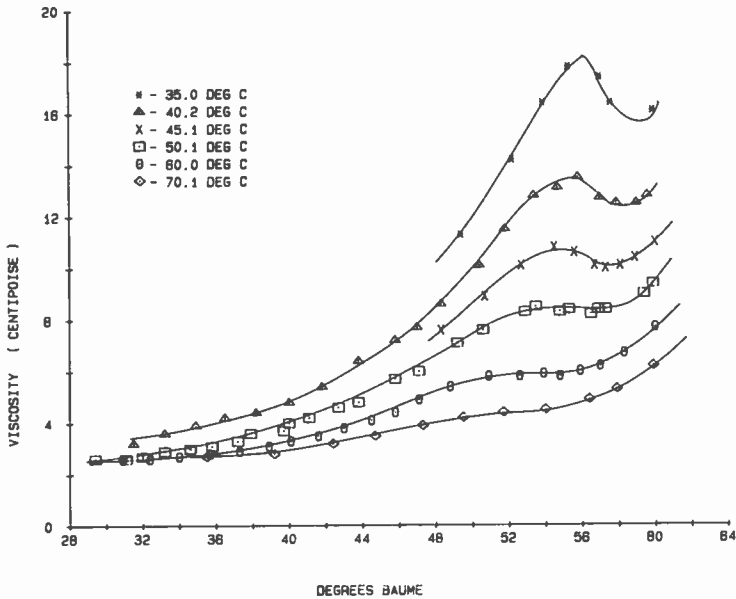


Fig. 7—Ferric Chloride viscosity (centipoise) as a function of Baumé and temperature.

with the steel substrate. Since the rate of encounter contains contributions from both mass transport and diffusion, we have, for convenience, followed the convention of others⁵ and termed this rate-limiting process as “transport-limited” kinetics.

Additionally, the enthalpy and entropy of activation values are quite similar to those found for the ferric perchlorate-perchloric acid etch system described in Ref. [1]. In that system we observed transport-limited kinetics and proposed a mechanism involving transport of ferric ion from bulk solution to the steel surface as the rate determining step. On the basis of the above results, it appears highly

Table 5—Average Etch Rate as a Function of Steel Surface Area at 60.0°C (Stirring Rate = 100 RPM)

Surface Area (cm ²)	Average Etch Rate (× 10 ⁻⁵ g/cm ² -sec)
34.3° Bé	
28.1	7.94 ± 0.34
54.1	9.57 ± 0.10
55.9° Bé	
27.5	0.608 ± 0.009
54.4	0.620 ± 0.012

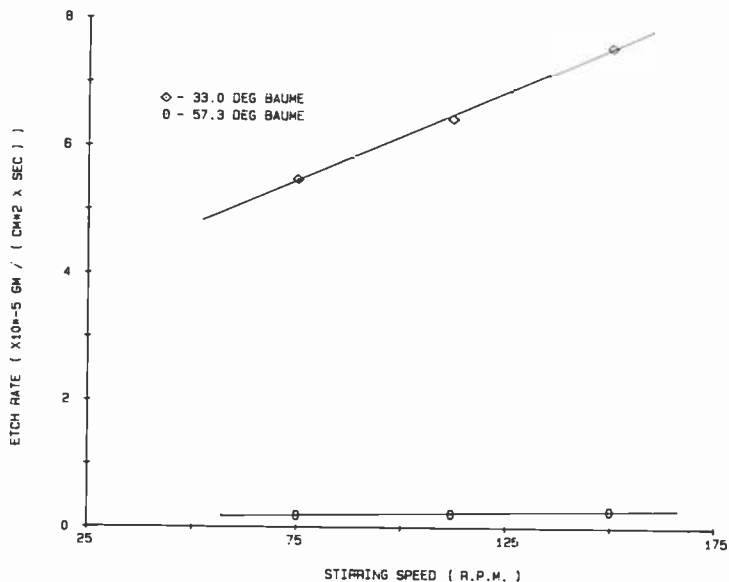


Fig. 8—Average etch rate (g/cm²-sec) as a function of stirring speed at 33.0° and 57.3° Baumé at 50.1°C.

plausible to us that a similar rate-determining step involving ferric chloro specie(s) occurs in the low Baumé region.

In the high Baumé region, the kinetics are different from those observed in the low Baumé region. Unfortunately, the kinetic parameters for the high Baumé region could not be determined at a Baumé where the curves in Fig. 1 level out. This was due to the difficulty in keeping highly concentrated ferric chloride in solution. As a result, the kinetic results determined at 57.0° Bé do exhibit a slight contribution from the transport-limited kinetics occurring in the low Baumé region.

Nevertheless, an enthalpy of activation of $+10.9 \pm 0.5$ kcal/mole is too high for a diffusion controlled reaction. If diffusion is important, then the etchant viscosity should influence etch rate.⁶ A comparison of etch rates at high Baumé (Fig. 1) with etchant viscosity (Fig. 7) indicates viscosity has a very limited effect upon etch rate, particularly at higher temperatures. If it did, then the shoulder observed in Fig. 7 should manifest itself in the etch rate curves. An examination of Fig. 1 reveals it does not. Instead, the enthalpy of activation falls into the range observed for processes dominated by adsorption. Energies of adsorption are generally in the range from about 9 to 100 kcal/mole.⁷

Further results reveal the etch rate to be virtually independent of stirring rate (Fig. 8)⁸ and surface area of the steel sample (Table

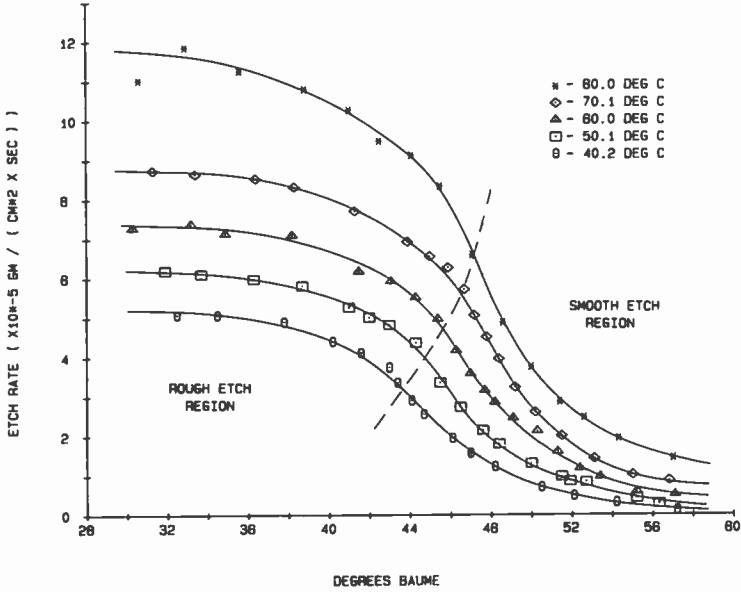


Fig. 9—Plot of Baumé and temperature combinations for smooth and rough etch.

5). All these results are consistent with reaction kinetics slower than transport limited and suggest to us a rate-limiting process involving surface reactions. This could involve adsorption of reactant, chemical reaction with surface iron atoms, desorption of products, or a combination of these processes. Since our present study doesn't allow us to choose which of the above processes are responsible for the rate-determining step, we have instead termed this rate-limiting process as "surface-limited" kinetics.

An apparent physical manifestation of the change in reaction mechanism from surface-limited kinetics to transport-limited kinetics is the sudden appearance of a nonuniform coating of smut on the surface of the etched pieces. This in turn, we believe, is responsible for the resultant increase in surface roughness seen in Fig. 2. Combining the results contained in Figs. 1 and 2 produces Fig. 9, which illustrates the various combinations of temperature and Baumé for obtaining either a smooth or rough surface finish.

The difference between a smooth and rough finish as the transition Baumé is passed is shown pictorially in the series of SEM topography photographs in Fig. 10. From top to bottom in the figure, an approximate six-fold increase in surface roughness is observed for a decrease of only 1.5° Bé. Knowledge of the transition Baumé could be important in etching, for example, the aperture openings in a shadow mask.

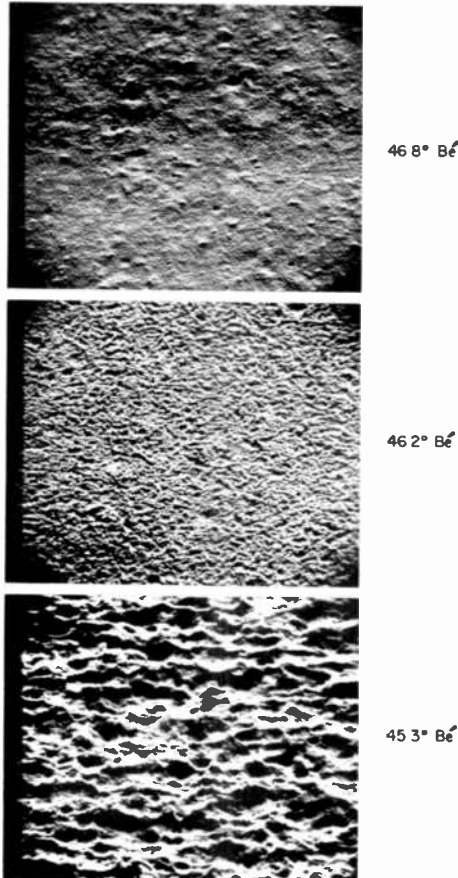


Fig. 10—SEM topography photographs of 1008 rimmed steel etched at 80°C. Sample surface roughness from top to bottom is, in microinches, 7 ± 1 , 22 ± 2 , and 45 ± 5 . Original photos were at $500 \times 45^\circ$ and have been reduced roughly by half here.

A possible explanation for the change in reaction mechanism as Baumé is varied involves a change in the identity of the reacting ferric chloro species. For example, upon increasing the Baumé at 25°C from 32° to 61° Bé, the ferric concentration increases from 2.3 to 6.8 M. Several different groups⁹⁻¹¹ utilizing Raman, ESR, and solution x-ray diffraction techniques upon concentrated ferric chloride solutions have shown that the identity of the ferric chloro species present changes over this concentration range. Although the identities of the ferric chloro species present at a particular concentration are interpreted somewhat differently by each group of workers, they do agree that increasing the ferric chloride concentration changes the principle species in solution.

From the results of the above-mentioned workers and considering equilibrium values^{12,13} for the various ferric chloro species, it appears that three ferric chloro species are involved. In the low concentration range both $\text{FeCl}_2(\text{H}_2\text{O})_4^+$ and $\text{FeCl}_3(\text{H}_2\text{O})_3$ are present, with the former probably in greater concentration than the latter. As the concentration (Baumé) increases, $\text{FeCl}_3(\text{H}_2\text{O})_3$ becomes the predominate species with $\text{FeCl}_2(\text{H}_2\text{O})_4^+$ declining. At the same time FeCl_4^- starts appearing and at high concentrations becomes the predominate species. The appearance of FeCl_4^- is further enhanced by the presence of chlorides.⁹

Immediately apparent is the different charge associated with each of the ferric chloro species. Two of the ferric chloro species are ionic with charges of equal but opposite sign, and the other is nonionic. Also of importance is the presence or absence of the counter ion associated with each reacting species. Taken together, the various chemical species present in solution determine the adsorption characteristics of the electrical double layer between the steel substrate and bulk solution.¹⁴ Changing the charge or eliminating it on the reacting species would be expected to have a profound effect upon the electrical double layer, resulting in a change in the rate of adsorption. If the presence of FeCl_4^- slows the rate of adsorption sufficiently, then a change in reaction mechanism from transport-limited to surface-limited would occur.

A result that supports this theory is the effect of added chloride ions upon etch rate. As shown in Table 3, added chloride ions cause a greater etch rate inhibition as the Baumé is increased. In the Baumé regions where FeCl_4^- formation is favored, adding excess chloride ions would greatly enhance FeCl_4^- formation. Any increase in FeCl_4^- concentration would then cause the observed reduction in etch rate.

Finally, it is of interest to compare our results with those of Allen and co-workers¹⁵ who studied ferric chloride etching of annealed AISI 304 stainless steel. The etch rate versus Baumé (30°–45° Bé at 30° and 50°C) curves they generated were somewhat different than those in Fig. 1. They found that upon decreasing the Baumé, an increase in etch rate occurred until ~38°–42° Bé, where the etch rate leveled off before rising to a maximum at ~33–34° Bé. Our results also show an increase in etch rate as Baumé decreases, but we observed no inflexion point at ~38°–42° Bé. They ascribe this inflection point to a changeover in reaction mechanisms. The changeover is possibly due to the presence of significant alloying elements (19% Cr; 10% Ni) in the AISI 304 stainless steel.

The difference in surface roughness between the two steel types as Baumé and temperature are varied is even more striking. Instead

of the sudden increase in surface roughness observed with 1008 rimmed steel, they observed a smooth increase in surface roughness as Baumé was decreased. Interestingly, they found a greater increase in surface roughness at lower temperatures, whereas we observed this at higher temperatures. Again, this is probably due to differences in the chemical composition of the two steels.*

Both steels exhibit a similar decrease in etch rate as free acid is increased. Although Allen and his coworkers studied this only at 40.2° Bé (30° and 50°C), their results are in agreement with ours in this Baumé region. However, they also observed at this Baumé that the surface roughness could be drastically changed by varying free-acid concentration. In contrast, we found that 1008 rimmed steel shows no dependence of surface roughness upon free-acid concentration around the Baumé where the transition from smooth to rough surface finish occurs.

The point to be made from this comparison is that differences in steel composition due to significant amounts of alloying elements can drastically change the manner in which the material will etch in ferric chloride. Thus, conclusions concerning etch rate and surface finish based upon etching one type of material may not be applicable to a different untried material.

Conclusions

The etching dynamics of 1008 rimmed steel with ferric chloride consists of two competing reaction mechanisms. In the region of low Baumé ($\sim < 40$ Bé) transport-limited kinetics dominate, while at high Baumé ($\sim > 54$ Bé) surface-limited kinetics dominate. Intermediate Baumés are a combination of varying degrees of the two types of reaction kinetics.

Surface finish of etched pieces is dependent upon Baumé and, to a lesser extent, upon temperature. A sudden increase in surface roughness is observed at a specific Baumé and temperature. Increasing the temperature of the etchant increases the Baumé where this is observed. Additionally, increased surface roughness may contribute to general nonuniformity in an etched piece.

High chloride ion concentrations were found to inhibit etch rates, particularly at high Baumés, and have no noticeable effect upon surface roughness.

* Allen et al (Ref. [15]) utilized spray etching. We do not believe this to be a major contributing factor in the differences observed between our study and theirs.

Acknowledgments

The authors wish to thank Dale Goodman for measuring surface roughness and JoAnn Wolfe for the SEM topography photographs.

References:

- ¹ R. B. Maynard, J. J. Moscony, and M. H. Saunders, "A Study of the Etching Kinetics of Low Carbon Steel Using the Ferric Perchlorate-Perchloric Acid System as a Model," *RCA Review*, **45**, p. 58, March 1984.
- ² R. G. Wilkins, *The Study of Kinetics and Mechanisms of Reactions of Transition Metal Complexes*, p. 79-81, Allyn and Bacon, Inc., Boston, MA, 1974.
- ³ V. Fried, H. F. Hameka, and U. Blukis, *Physical Chemistry*, p. 64, McMillan Publishing Co., Inc., New York, 1977.
- ⁴ S. W. Benson, *The Foundation of Chemical Kinetics*, p. 499, McGraw-Hill, New York, 1960; D. Shooter in *Comprehensive Chemical Kinetics*, Vol. 1, p. 253, C. H. Bamford and D. F. H. Tipper, Eds., Elsevier, Amsterdam, 1969.
- ⁵ H. R. Rogers, C. L. Hill, Y. Fujiwara, R. J. Rogers, H. L. Mitchell, and G. M. Whitesides, "Mechanism of Formation of Grignard Reagents. Kinetics of Reaction of Alkyl Halides in Diethyl Ether with Magnesium," *J. Amer. Chem. Soc.*, **102**, p. 217, 1980.
- ⁶ W. Jost, *Diffusion in Solids, Liquids and Gases*, p. 2, Academic Press, Inc., New York, 1952.
- ⁷ W. J. Moore, *Physical Chemistry*, 4th Ed., p. 496, Prentice-Hall, Inc., Englewood Cliffs, NJ, 1972.
- ⁸ V. Fried, H. F. Hameka and U. Blukis, *Physical Chemistry*, p. 710, McMillan Publishing Co., Inc., New York, 1977.
- ⁹ W. L. Marston and S. F. Bush, "Raman Spectral Investigation of the Complex Species of Ferric Chloride in Concentrated Aqueous Solution," *Appl. Spectros.*, **26**, p. 579, 1972.
- ¹⁰ M. Magini and T. Radnai, "X-Ray Diffraction Study of Ferric Chloride Solutions and Hydrated Melt. Analysis of the Iron(III)-Chloride Complexes Formation," *J. Chem. Phys.*, **71**, p. 4255, 1979; G. Giubileo, M. Magini, G. Licheri, G. Paschina, G. Piccaluga, and G. Pinna, "On the Structure of Iron(III) Chloride Solutions," *Inorg. Chem.*, **22**, p. 1001, 1983.
- ¹¹ D. L. Wertz and M. L. Steele, "Coordination of Fe³⁺ in Concentrated Aqueous Solutions with Chloride Ligands," *Inorg. Chem.*, **19**, p. 1652, 1980; D. L. Wertz and M. D. Luter, "Evolving Cation Coordination in Aqueous Solutions Prepared from Iron(III) Chloride Hexahydrate," *Inorg. Chem.*, **20**, p. 3118, 1981.
- ¹² G. A. Gamlen and D. O. Jordan, "A Spectroscopic Study of the Iron(III) Chloro-Complexes," *J. Chem. Soc.*, p. 1453, 1953.
- ¹³ Y. Strahm, R. C. Patel and E. Matijevec, "Thermodynamics and Kinetics of Aqueous Iron(III) Chloride Complex Formation," *J. Phys. Chem.*, **83**, p. 1689, 1979.
- ¹⁴ A. W. Adamson, *Physical Chemistry of Surfaces*, 3rd Ed., p. 411, John Wiley and Sons, New York, 1976; M. J. Rosen, *Surfactants and Interfacial Phenomena*, p. 26, John Wiley and Sons, New York, 1978.
- ¹⁵ D. M. Allen, A. J. Hegarty and D. F. Horne, "Surface Textures of Annealed AISI 304 Stainless Steel Etched by Aqueous Ferric Chloride-Hydrochloric Acid Solutions," *Trans. Inst. Met. Finish*, **59**, p. 25, 1981.

Interaction with Metal Films on Glass: A New Method for Evaluating Solder Parameters*

S. Tosima,† S. Harada,** and E. O. Johnson†

Abstract—The interaction rate between molten solder and a metal film of known thickness and composition deposited on a heat-resistant, transparent glass substrate can be measured conveniently by the length of time required for the underside of the film to start changing color.

The utility of this simple method for observing and analyzing solder behavior was demonstrated for various solder impurities, temperature and motion effects, and alloy compositions. The new method is quicker and more convenient than the usual chemical method for measuring the amount of a solder impurity, such as copper, the most probable contaminant from the usual factory circuit board soldering operation. The method directly reveals when the solder is saturated with an impurity.

Operation of the new method is explicable in terms of a simple diffusion model. At impurity levels below solder saturation, the method operates by measuring the dissolution rate of the metal film into the solder. At levels above saturation, the method reveals the diffusion rate of Sn from the solder into the metal film.

1. Introduction

The practical behavior of the lead-tin solder alloy system is affected by various parameters including impurities, particularly copper,

* A major part of this work was done during 1981–1982 under RCA sponsorship. RCA approval has been given to summarize and publish as herein described.

** S. Harada is now with Tokyo Laboratories, Sharp Co., Kashiwa City, Chiba, 277 Japan.

† Presently with Corning Research, Inc., Machida City, Tokyo, 194-02 Japan.

nickel, and zinc. A simple means of evaluating such behavior is of practical and scientific interest.

Ackroyd et al.¹ used area-of-spread, rotary dip, and surface-tension balance methods to study the effects of certain impurities in solder. Latin² studied the dynamics of capillary flow involving area-of-spread, surface tension, wetting time, and the penetration coefficient. One of the present authors and Y. Wada studied solderability using the capillary rise method and found that a static parameter, such as adhesion tension, is not a sensitive parameter for evaluating impurity effects on solderability.³

The new technique described in this paper is a sensitive and direct means for measuring impurity levels and other effects. A thin metal sample film of known thickness is deposited on one side of a thin, transparent piece of glass. The dissolution and alloy interaction of this in molten solder alloy can be measured by the length of time required for the underside of the film to start changing color. Such observations conveniently reveal the effects of impurities, surface layers, flux, and other parameters on the solder alloy system. Results seem concordant with simple physics.

This paper describes the physical principles, the experimental procedure, and typical results. For reasons of practicality and convenience, major emphasis is on the behavior of copper in the tin/lead, near-eutectic 60/40 system.

2. Physical Principles

When a copper film on glass contacts molten Sn/Pb solder, Sn atoms diffuse into the Cu film, and Cu atoms from the film diffuse into the solder. This process involves the phase system:^{4,5,6} Sn/Pb solder/ Cu_6Sn_5 (η -phase)// Cu_3Sn (ϵ -phase)//Cu//glass.

With time, the Cu film is gradually consumed and the other phases appear in succession at the glass surface where they can be seen by their increasingly silvery appearance. Finally, all of the intermediate phases disappear and the solder itself appears at the glass surface. This expected phase behavior was conveniently confirmed by ultrasonically peeling the composite film from our glass samples at various stages of the process and x-ray analyzing it.

There are two cases to consider with respect to the rate of change of the above phase system. In the first case, the system rate of change is determined by the rate of dissolution and diffusion of the film metal into the solder. This situation prevails when the solder is not saturated with film metal. In the second case, system change

rate is limited by Sn diffusion from the solder into the film metal. This case prevails when the solder is saturated with film metal.

The first case should be explicable in terms of the simple diffusion relation:

$$\frac{dh}{dt} \propto D (C_{sat} - C)/\delta \quad [1]$$

where h (μm) is the metal film thickness; t (sec) is time; D is the diffusion constant of the film metal in the solder; C_{sat} (wt%) is the saturation concentration of the film metal in the solder; C (wt%) is the actual film metal concentration; and δ is the thickness of a narrow boundary zone at the liquid/solid surface. The solder at the film surface side of the zone has a saturation concentration C_{sat} of film metal; the opposite side of the zone has a concentration C equal to that in the body of the liquid solder. The boundary zone should have a width inversely proportional to the square root of the speed U (cm/sec) of solder that flows parallel to the film surface due to convection or stirring. Eq. [1] can then be written

$$\frac{h}{t} = A\sqrt{U} (C_{sat} - C), \quad [2]$$

where A is a constant. We have assumed that the total amount of film metal to be dissolved into the solder during an experiment is small compared to the amount already there. A thickness h of film is consumed during a time t .

In the second case, where there is no concentration difference term in Eqs. [1] and [2], the diffusion of Sn into the metal film is described by the diffusion equation

$$\frac{\partial C_f}{\partial t} = D \frac{\partial^2 C_f}{\partial x^2} \quad [3]$$

where C_f is the concentration of Sn in the film, t is time, D is the Sn diffusion constant, and x is the distance from the outer surface of the film measured normal to the film plane. Eq. [3] can be normalized by the dimensionless factors τ and ϵ in the relations

$$\tau = \frac{t}{t_0} \text{ and } \epsilon = \frac{x}{h}, \quad [4]$$

where t_0 is the time required for the Sn concentration to reach a concentration C_0 at the glass interface where Sn presence can be visually detected, and h is the film thickness. Eq. [3] becomes

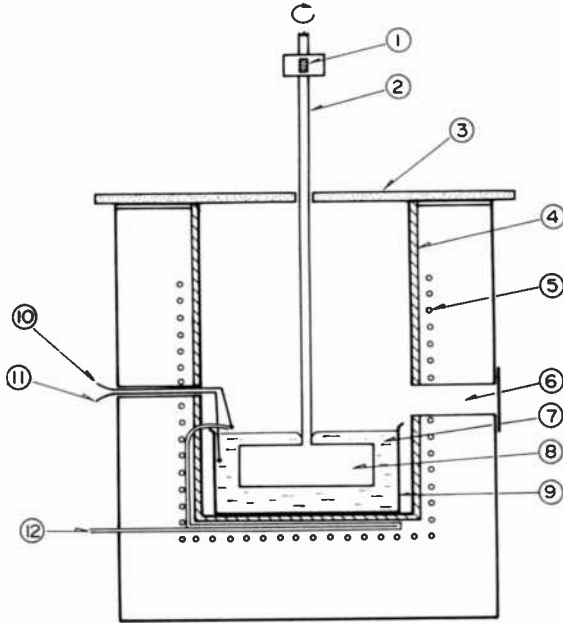


Fig. 1—Experimental apparatus. 1. Reflector for rotation counting; 2. stirrer shaft; 3. plate of fused silica; 4. stainless steel shell; 5. heating element; 6. sample inlet with cover; 7. molten solder; 8. stirrer blade; 9. stainless steel solder bath; 10, 11. thermocouple; 12. copper nitrogen pipe.

$$\frac{\partial C}{\partial \tau} = a \frac{\partial^2 C}{\partial \epsilon^2} \quad [5]$$

with

$$a = Dt_0/h^2. \quad [6]$$

If the parameter a is held constant, the solution to Eq. [5] should be the same regardless of film thickness h . For our purposes, this means that the time t_0 for a color change to be observed at the back surface of the film is proportional to the square of h .

3. Experimental Arrangement

Test samples were prepared by vacuum evaporation (4×10^{-7} Torr) of copper from a tungsten boat onto carefully cleaned borosilicate glass substrates $8 \times 6 \times 0.2$ mm³. The 0.2-mm thickness was chosen as a compromise between mechanical robustness and thermal mass. The deposition rate of 4N copper was $0.2 \mu\text{m}/\text{min}$ as determined from weight measurements and a quartz-crystal mon-

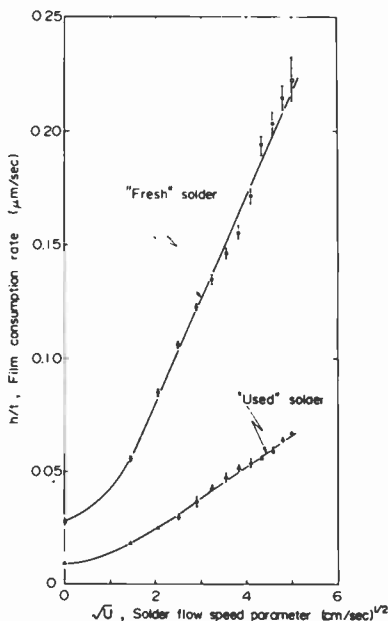


Fig. 2—Effect of solder flow speed on Cu film consumption rate for fresh and used (copper-contaminated) solder. Film thickness 4 μm ; solder temperature 260°C.

itor. X-ray analysis showed our films to be $\langle 111 \rangle$ axis-oriented perpendicular to the substrate surface. For 2- μm -thick films at RT, the measured resistivity was 1.8 to 2.0 $\mu\Omega\text{-cm}$; the handbook value for bulk copper is listed as 1.7 $\mu\Omega\text{-cm}$.

The test apparatus shown in Fig. 1 consists of a small mantle heater furnace (400 W) for solder bath heating and a stirrer to generate flow motion of the molten solder. A small inlet hole (1 \times 2 cm^2) with a cover on the furnace sidewall was used for sample insertion. Nitrogen was introduced through a heated pipe to suppress oxidation of the solder surface. The container for the molten solder was a stainless steel vessel 2 cm in height and 6 cm in diameter. The molten solder temperature was kept with $\pm 1^\circ\text{C}$ at the typical soldering temperature of 260°C. This temperature was used unless otherwise noted.

The starting solder compositions were all 60Sn/40Pb unless otherwise noted. To prepare solder samples contaminated with Cu-impurity, a known amount of Cu was dissolved into the fresh solder sample at 300°C.

The molten solder of 425-g mass was stirred to maintain a uniform Cu concentration and also as a means to verify Eq. [2]. The stirrer blade is located in the middle of the solder pool and rotates

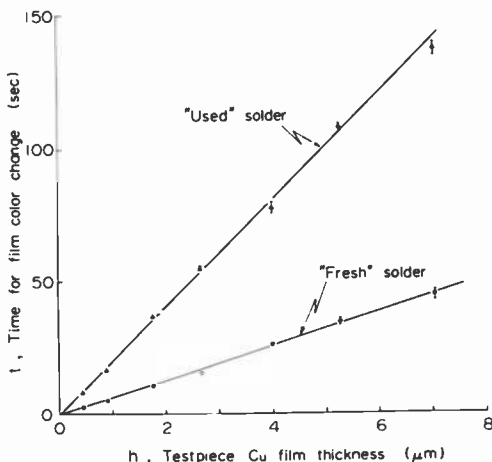


Fig. 3—Effect of Cu film thickness on time required for film backside color change. Solder temperature 260°C; solder flow speed 14.7 cm/sec.

around the vertical axis of the solder container. It is a thin stainless steel plate 3.8 cm long, 1.0 cm wide, and 0.5 mm thick. The flow speed of the molten solder at the sample location was estimated from the rotational speed of the stirrer and the distance of the sample from the stirrer shaft. Speed was kept below 120 rpm to prevent solder turbulence.

4. Sample Behavior

The test piece of Cu film on glass was held over the molten solder for about 5 seconds for preheating before film contact was made with the solder. The piece was allowed to float on the solder surface with the film side down. To remove intervening oxides, a rosin flux was used (Y-20, Tamura Kaken Co., Ltd.).

When this is done on a motionless molten solder pool, the Cu film color change typically starts at the periphery of the film and proceeds toward the center. On the other hand, when the molten solder is flowing, color change starts at the upstream edge of the film and proceeds along in the solder flow direction towards the downstream edge. Because of such effects, the experimentally measured reaction times were taken as those required to complete the color change over the entire sample.

Lateral motion of the color change front does not signify diffusion laterally along the Cu-glass interface from edges, pinholes, or other seemingly preferential paths. This was tested with two samples. In

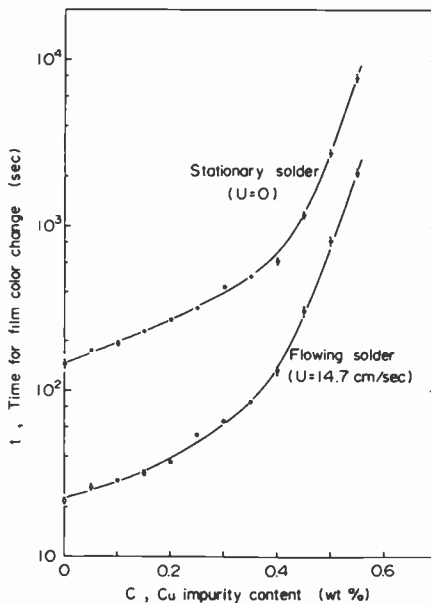


Fig. 4—Effect of solder Cu impurity on time for film backside color change for stationary and flowing solder. Film thickness $4\ \mu\text{m}$; solder temperature 260°C .

one, the Cu film was scratched through to the glass surface with a sharp needle; color front motional behavior was unaffected. In the other sample, the Cu film was deposited thickly along the periphery and thinly in the central area. The color change viewed from the rear side of the glass occurred first in the central area. From such observations we infer that dissolution and diffusion occurs in a planar manner from the solder side of the film toward the Cu-glass interface.

To evaluate the effect of the oxide layer on the Cu film surface, one-half of the surface of a freshly prepared film was prefluxed to avoid oxidation. The other half of the film surface was left bare. After 3 weeks the sample was treated with the Y-20 flux and immersed in molten solder. The time was observed for backside color change of the film. No difference was detected for the two differently treated surface regions. The Y-20 flux was accordingly judged adequate to remove oxide layers on the film.

5. Experimental Results at 260°C with Cu Films

The results were obtained with Cu film thicknesses of $4\ \mu\text{m}$ unless otherwise specified.

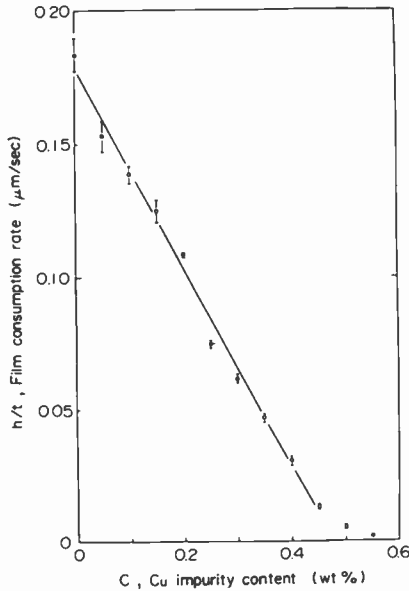


Fig. 5—Effect of solder Cu impurity on Cu film consumption rate. Data taken from flowing solder curve in Fig. 4.

In Fig. 2 the film consumption rate h/t for “fresh” and factory “used” solder is seen to be proportional to the square root of the solder flow speed U except at small values where convection effects dominate. Convection was not easy to control and the results at $U < 2$ cm/sec were not used in the analyses.

Fig. 3 shows that time t is proportional to Cu film thickness h in both fresh and “used” solder samples. The rate h/t is thus independent of film thickness.

Fig. 4 shows the t dependence of Cu impurity content C in the solder. For the “used” solder sample, a time of 77 sec was required for color change when $U = 14.7$ cm/sec, and 450 sec for $U = 0$. These t values correspond to a 0.33 wt% of C in Fig. 4. This value is very close to the factory specification for the allowable upper limit of 0.3 wt% in a solder bath.¹

The data for the $U = 14.7$ cm/sec case in Fig. 4 was used to plot the h/t versus C curve shown in Fig. 5. The relationship is linear except for the tail region where $C > 0.4$ wt%.

The above experimental data applied to Eq. [2] by a least square fit gives $A = 9.7 \times 10^{-2}$ and $C_{sat} = 0.476$ wt% for $U > 2$ cm/sec and $C < 0.4$ wt%. Similar results were observed by Shoji et al. in the dissolution of solid copper in molten tin.⁷ Experimental data for the color change time t appearing in Figs. 2, 3, and 4 are summa-

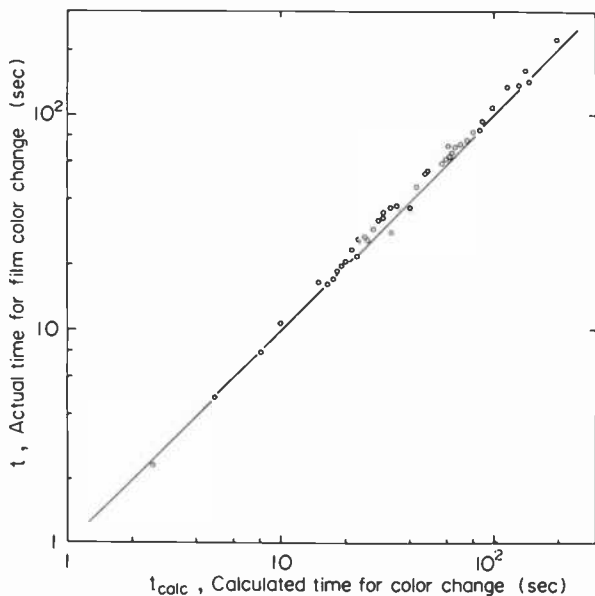


Fig. 6—Comparison of actual and calculated times required for Cu film backside color change. Least square-fitted data from Figs. 2, 3, and 4 used in Eq. [2] for calculated times.

rized and plotted against t_{calc} in Fig. 6. The good correlation indicates that film consumption is caused by Cu diffusion from the film into the molten solder across a thin boundary zone (~ 0.1 mm) that occurs under our test conditions where the Reynolds number, in our case, is typically about 2000.

6. Effect of Solder Temperature

This was studied over the 215–290°C range with Cu concentrations of 0–0.9 wt%, and primarily with a Cu film thickness of 0.74 μm . Results with stationary and flowing solder ($U = 14.7$ cm/sec) are summarized in Figs. 7 and 8, respectively. In both cases there is a similar tendency for the curves to saturate at high Cu concentrations, the saturation occurring at higher concentrations for higher temperatures. Also, in both figures it can be seen that regions where time t is insensitive to Cu content, t is also insensitive to solder motion. This suggests that the solder is saturated with Cu impurity and that Sn diffusion into the Cu film becomes the dominant mechanism for causing the backside of the film to change color.

Fig. 9 shows the effect of solder Cu impurity on the inverse film consumption rate t/h at 260°C and $U = 14.7$ cm/sec for two film

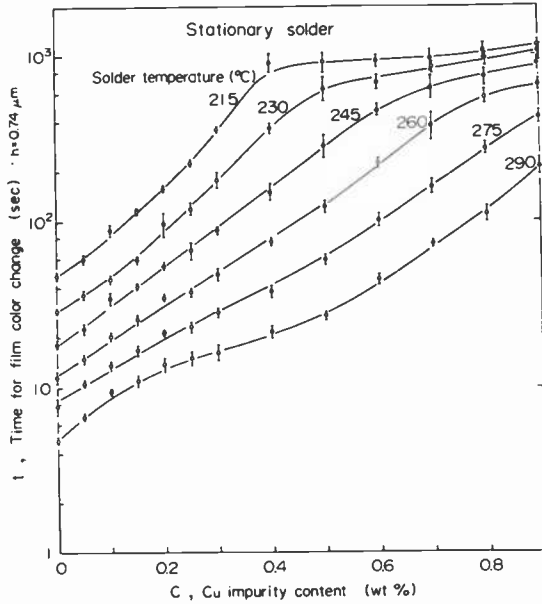


Fig. 7—Effect of solder temperature and Cu impurity content on color change time. Solder flow speed $U = 0$; Cu film thickness $0.74 \mu\text{m}$.

thicknesses, $h = 4.0$ and $0.74 \mu\text{m}$. At low solder impurity levels where $\text{Cu} < 0.4 \text{ wt}\%$, the film dissolution rate is independent of film thickness in accordance with the physical mechanism described by Equ. [2]. On the other hand, at higher impurity levels the marked dependence on film thickness shows the predominance of another physical mechanism. This other mechanism, besides being dependent upon film thickness, substantially increases the time required for the backside of the Cu film to change color. This behavior is qualitatively in accord with Eq. [6]. Quantitative behavior was not studied.

Dependence of the film consumption rate h/t upon the solder impurity content is plotted in Fig. 10 at various temperatures. From the linear portions of the curves, the least squares fit values of C_{sat} and A of Eq. [2] were obtained with the results shown in Fig. 11. In Fig. 10 the extrapolation of the linear regions of the curves to the $h/t = 0$ axis gives values for the saturation concentration of Cu in the solder.

7. Effect of Other Solder Impurities on Cu Film Behavior

While Cu is the most probable contaminant of solder in circuit board manufacture, it is not the only one.⁸ Some of the other possible

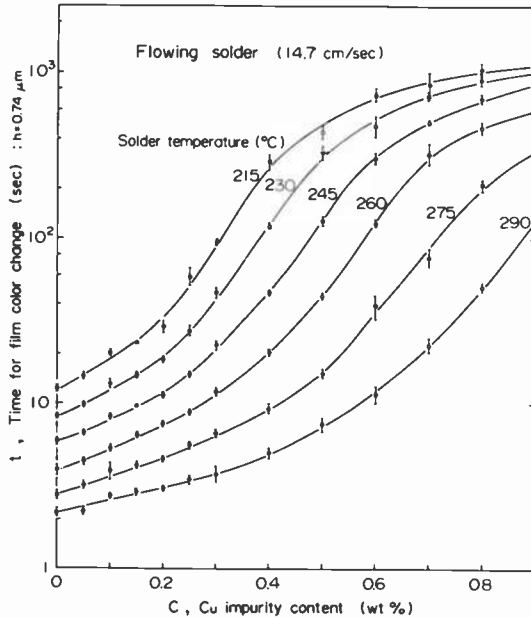


Fig. 8—Effect of solder temperature and Cu impurity content on color change time. Solder flow speed $U = 14.7$ cm/sec; Cu film thickness $0.74 \mu\text{m}$.

contaminants were studied at 260°C in the manner previously described for Cu used as the sole impurity. Chemical analysis of solder impurity elements can be a laborious process⁸ and another more convenient supplementary method is of practical interest.

Nine elements from a typical factory impurity specification list, excluding Cu, were separately used to contaminate solder up to a few wt% with a known quantity of each impurity. The observed order of solubility of these elements in 60/40 molten tin/lead solder was: In, Au \gg Bi, Cd \gg Sb $>$ Ag, Zn \gg As, Ni. Ag, Bi, Sb, Cd, In, Au, and As had no effect on the color change time t of the backside of a Cu film. Ni and Zn significantly increase t and thus should be treated with caution in the soldering process.

The effect of Zn and Ni impurity wt% is shown in Fig. 12 for $U = 0$ and $U = 14.7$ cm/sec. The Ni effect saturates at a low wt% because of the limited solubility of Ni in the solder.

The Zn effect on Cu film consumption rate h/t is shown in Fig. 13. Note that there is no characteristic linear region such as shown in Fig. 5 with Cu impurity.

The above described effects can be largely understood in terms of the phase diagrams of binary systems⁹ and knowledge of the ther-

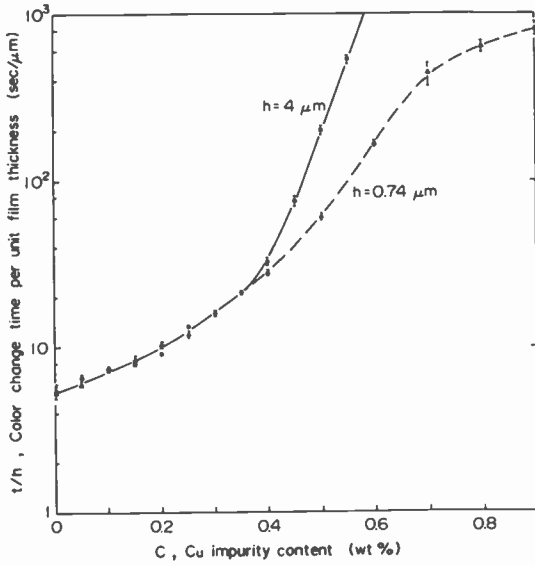


Fig. 9—Effect of solder Cu impurity content on Cu film inverse consumption rate for film thickness $h = 0.74$ and $4.0 \mu\text{m}$. Temperature 260°C and solder flow speed $U = \text{cm}/\text{sec}$.

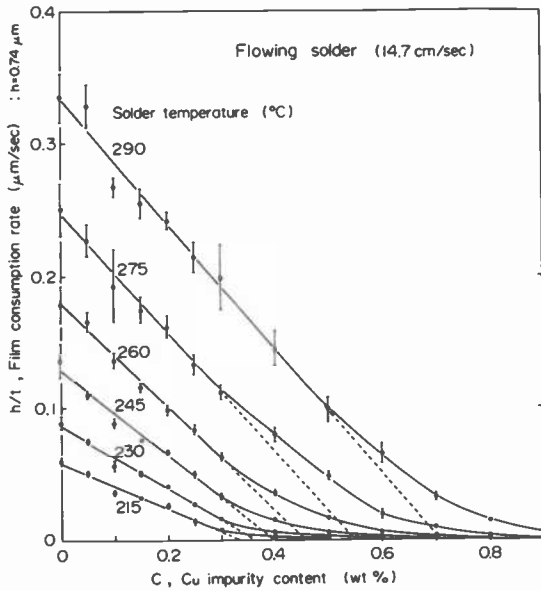


Fig. 10—Effect of solder Cu impurity on Cu film consumption rate at various temperatures. Film thickness $h = 0.74 \mu\text{m}$.

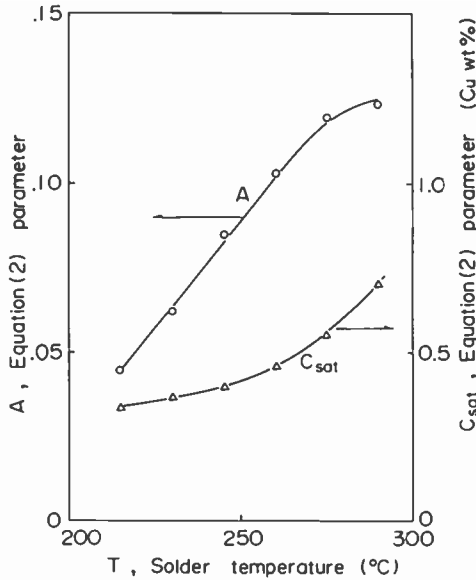


Fig. 11—Least squares fitted values for Eq. [2] constants A and C_{sat} as a function of temperature. Data from linear regions of curves in Fig. 10.

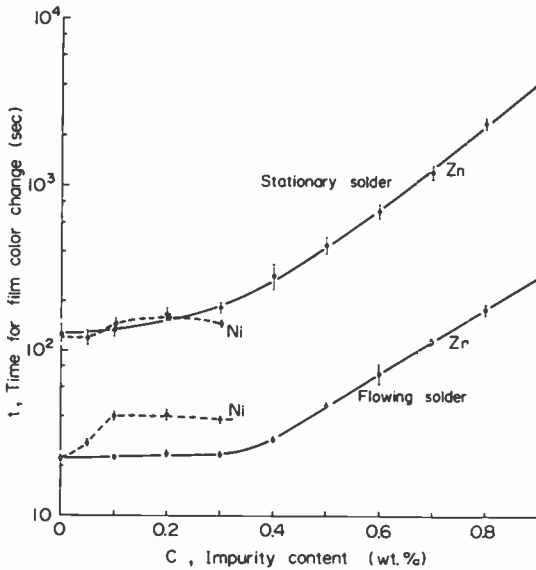


Fig. 12—Effect of solder Ni and Zn impurity on Cu film color change time for stationary and flowing solder $U = 14.7$ cm/sec. Solder temperature 260°C and Cu film thickness 4.0 μm .

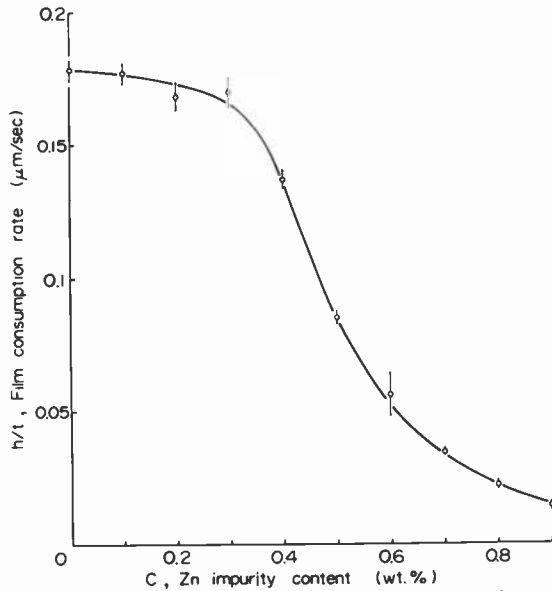


Fig. 13—Effect of solder Zn impurity on Cu film consumption rate. Solder flow speed $U = 14.7$ cm/sec, solder temperature 260°C , and Cu film thickness 4.0 μm .

modynamic potential¹⁰ of the intermetallic compounds in such systems. Among the factors to be considered are: impurity solubility in the solder and Cu; the possibility of formation of intermetallic compounds with Cu, Sn, and Pb; and the relative coupling of impurity atoms to Pb, Sn, and Cu. With respect to the latter factor, for example, Au and Zn are quite different; Au forms intermetallic compounds with Sn and Pb, but Zn does not. On the other hand, Zn is highly reactive with Cu.

In addition to the effect on Cu film behavior, Zn causes other generally undesirable effects. When Zn content exceeds about 0.1 wt%, a silvery white tenacious surface layer remains stuck to the Cu film. Such behavior will have harmful effects in bridging and icicle formation on circuit boards.

8. Other Film and Impurity Combinations: Double-Layer Films

The previously described techniques can be used to study the effect in soldering of other material combinations of electronic industry interest, for example, the effect of gold impurities in solder on gold films. As with copper, gold is easily distinguishable in color from

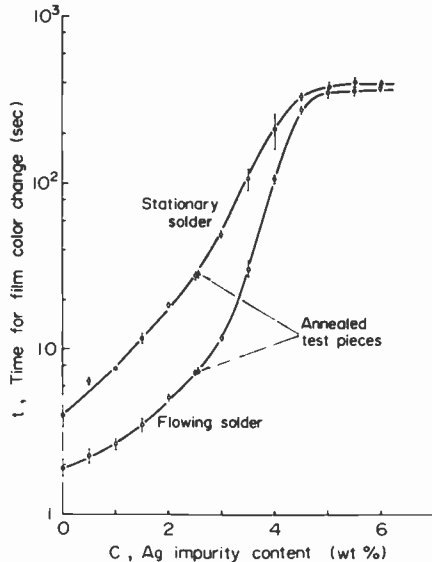


Fig. 14—Effect of solder Ag impurity on unannealed and annealed Ag film backside color change time for stationary, and for flowing solder $U = 14.7$ cm/sec. Solder temperature 260°C , Ag film thickness $3\ \mu\text{m}$.

solder, and gold film color changes can be observed readily on the backside of the film. However, such color change is not readily visible with a film such as Ag, whose color is similar to that of solder. This problem is easily solved by using a double-layer film. The material of the outer layer that contacts the molten solder is chosen to be the same as the solder impurity element to be studied. The inner layer is composed of a visible, but very thin, layer of Au or Cu that rapidly changes color when contacted by hot solder or a silvery impurity element.

Experimental results are demonstrated in Fig. 14 for a $3\text{-}\mu\text{m}$ -thick Ag film deposited over an Au layer. The solder impurity was Ag, and measurements were carried out at 260°C with 60Sn/40Pb solder both stationary and moving ($U = 14.7$ cm/sec). The curves are similar to those of the Cu film/Cu impurity system and saturate abruptly at about 5 wt% of the Ag impurity. As with the Cu system, curve saturation independent of solder flow velocity, signifies saturation concentration of Ag in the solder at 260°C .

Since alloy formation and dissolution may depend upon film quality,¹¹ the Ag films were annealed at 260°C in Ar in 10^{-2} to 10^{-3} Torr pressure. As indicated in Fig. 14, no difference was observed between these films and the unannealed ones.

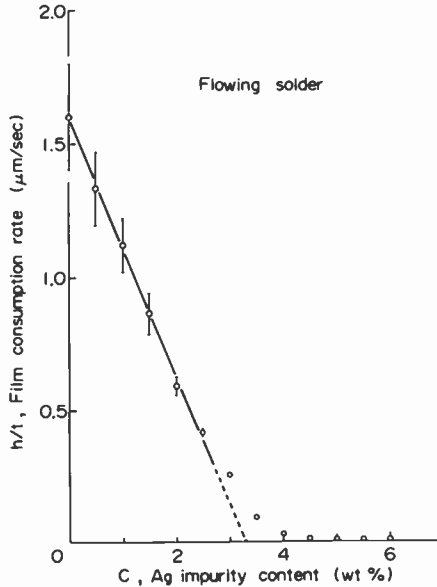


Fig. 15—Effect of flowing solder Ag impurity on Ag film consumption rate. Solder temperature 260°C, solder flow speed 14.7 cm/sec, Ag film thickness 3 μm.

Least square derived values for A and C_{sat} for impurity contents up to 2.5 wt% are 12.5×10^{-2} and 3.3 wt%, respectively. The value of A is close to the value 9.7×10^{-2} observed for the Cu system. Similar to the Cu case, the Ag saturation concentration determined from the h/t versus C plot in Fig. 15 in the low C region was somewhat lower than that determined from the slope transition in Fig. 14.

9. Effect of Solder Tin/Lead Composition

This was studied at 260°C using the Cu film color change time t as a measure of the effect of various values of Sn content (54 to 100 wt%) and Cu impurity content C . Observed compositional dependence is attributed to the increase of the solubility of Cu in solder with increasing Sn content; molten tin can dissolve impurity elements, such as Cu, more readily than can Pb.⁹ This is of practical interest because tin is more rapidly consumed by oxidation in the usual soldering process than is lead.¹² Meanwhile, in usual practice the solder-dissolved impurity content, mainly Cu, gradually increases due to dissolution from circuit board metal parts. These

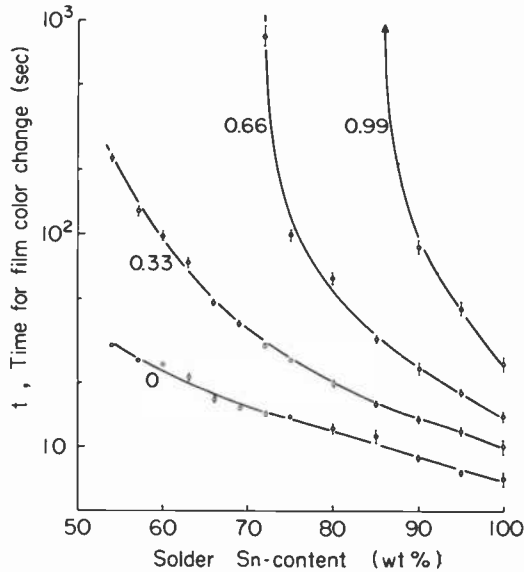


Fig. 16—Effect of solder Sn content on Cu film backside color change time for different solder Cu impurity contents. Solder flow speed 14.7 cm/sec, solder temperature 260°C, and copper film thickness 4.0 μm . Numbers attached to the curves represent the Cu impurity contents in wt%.

combined effects can cause large changes in the interaction of the solder with Cu parts on a circuit board.

Such effects can be seen in Fig. 16 where solder tin content is plotted against the time for film backside color change with Cu flowing solder ($U = 14.7$ cm/sec) impurity content (wt%) as a parameter. Qualitatively similar behavior is shown by stationary solder.

The data in Fig. 16 were analyzed with Eq. [2] to find the C_{sat} dependence of Cu upon solder composition. This is conveniently done since the parameter A in Eq. [2] is independent of Cu content. The least squares result is shown in Fig. 17. At 100 wt% of Sn, the value of C_{sat} reaches 1.37 ± 0.12 wt%, a value slightly lower than 1.5 wt% (2.7 at%) reported by Heycock and Neville.¹³ The values of A in Fig. 17 were obtained from the least square values of C_{sat} and Eq. [2]. The parameter A is only weakly dependent upon the Sn content.

The solid curves in Fig. 18 were obtained from Eq. [2] using the above determined values of A and C_{sat} . Experimental data are included for comparison. Reasonable agreement shows the utility of Eq. [2].

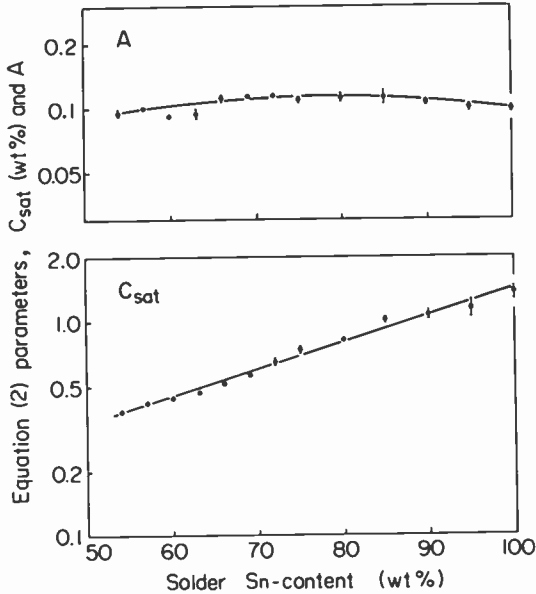


Fig. 17—Effect of solder Sn content on parameters A and C_{sat} in Eq. [2]. Least square data taken from Fig. 16.

10. Conclusions

The utility of a simple film-on-glass method for observing and analyzing solder behavior was demonstrated for various solder impurities, temperatures, motion effects, and alloy compositions. The method conveniently measures solder impurity content, for example that of Cu, Ag, Ni, and Zn. Saturation levels are readily determined.

At impurity levels below saturation, the method operates by measuring the dissolution rate of the metal film into the solder. At impurity levels above solder saturation, the method reveals the diffusion rate of Sn from the solder into the metal film. Behavior is concordant with simple diffusion models.

Acknowledgments

The authors appreciate helpful discussions and advice from Drs. F. Okamoto and Y. Wada. Permission to publish this paper by the RCA Laboratories, Princeton, New Jersey, and their many helpful suggestions are much appreciated.

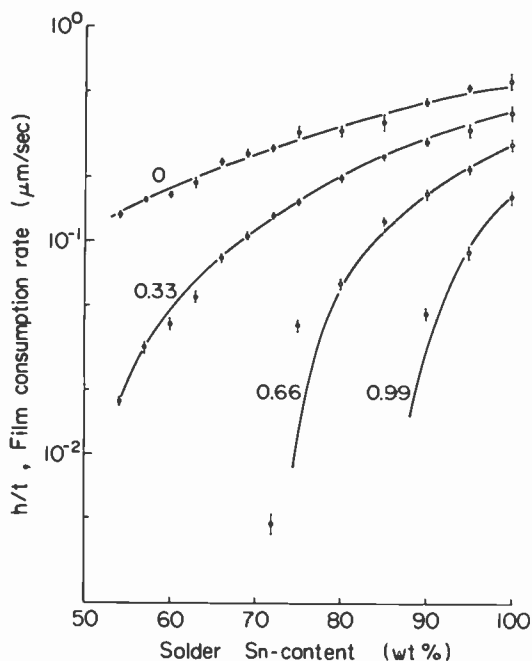


Fig. 18—Effect of solder Sn content upon Cu film consumption rate: comparison of calculated results (solid curves) with observed data (data points). Calculated results were obtained from Eq. [2] using the A and C_{sar} values of Fig. 17. Numbers attached to the curves represent the Cu impurity contents in wt%.

References:

- ¹ M. L. Ackroyd, C. A. Mackay, and C. J. Thwaites, *Metals Tech.*, **2**, p. 73, 1975.
- ² A. Latin, *J. Inst. Metals*, **72**, p. 265, 1946.
- ³ S. Harada and Y. Wada, private communication.
- ⁴ E. Toledo, S. Bonis, J. Breen, and F. Oberin, *Circuits Manufacturing*, p. 64, Jan. 1970.
- ⁵ K. Kumar and A. Moscaritolo, *J. Electrochem. Soc.*, **128**, p. 379, 1981.
- ⁶ K. Kumar, A. Moscaritolo, and M. Brownawell, *J. Electrochem. Soc.*, **128**, p. 2165, 1981.
- ⁷ Y. Shoji, S. Uchida, and T. Ariga, *Trans. Japan Weld. Soc.*, **11**, p. 143, 1980; *ibid.*, **11**, p. 148, 1980; *Weld. Journal*, **60**, p. 195, 1981.
- ⁸ R. Guerra, *Atomic Spectroscopy*, **1**, p. 58, 1980.
- ⁹ M. Hansen, *Constitution of Binary Alloys*, McGraw-Hill, 1958.
- ¹⁰ O. Kubaschewski, E. L. Evans, and C. B. Alcock, *Metallurgical Thermochemistry*, Pergamon Press, Fourth Edition, pp. 304–363, 1967.
- ¹¹ L. J. Rickabaugh, *Electrocomponent Sci. and Tech.*, **4**, p. 43, 1977.
- ¹² A. M. Stoweman, C. A. Mackay, C. J. Thwaites, and J. Mackowiak, *Metals Tech.*, **5**, p. 126, 1978.
- ¹³ C. T. Heycock and F. H. Neville, *Phil. Trans. Roy. Soc. (London)*, **A189**, pp. 47–51 and 62–66, 1897.

Extending the Content and Expanding the Usefulness of the Simple Gaussian Lens Equations—Part 3, Section A: (a) Special Cases of Primitive Two-Lens Relay Optical Systems; (b) Regular and Inverse Relaying Actions of Any Non-Afocal Optical System; (c) Permissible Sign Groupings That Typify Non-Afocal Relaying Actions Generally

L. T. Sachtleben

RCA Advanced Technology Laboratories, Camden, NJ

Abstract—The Gaussian expressions for the optical separation of the two lenses of a non-afocal primitive relay optical system are developed in general forms that are suited to any one of the four conjugate distances being assigned an infinite value. These are extended to the case where the members of one of the conjugate pairs are both infinite, and the system afocal. The afocal system is analyzed to obtain relationships that simplify Gaussian design of an afocal telescope when *all four* conjugate distances are finite. Examples are worked through to illustrate applications. The relaying action of *any* non-afocal optical system (for two discrete object distances) is studied in its most general terms, with the four conjugate distances, the focal length, and the two magnifications being represented as literal parameters with fixed signs. Eight optically possible sign groupings of the parameters are identified when conjugate distances are Newtonian. They are used to identify the eighteen optically possible sign groupings when the conjugate distances are Gaussian. The two sorts of groupings are tabulated for easy reference and to simplify their intercomparison. Analyses that

relate the Newtonian and Gaussian groupings are performed in terms of inequalities. Examples of possible applications are reviewed. Useful applications of the theory of two separated lenses to the problems of a single thick lens are developed. Examples are worked through.

24. Introductory Notes*

All numbering in this paper is a continuation of the numbering in Parts 1 and 2, as described in Secs. 13 (footnote) and 14 of the latter. Equation numbering in Part 3 will begin with Eq. [205].

It is important that the reader review Sec. 18 of Part 2 to understand the dropping of the numerical subscripts that were used in Part 1. Also, when the numerical subscripts are *not* used, it must be observed that if x is plain (x), the corresponding y is *always* plain (y) and vice versa; if x is primed (x'), the corresponding y is always primed (y') and vice versa. A careful re-reading of Secs. 16 through 18 of Part 2 will be very helpful in understanding this paper.

It should be understood that in Eqs. [159] and [160] of Part 2, primes may be added to or dropped from x , M , and D without any effect on f , f' , and F , providing that a , S , and S' remain unchanged (see note that follows Eq. [162]). Any application of this procedure to other equations should be made only after great care has been taken to make certain that it is justified; otherwise, serious error may result.

As a final note, it will usually (but not always) be true that when an equation is called up that has a higher Eq. [No.] than those in the associated portion of the text, that higher numbered equation, along with its derivation, will be found in one of the appendices of Part 3.

25. The Primitive Non-Afocal Relay Optical System In Air or Vacuum, With One of Its Objects, or One of Its Images, at Infinity (See Fig. 12)

The discussion of the problem of the primitive relay optical system in Part 2 (Sec. 17)** tended to be equivocal on the question of an

* Editors Note: This paper is a continuation of the author's previous papers in the December 1976 and June 1978 issues of the *RCA Review*.

** Since we are once again dealing with the primitive relay, which is a special case, lower case x , x' , y , and y' are used. All x and x' are measured from H of lens L , and all y and y' from H' of lens L' , as in Fig. 12. Numerical subscripts also are used in the figure (see Sec. 18, Part 2).

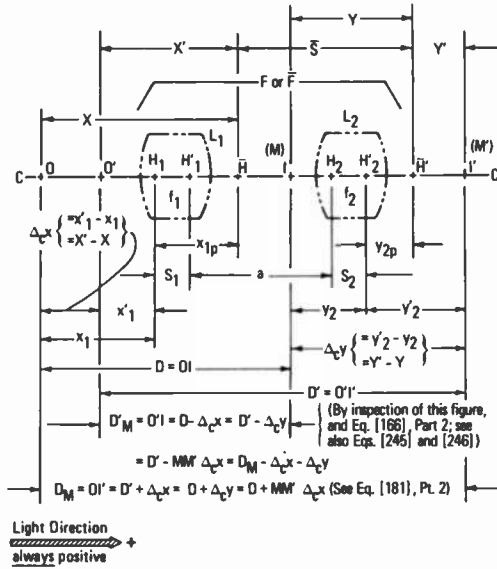


Fig. 12—Quantities that are involved in the Gaussian design relationships for the primitive relay optical system. Similar to Fig. 10, Part 2. Schematic only—not to scale.

object-point or image-point at infinity. A further investigation of the matter shows the development of Eq. [180] in Appendix 3 (Part 2) to be sufficiently general to include the case of either an infinite object-distance or an infinite image-distance. By way of introduction of the topic of this section, there are four broadly defined limiting cases for systems of positive focal length. Each case is defined by a set of three concurrently limited variables, as shown in Table 11. Changes that occur in the table when the system focal length is negative are indicated in the third following paragraph.

The signs that precede the infinite limits and the zero limits in the concurrently limited sets of Table 11 are the signs of *all* of the finite values that the three variables are assumed to pass through monotonically as they approach those limits. For example, Case 1 (with lower signs) is the limiting case as x approaches ∞ through negative values, corresponding to which displacement $\Delta_c x (= x' -$

The present Part 3 depends for its basic understanding, as did Parts 1 and 2, on the Gardner sign convention described in Secs. 3 and 4 of Part 1 (*RCA Review*, 37, p. 439–42, 1976), and elaborated at various points throughout the paper. Equations that are based on the Gardner convention are *not* in conflict with the Conrady sign convention.

x , with x' finite) approaches ∞ through positive values, and M approaches zero through negative values.

The signs of the limiting values of the displacements $\Delta_c x$ and $\Delta_c y$ in Table 11 are easily verified for each case from the parenthetically included equations. These express $\Delta_c x$ and $\Delta_c y$ in terms of both the indicated finite variable and the variable that approaches $\pm\infty$. Verification is done most easily by setting the indicated finite addend equal to zero and expressing the displacement as a limit. In Case 4, for example,

$$\lim_{y' \rightarrow \pm\infty} \Delta_c y = \lim_{y \rightarrow \pm\infty} (y' - y) = \lim_{y \rightarrow \pm\infty} -y = \mp\infty$$

The limits of the displacements are always independent of focal length f and therefore of its sign. The signs of the limiting values of M and M' are verified by assuming $f > 0$ in Eqs. [368] and [369] of Appendix 7, and letting the applicable X , Y , X' , or Y' approach $\pm\infty$. This is permissible because the principal points of a non-afocal primitive relay are at finite distances from the system (see Sec. 9, and Eqs. [32], [33], and [46], Part 1). Thus, for example, when $x \rightarrow \pm\infty$, X also $\rightarrow \pm\infty$, and Eqs. [368] and [369] apply in the limit; similar consideration holds for x' , y , and y' .^{*} In Case 2, for example,

$$\lim_{y' \rightarrow \pm\infty} M' = \lim_{Y' \rightarrow \pm\infty} \frac{f - Y'}{f} = \mp\infty \quad (+\infty \neq f > 0)$$

Eqs. [368] and [369] show clearly that if $f < 0$, the double signs of M and M' in Table 11 would all be inverted. The double signs of displacements $\Delta_c x$ and $\Delta_c y$ would remain unchanged by reversal of the sign of f (see the preceding paragraph).

It must now be pointed out that the double signs in Table 11 and the discussion that follows it merely assist the orientation of the reader to the problem. The signs will be seen to play no mathematical part in deriving the equations that pertain to an infinitely distant object- or image-point for the primitive relay optical system, but they are convenient for reference in cases where the sign of M or M' and of $\Delta_c x$ or $\Delta_c y$ neighboring the applicable limits of Table 11 may be in question. Note again that the double signs of M and M' in Table 11 *must* be inverted if the focal length is negative.

The cases of a single infinite object- or image-distance will be approached through the equations of Appendix 3, Part 2, by appro-

^{*}See Fig. 12 and footnote on p. 110. Note that measurements of X and X' are made from H ; those of Y and Y' from H' . H and H' are the principal points of the non-afocal primitive relay system.

Table 11—Concurrently limited sets of three variables for each of the four cases of the primitive two-lens relay of positive focal length when one object-point, or one image-point, goes to infinity (see Eqs. [172] and [173] of Part 2)

	Concurrent Limits of Variables		Value of Variable Δ_x or Δ_y
Case 1:	$x \rightarrow \pm \infty,$	$\Delta_x \rightarrow \mp \infty,$	$M \rightarrow \pm 0,$
Case 2:	$y' \rightarrow \pm \infty,$	$\Delta_y \rightarrow \pm \infty,$	$M' \rightarrow \mp \infty,$
Case 3:	$x' \rightarrow \pm \infty,$	$\Delta_x \rightarrow \pm \infty,$	$M' \rightarrow \pm 0,$
Case 4:	$y \rightarrow \pm \infty,$	$\Delta_y \rightarrow \mp \infty,$	$M \rightarrow \mp \infty,$
			(where $\Delta_x = x' - x,$ with x' finite)
			(where $\Delta_y = y' - y,$ with y' finite)
			(where $\Delta_x = x' - x,$ with x' finite)
			(where $\Delta_y = y' - y,$ with y' finite)

appropriate applications of the replacement transformation of Sec. 6, Part 1. This use of the replacement transformation will serve to bolster confidence in it as a valid step in the derivation of new Gaussian relationships. Details are developed in Appendix 5, and the resulting equations are restated here. The immediate antecedents of these equations (in Appendix 5), while not restated here, are completely general, and can be very important to the solutions of certain kinds of problems. An instance of their possible use is Example 11, Sec. 25A, which with its check calculations confirms the validity and versatility of the general approach that has been followed in this study. For Case 1, Table 11: by setting $M = 0$, Eq. [340], Appendix 5, produces

$$a = -\frac{1}{M'}(y + \Delta_c y) - \frac{1}{\Delta_c y} M' x' y \quad (x = \infty; \Delta_c x = \infty; M = 0) \quad [205]$$

in which, for a to be finite or zero, M' and $\Delta_c y$ are severally and arbitrarily finite but never zero,* while x' and y are severally and arbitrarily finite or zero. In practice, a must usually be positive. For Case 2, Table 11: by setting $M' = \infty$, Eq. [343], Appendix 5, produces

$$a = \frac{-x'y}{M\Delta_c x} + Mx \quad (y' = \infty; \Delta_c y = \infty; M' = \infty) \quad [206]$$

in which, for a to be finite or zero, M and $\Delta_c x$ are severally and arbitrarily finite but never zero,* while x , x' , and y are severally and arbitrarily finite or zero. In practice, a must usually be positive. For Case 3, Table 11: by setting $M' = 0$, Eq. [347], Appendix 5, produces

$$a = \frac{Mxy'}{\Delta_c y} - \frac{y}{M} \quad (x' = \infty; \Delta_c x = \infty; M' = 0) \quad [207]$$

in which, for a to be finite or zero, M and $\Delta_c y$ are severally and arbitrarily finite but never zero,* while x , y , and y' are severally and arbitrarily finite or zero. In practice, a must usually be positive. For Case 4, Table 11: by setting $M = \infty$, Eq. [349], Appendix 5, produces

$$a = M'(x + \Delta_c x) + \frac{xy'}{M'\Delta_c x} \quad (y = \infty; \Delta_c y = \infty; M = \infty) \quad [208]$$

* It is shown in Sec. 26 and Appendix 6 that for $\Delta_c x$ and $\Delta_c y$ to both be infinite in any case of Table 11, it is necessary that the system be afocal and that $M = M'$. Such requirements make the problem, and its analysis, entirely different from the considerations of this section. See also Sec. 26A, for Example 12.

in which, for a to be finite or zero, M' and $\Delta_c x$ are severally and arbitrarily finite but never zero,* while x and y' are severally and arbitrarily finite or zero. In practice, a must usually be positive.

The antecedents of Eqs. [205] through [208] (in Appendix 5) are readily checked numerically by making substitutions into Eqs. [340], [343], [347], and [349] from the first column of Table 10, Part 2. The numerical parameters to be substituted from that table are assembled and identified in the following tabulation. The parameters are identified by item numbers from Table 9, Part 2; those missing from Table 10 are found in Table 9. The object in each case is to calculate the optical separation a and compare the results with the applicable values of a in the tabulation.

Items	Parameter	For the P-Stage	For the Z-Stage
13 & 49	M	-2.727273	-0.444444
17 & 53	M'	-4.017857	-0.256667
—	$x (= x' - \Delta_c x)$	-8.500000"	-88.162312"
11 & 47	y	0.500000	Zero
5 & 41	x'	-0.500000	-0.500000
—	$y' (= y + \Delta_c y)$	88.162312	10.000000
4 & 40	$\Delta_c x$	8.000000	87.662312
15 & 51	$\Delta_c y$	87.662312	10.000000
—	—	—	—
9 & 45	a (i.e., a_P & a_Z)	23.302584"	39.183211"

Eqs. [343] and [347] produce values of a that exactly check the values of a_P and a_Z in the first column of Table 10. Eqs. [340] and [349] each give $a_P = 23.302577$ inches and $a_Z = 39.183210$ inches. The four equations in question appear to meet this numerical test.

25A. Representative Applications

Example 10: An Instrument With the Sun (or Moon) As Light Source

The instrument is to be constructed for use on an equatorial tracking mount, with the sun or moon as the light source (see Fig. 13). A transparency integral with the instrument is of diameter $d_t = 102$ mm. It is at a distance $x' = -100$ mm from the first principal

* It is shown in Sec. 26 and Appendix 6 that for $\Delta_c x$ and $\Delta_c y$ to both be infinite in any case of Table 11, it is necessary that the system be afocal and that $M = M'$. Such requirements make the problem, and its analysis, entirely different from the considerations of this section. See also Sec. 26A, for Example 12.

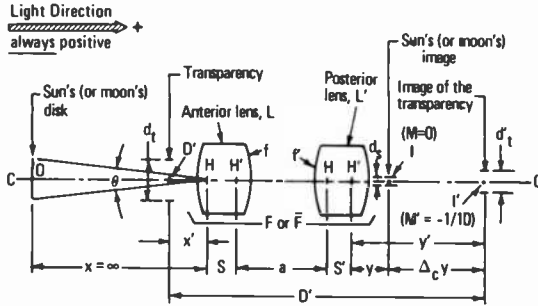


Fig. 13—An optical instrument with the Sun (or Moon) as light source. Schematic only—not to scale.

point of the anterior lens. The sun's image is to be at a distance $y = +25$ mm from the second principal point of the posterior lens. The magnification of the transparency is $M' = -0.10$, and its image is at a distance $\Delta_c y = +75$ mm from the sun's image. Describe the simplest two-lens Gaussian optical system that meets these imaging requirements. Also find the diameter of the sun's (or moon's) image, assuming the naked-eye angular diameter of either source to be $\theta = 1/2^\circ$.

The applicable calculations will be based on the Gaussian parameters of Eq. [205], where

$$\begin{aligned}
 x &= \infty \\
 \Delta_c x &= \infty \quad (= x' - x) \\
 x' &= -100 \text{ mm} \\
 y &= +25 \text{ mm} \\
 \Delta_c y &= +75 \text{ mm} \quad (= y' - y) \\
 M &= 0 \\
 M' &= -0.10 \\
 d_t &= 102 \text{ mm} \\
 \theta &= \frac{1}{2}^\circ
 \end{aligned}$$

By Eq. [205],

$$a = -\frac{1}{M'}(y + \Delta_c y) - \frac{1}{\Delta_c y} M' x' y, \quad \text{given } (x = \infty; \Delta_c x = \infty; M = 0)$$

or

$$a = \frac{-1}{-0.10} (25 + 75) - \frac{1}{75} (-0.10)(-100)(25)$$

or

$$a = 996.667 \text{ mm.}$$

We allow $S = S' = 7.0$ mm, from which, and from Eqs. [163] and [173]

$$D' = a - x' + y + \Delta_c y + S + S'$$

or

$$D' = 996.667 - (-100) + 25 + 75 + 7.0 + 7.0,$$

$$D' = 1210.667 \text{ mm, from } O' \text{ to } I'.$$

By Eq. [159] (on taking due account of the note following Eq. [162]),

$$f = \frac{-M'x'a}{(1 - M')(x' - a) + D' - S - S'}$$

or

$$f = \frac{-(-0.10)(-100)(996.667)}{[1 - (-0.10)](-100 - 996.667) + 1210.667 - 7.0 - 7.0}$$

$$f = 1031.034 \text{ mm.}$$

Likewise, by Eq. [160],

$$f' = \frac{a(x' + D' - S - S') - a^2}{(1 - M')x' + D' - S - S'}$$

or

$$f' = \frac{996.667(-100 + 1210.667 - 7.0 - 7.0) - (996.667)^2}{[1 - (-0.10)](-100) + 1210.667 - 7.0 - 7.0}$$

$$f' = 91.718 \text{ mm.}$$

By Eq. [113], the focal length of the system is

$$F = \frac{ff'}{f + f' - a}$$

or

$$F = \frac{1031.034(91.718)}{1031.034 + 91.718 - 996.667}$$

$$F = 750.000 \text{ mm.}$$

By substituting the expressions for f and f' , from Eqs. [159] and [160], into Eq. [113], a check formula for F is found to be

$$F = \frac{M'x'(x' - a + D' - S - S')}{(1 - M')[(1 + M')x' - a] + D' - S - S'} \quad [209]$$

A simpler check formula, in this particular case, is provided by Eq. [43],

$$F = \frac{-\Delta_c y}{M' - M} \quad [210]$$

Substitutions into Eqs. [209] and [210] give $F = 750.000$ mm (perfect checks!)*

Since the image of the infinitely distant sun is located at the second principal focal point of the system, the image ideally subtends the same angle θ at the second principal point that the sun's diameter subtends at the earth. The radian equivalent of $\theta = 1/2^\circ$ is $\theta_r = 0.008727$ rad. Therefore the ideal diameter of the solar image is

$$d'_s = F\theta_r$$

or

$$d'_s = 750.000(0.008727)$$

$$d'_s = 6.545 \text{ mm}$$

The following calculations of the geometrical speeds (f /numbers or focal ratios) at which the ideal Gaussian images of the sun and the transparency are formed depend upon photometric relationships that are not detailed here, but which can be substantiated by a study of the subject as presented in references 23 through 28 of Part 2.

The solar (or lunar) image of diameter d'_s is formed by the system at an ideal geometrical speed of

$$f \left/ \frac{F}{d_t} \right. = f \left/ \frac{\Delta_c y}{-M' d_t} \right. \quad (\text{see Eq. [210], when } M = 0)$$

or of

$$f \left/ \frac{750}{102} \right. = f \left/ \frac{75}{-(-0.10)(102)} \right.$$

or of

$$f/7.353.$$

The transparency image of diameter d'_t is formed at an ideal geometrical speed of

$$f \left/ \frac{\Delta_c y}{d'_s} \right.$$

* It is noted that if F had first been calculated by Eqs. [209] or [43], then f and f' could have been calculated from Eqs. [63] and [64] of Part 1, by carefully noting Sec. 18, Part 2. It is always possible to use this approach as a check.

or of

$$f / \frac{75}{6.545}$$

or of

$$f/11.459.$$

In order to check the foregoing photometric calculations, it is noted that if light losses in the system are discounted, the amount of light in the image of the transparency equals the light in the image of the primary source (sun or moon). For this reason the diameters of the two images should be in the ratio of the geometrical speeds or f /numbers at which the images are respectively formed. Thus, since

$$d'_i = -M'd_i = 0.1(102) = 10.2 \text{ mm},$$

then

$$\frac{d'_i}{d'_s} = \frac{10.20}{6.545} = 1.5584.$$

The ratio of the corresponding f /numbers that were calculated above is

$$\frac{11.459}{7.353} = 1.5584$$

which checks the ratio of the corresponding diameters perfectly.

Example 11: Designing a Primitive Relay Optical System, Given the Two Object-Distances and the Two Magnifications, and Given a Required Optical Separation for the Two Lenses

The given and calculated parameters are (see Fig. 12):

$$\begin{aligned} M &= -.50 \\ M' &= +3.0 \\ a &= +5.9 \\ x &= -10.0 \\ x' &= +2.0 \\ \Delta_c x &= +12.0 \\ \Delta_c y &= -18.0 \end{aligned}$$

where the unit used for all linear quantities is arbitrary. Here a is the required optical separation of the lenses, and

$$\begin{aligned}\Delta_c x &= x' - x = 2 - (-10) = +12 && \text{(Ref. Eq. [172], Part 2),} \\ \Delta_c y &= MM' \Delta_c x = -0.5(3)(12) && \text{(Ref. Eq. [41], Part 1} \\ &= -18 = y' - y && \text{and Eq. [173], Part 2)}\end{aligned}$$

Note that the solution of this example depends on Eq. [343] of Appendix 5, and the check calculations depend on Eqs. [9] and [10] of Part 1. Derivations of these three equations involved the replacement transformation process of Sec. 6, Part 1. The satisfactory checks may be regarded as a significant confirmation of the trustworthiness of the replacement transformation procedure in Gaussian lens equation derivation and analysis.

Solution of Eq. [343] for y (see Appendix 5),* gives

$$y = \frac{Mx - a}{M'x' - Mx} \Delta_c y \quad (\Delta_c y = MM' \Delta_c x)$$

or

$$\begin{aligned}y &= \frac{-0.5(-10) - 5.9}{3(2) - (-0.5)(-10)} (-18) \\ y &= 16.200000.\end{aligned}$$

By Eq. [173], Part 2,

$$y' = y + \Delta_c y$$

or

$$\begin{aligned}y' &= 16.2 + (-18) \\ y' &= -1.800000.\end{aligned}$$

By Eq. [43], Part 1,

$$F = \frac{-\Delta_c y}{M' - M}$$

or

$$\begin{aligned}F &= \frac{-(-18)}{3 - (-0.5)} \\ F &= 5.142857.\end{aligned}$$

By Eq. [63], Part 1 (upon carefully noting Sec. 18, Part 2)

* In the following, the check calculations depend on storage and use of quantities that are calculated to the maximum accuracy provided by the HP-55 calculator. Such accuracy is usually of no practical use in paraxial calculations, but is useful in judging the reliability of formulas for performing and checking calculations, and therefore the reliability of the theory and general methods on which derivation of the formulas is based.

$$f = \frac{a(Mx - F)}{M(x - a) + (M - 1)F} = \frac{a(M'x' - F)}{M'(x' - a) + (M' - 1)F}$$

On substituting plain values of M and x into Eq. [63]

$$f = \frac{5.9[-0.5(-10) - 5.142857]}{-0.5(-10 - 5.9) + (-0.5 - 1)(5.142857)}$$

$$f = -3.575758.$$

Precisely the same value of f results when M and x are respectively replaced by M' and x' in Eq. [63].

By Eq. [64], Part 1 (note Sec. 18, Part 2)

$$f' = \frac{aFM}{Mx + (M - 1)F}$$

and, by substituting plain M and x into Eq. [64]

$$f' = \frac{5.9(5.142857)(-0.5)}{-0.5(-10) + (-0.5 - 1)(5.142857)}$$

$$f' = 5.589474.$$

An exact check of this value of f' results when M' and x' respectively replace M and x in Eq. [64].

Further check calculations of f and f' will be made by substituting M and x (and also M' and x') into Eqs. [9] and [10], Part 1, taking due note of the procedure described in Sec. 18, Part 2. But before proceeding in this manner it is necessary to obtain D and D' . These are calculated from Eq. [19], Part 1, in the forms $D - S - S'$, and $D' - S - S'$, which may then be substituted directly into Eqs. [9] and [10] (note the discussion of Sec. 18, Part 2):

$$D - S - S' = a - x + \frac{f'[(f - a)x - fa]}{(f + f' - a)x + f(f' - a)}$$

By substituting plain values of x into Eq. [19]

$$D - S - S' = 5.9 - (-10)$$

$$+ \frac{5.589474[(-3.575758 - 5.9)(-10) - (-3.575758)(5.9)]}{(-3.575758 + 5.589474 - 5.9)(-10) + (-3.575758)(5.589474 - 5.9)}$$

$$D - S - S' = 32.100000.$$

When x and D are respectively replaced by x' and D' in Eq. [19],

$$D' - S - S' = 2.100000.$$

The values calculated for the two expressions in D and D' are readily checked by means of Eq. [181] Part 2, by which

$$D - D' = \Delta_c x - \Delta_c y = 12 - (-18) = 30.000000,$$

and also $D - D' = (D - S - S') - (D' - S - S') = 32.1 - 2.1 = 30.000000$. By Eq. [9] (note Sec. 18, Part 2)

$$f = \frac{Ma(-y + D - S - S') - Ma^2}{(1 - M)y + M(D - S - S')},$$

and by substituting the foregoing values of M , y , a , and $(D - S - S')$

$$f = \frac{-0.5(5.9)(-16.2 + 32.1) - (-.5)(5.9)^2}{[1 - (-0.5)](16.2) + (-0.5)(32.1)}$$

$$f = -3.575758.$$

This exactly confirms the values obtained earlier by making substitutions into Eq. [63]. Furthermore, this value is again exactly confirmed by respectively replacing M , y and $D - S - S'$ by M' , y' and $D' - S - S'$ in Eq. [9].

Then, by Eq. [10] (again noting Sec. 18, Part 2),

$$f' = \frac{ay}{(1 - M)(y + a) + M(D - S - S')}$$

into which the values of M , y , a , and $D - S - S'$ are substituted to yield

$$f' = \frac{5.9(16.2)}{[1 - (-0.5)](16.2 + 5.9) + (-0.5)(32.1)}$$

$$f' = 5.589474,$$

which again confirms the earlier values obtained with Eq. [64]. Respective replacement of M , y , and $D - S - S'$ by M' , y' , and $D' - S - S'$ in Eq. [10] again exactly confirms this value of f' .*

As a final check, using Eq. [45], Part 1 (Eq. [113], Part 2),

$$F = \frac{ff'}{f + f' - a}$$

$$F = \frac{-3.575758(5.589474)}{-3.575758 + 5.589474 - 5.9}$$

$$F = 5.142857,$$

just as resulted from Eq. [43], above.

* The reader will also want to make check calculations of f and f' by substituting M , x , and $D - S - S'$ (and also M' , x' , and $D' - S - S'$) directly into Eqs. [7] and [8], Part 1 (after carefully noting Sec. 18, Part 2).

26. The Primitive Afocal Relay Optical System In Air or Vacuum, With One of Its Objects and Also the Corresponding Image At Infinity

It may sometimes be the case with a primitive relay system that one of the objects is at infinity while the corresponding image is also at infinity. Section 25 dealt with cases where the conjugate to the infinite distance, whether the object- or the image-distance, was always finite.

It is easy to guess that when an object and its image are both at infinity, the primitive relay system must be afocal, and this is demonstrated mathematically in Appendix 6, where Eq. [355] states the condition for both conjugates to be infinite as

$$f + f' - a = 0. \quad [214]$$

This condition also makes the system focal length infinite (see Eq. [113]) or the system afocal.

For any primitive relay, Eq. [112] shows the magnification to be

$$M = \frac{ff'}{(f + f' - a)x + f(f' - a)}. \quad [215]$$

This magnification is easily seen to be independent of x when Eq. [214] holds true. The magnification then becomes

$$M = -\frac{f'}{f}. \quad [216]$$

It is not intuitively clear that Eq. [216] correctly expresses the magnification when $x = \infty$, but Eqs. [356] through [359] of Appendix 6 remove any reservation on this point, and they confirm Eq. [216] for an infinite x .

It remains to examine the algebraic location of an infinitely distant image that an afocal primitive relay system produces of an infinitely distant object. Appendix 6 derives Eq. [363] to show that the general image-distance y is

$$y = -M \left[\frac{f'}{f} x + (f + f') \right] \quad (x \text{ finite}). \quad [217]$$

For very great values of x , when M is finite, Eq. [217] becomes simply

$$y = -M \frac{f'}{f} x \quad (x = \pm\infty). \quad [218]$$

and when we substitute the value of M from Eq. [216], we may write either

$$y = M^2x \quad (x = \pm\infty) \quad [219]$$

or

$$y = \left[\frac{f'}{f} \right]^2 x \quad (x = \pm\infty) \quad [220]$$

from either of which x and y are infinities of the same sign, independent of the sign of M , or of the signs of f and f' .

Eqs. [216] and [220] describe the action of a Galilean telescope and also that of a simple Keplerian or astronomic telescope. In the Galilean, f is positive and f' negative, making M positive and the image upright. In the Keplerian, both focal lengths are positive and the image is inverted. In the cases of both telescopes the image appears at $y = -\infty$ (exactly where the object appears without a telescope but with telescopic magnification $M_T = 1/M$; see portion of Appendix 6 following Eq. [363], especially the last six paragraphs).

An image at $-\infty$ is formed in parallel light by either telescope, each point in the image being represented at the optical system by a separate bundle of parallel rays that is leaving the eyepiece and entering the eye. In a *limited* sense there is no optical distinction between an image-point being at $-\infty$ and being at $+\infty$, since to say that an image-point is at either infinity is merely to say that the rays that correspond to it in the image-space are parallel to each other. Conversely, parallel rays may be considered to meet both at positive infinity and at negative infinity. The Galilean and Keplerian telescopes, therefore, produce virtual images at negative infinity but also real images at positive infinity. This being the case, there is a further distinction between the virtual and real images, which is illustrated by Eq. [218]. If the values of f , f' , and $x = \pm\infty$ are held constant, then it is clear from the equation that reversal of the sign of y implies a reversal of the sign of M . Thus, when $x = -\infty$, the Galilean and Keplerian telescopes both produce virtual images at $y = -\infty$ and at magnifications $M = -f'/f$; but at the same time they produce real images at $y = +\infty$, and at magnifications $M = +f'/f$. This is the meaning of the references to magnification in the footnotes to Sec. 16, Part 2. Moreover, any telescope or optical instrument that produces an image at a noninfinite distance produces only one image at one magnification.

26A. A Representative Application

Example 12: Design of A Simple Keplerian Type Afocal Telescope For Use at A Specified Finite Object-Distance (See Fig. 14)

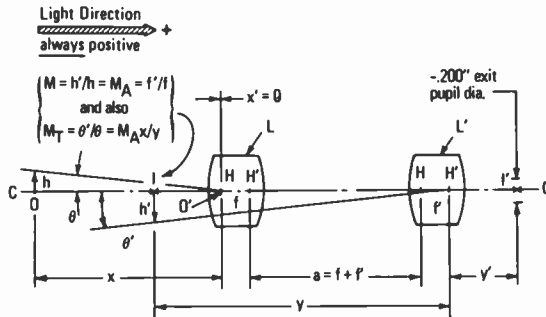


Fig. 14—Strictly afocal Keplerian telescope for viewing finitely distant object at predetermined telescopic magnification M_T . Schematic only—not to scale.

A Keplerian (astronomical type) telescope is required to view an object at -300 feet from its objective lens. Its telescopic magnification for that object-distance is to be -5.0 . The distance from the second principal point of the eyepiece to the exit pupil is to be 0.937 inch, and the distance from the pupil to the inverted image of the object is to be algebraically no greater than -1.0 meter. The exit pupil diameter is to be -0.200 inch. The telescope is to be afocal under its intended condition of use. The following discussion of the problem is best understood if the reader will first review Appendix 6.

A tabulation of the Gaussian requirements and the unknown quantities is

x	$= -3600$ inches	a	$=$ Unknown
y	$=$ Unknown	$M = M_A$	$=$ Unknown
x'	$=$ Zero	f	$=$ Unknown
y'	$= +0.937$ inch	f'	$=$ Unknown
M_T	$= -5.0$	Exit pupil diameter	$= -0.200$ inch

The afocal requirement dictates, by Eqs. [355] and [359], that

$$a = f + f' \tag{221}$$

and

$$M = -\frac{f'}{f} \tag{222}$$

From Eq. [365], we may write

$$M = M_T \frac{y}{x} = M_A, \quad [223]$$

and since $M (=M_A)$ is constant for all $\{x,y\}$ in the case of an afocal system, we may write, from Eqs. [149], [172], and [173],

$$y' - y = M_A^2(x' - x). \quad [224]$$

On making substitution for M_A from Eq. [223] and reducing to standard quadratic form

$$\frac{M_T^2(x' - x)}{x^2} y^2 + y - y' = 0, \quad [225]$$

the solution of which for y is

$$y = \frac{-x^2}{2M_T^2(x' - x)} \pm \sqrt{\frac{x^4}{[2M_T^2(x' - x)]^2} + \frac{x^2 y'}{M_T^2(x' - x)}}. \quad [226]$$

The dependence of this solution on the conjugate displacement theorem, in the form of Eqs. [149] and [224], is clear. By substituting the appropriate quantities from the list of requirements into Eqs. [226] and [223],

$$y = -144.9309811 \text{ inches} = -3.681246920 \text{ m} (< -1.0 \text{ m, as required})$$

$$M(=M_A) = -0.2012930293 = \text{constant for the afocal system.}$$

Therefore, in order for the exit pupil diameter to be -0.200 inch, as required, the objective lens diameter must be $-0.200 \text{ inch}/M_A = 0.993576383$ inch. (All of the significant figures provided by the computer are retained only for the purpose of making check calculations easy and convincing.)

In terms of the primed requirements of the tabulation, and noting that $M(=M_A) = M'$ for an afocal system, we write from Eq. [363]

$$y' = -M \left[\frac{f'}{f} x' + f + f' \right] \quad M = M_A = \text{constant} \quad [227]$$

from which, since $x' = \text{zero}$

$$f + f' = \frac{y'}{-M}$$

$$f + f' = 4.654905355 \text{ inches.}$$

From Eq. [222]

$$\frac{f'}{f} = -M = 0.2012930293$$

and solution of the preceding two equations in f and f' gives

$$f = 3.874912484 \text{ inches} = y'/[-M(1 - M)]$$

$$f' = 0.7799928722 \text{ inch,}$$

with Eq. [221] giving

$$a = 4.654905356 \text{ inches.}$$

If it is desired to find the value of x for the afocal telescope when y has the assumed practical maximum algebraic value of -1 m ($= -10^4/254$ inches) we solve Eq. [363] for x (remembering the relationship of Eq. [222]) to get the linear relation

$$x = \frac{y + M(f + f')}{M^2}, \quad M = M_A = \text{constant} \quad [228]$$

or, on substituting the given and previously calculated numerical values of the variables,

$$x = -994.7726867 \text{ inches} = -82.89772389 \text{ feet.}$$

Furthermore, although $M(=M_A)$ is constant, M_T depends on $\{x, y\}$ as expressed by Eq. [365]. Thus

$$M_T = \frac{Mx}{y}, \quad M = M_A = \text{constant}$$

and, by numerical substitution ($x = -994.7726867$ inches; $y = -1 \text{ m} = -10^4/254$ inches)

$$M_T = -5.086116513.$$

$$\text{By Eq. [367], } M_T = \frac{1}{M_A} = \frac{1}{-0.2012930293} = -4.967881916,$$

when x (and y) $= -\infty$. Therefore, when y decreases algebraically from $y = -1 \text{ m}$ to $y = -\infty$ in this particular telescope, the monotonic change in the value of M_T as x changes from $x \approx -995$ inches (for $y = -1 \text{ m}$) to $x = -\infty$ is only about 2.4%; therefore M_T , though variable, does not undergo large changes as x varies through the indicated range. In a practical telescope the posterior lens or eyepiece will be movable for focusing to suit individual observers, and this will have a further influence on M_T that is not discussed here. Depending also on the amount of motion that is provided for the eyepiece, satisfactory viewing at object-distances much greater (algebraically) than $x = -995$ inches will be possible, and these possibilities should be studied by the reader. The telescope will not be truly afocal, however, under conditions where the optical separation of the two lenses is $a \neq f + f'$.

Equation [225] is useful as a check on the values obtained above for x and M_T , when $y = -1$ m. The equation will be useful in understanding the algebraic structure of specifications for other afocal variants of Example 12, which the reader will find it instructive to formulate and solve.

27. The Regular and Inverse Relaying Actions of Any Non-Afocal, Centered Spherical Lens or Lens System In Air or Vacuum

By way of orienting the reader to the discussions in this and the following sections, "relaying action" will not be restricted to that of the primitive, separated two-lens relaying systems of the preceding sections (including those of Part 2), but will be extended to include any centered system of spherical refracting surfaces in air or vacuum. As in the case of the primitive relay system, "relaying action" will assume the production of images of two fixed object-points that are spaced apart at perfectly general object locations along the system axis; it will, however, *not necessarily* be assumed to do so in a manner that conserves the light (see Abstract and Sec. 13, Part 2). In what follows, "relaying action" will be considered from a less restricted and much more general point of view, and will correspondingly lead to very general conclusions regarding any non-afocal optical system whose actual or prospective "relaying action" is under consideration.

Also, it was convenient and helpful, in the introductory discussion of the primitive relay system in Part 2 to refer to the relative order of the two objects O and O' on the system axis (as well as to the relative order of the two images I and I') by the terms "anterior" and "posterior," respectively. The meaning of these terms was indicated in the footnote to Sec. 16.

Such terminology is, however, inconveniently restrictive when applied to general object- and image-points, and it is not well suited to a discussion of the relaying action of a generalized lens or lens system. It is much better, for example (see Fig. 12), if starting with the object-space of the system to simply and permanently define the object-distance of an arbitrarily located O as X , and of an arbitrarily located O' as X' ,* and to note that their relative order along the

* Here, upper case X , Y , X' , and Y' represent Gaussian object- and image-distances that are measured from the corresponding principal points (\bar{H} or \bar{H}') of any lens or optical system. They are related by: $\Delta_c x = X' - X$; $\Delta_c y = Y' - Y$; $M = Y/X$; $M' = Y'/X'$; and by the conjugate displacement theorem, $\Delta_c y = MM' \Delta_c x$ (see Sec. 10, Part 1). An infinitely distant \bar{H} or \bar{H}' requires the optical system to be afocal (see Sec. 26).

axis is indicated by the object displacement $\Delta_c x = X' - X$, which is positive when X' is algebraically greater than X , and negative when it is less. If starting with the image-space of the system, we would permanently define the image-distance of an arbitrarily located I as Y , and of an arbitrarily located I' as Y' ,* and note that their relative order is indicated by the image displacement $\Delta_c y = Y' - Y$, which is positive when Y' is algebraically greater than Y , and negative when it is less. Displacement $\Delta_c x$ is *always* in the direction from O to O' , and $\Delta_c y$ in the direction from I to I' . Under the Gardner sign convention, a displacement from O to O' (or from I to I') is *always* in the direction of light travel when $\Delta_c x$ (or $\Delta_c y$) is positive, and opposed to the direction of light travel when the displacement is negative.

It is always important to remember that the distances X and Y and magnification M pertain *only* to the conjugate points O and I , and that the distances X' and Y' and the magnification M' pertain *only* to points O' and I' .

As a matter of general interest, displacements $\Delta_c x$ and $\Delta_c y$ may be explicitly related in any optical system by making suitable substitutions for M and M' into later Eq. [232] from Table 1, Part 1. When any such relationship is used to calculate $\Delta_c y$ from $\Delta_c x$, for example, we may say that the given x -displacement ($\Delta_c x$) is "carried through" as a y -displacement ($\Delta_c y$). The result of such a carry-through appears as a signed numerical value of $\Delta_c y$. The sign immediately indicates the order of I and I' along the axis referred to the light direction, provided that the Gardner sign convention has been carefully adhered to in making *all* of the relevant antecedent calculations.

By substitutions into Eq. [232] from Table 1, V-2,

$$\Delta_c y = \frac{f^2}{(f + X)(f + X')} \Delta_c x \quad \text{where } \Delta_c x = X' - X. \quad [229]$$

By the replacement transformation of Sec. 6, and noting Appendix 5, Eq. [229] transforms into

$$\Delta_c x = \frac{f^2}{(f - Y)(f - Y')} \Delta_c y \quad \text{where } \Delta_c y = Y' - Y, \quad [230]$$

which is verifiable from Table 1, V-5, by inspection.

From Eq. [181], Part 2, substitutions into it from Table 1, I-2, produce

$$\Delta_c y = \frac{X^2}{f + X} - \frac{X'^2}{f + X'} + \Delta_c x \quad \text{where } \Delta_c x = X' - X. \quad [231]$$

This matter is not discussed further here, but it does suggest added possibilities for usefulness of the simple Gaussian lens equations through applications of the conjugate displacement theorem. If the substitutions from Table 1 are made in terms of mixed variables, such as in terms of X for M , and in terms of Y' for M' , difficulties arise that are not examined further at this point.

In any configuration of a system and its associated object- and image-points, if the members of any conjugate displacement pair $\Delta_c x$ and $\Delta_c y$ are both finite and have the same sign, whether positive or negative, the system is defined as having a *regular* relaying action for that pair of displacements. If the members of any conjugate displacement pair are opposed in sign, the system is defined as having an *inverse* relaying action for that pair. A system may have a regular relaying action for one pair of object-points (or image-points), and an inverse relaying action for some other pair.

For systems of finite focal length (non-afocal systems), the relaying action is primarily dependent on the positions of the objects, or of the images, along the system axis. The conjugate displacement theorem

$$\frac{\Delta_c y}{\Delta_c x} = MM' = M_\Delta \quad [232]$$

(where the M_Δ symbol is introduced for convenience and is called the displacement magnification) makes it obvious that in the case of regular relaying action ($+\infty \neq M_\Delta > 0$), the two magnifications M and M' must have the same sign. It is similarly obvious that the magnifications must have opposed signs in the case of inverse relaying action. The converse of these statements is also true, the relaying action being necessarily regular ($+\infty \neq M_\Delta > 0$) if the magnifications have the same sign, but inverse ($-\infty \neq M_\Delta < 0$) if the signs are opposed.

It is instructive and useful to consider how two axial object-points, or two axial image-points, are related to a lens or lens system when their magnifications have the same sign, and also when they have opposed signs. The details are developed in Appendix 7 in terms of Newtonian conjugate distances X_N , Y_N , etc. (instead of the usual Gaussian conjugate distances X , Y , etc.). The results are summarized in Table 12, where they are intelligibly related to the regular and inverse relaying actions of a lens or lens system.

In Table 12, the signs (indicated in each row by P or N, for positive or negative, respectively) of f , M , M' , and M_Δ , are related to the signs of the members of the two Newtonian conjugate distance pairs X_N , Y_N , and X'_N , Y'_N , as indicated in each row of the tabulation.

Table 12—Schedules of The Eight Optically Possible Sign Groupings of The Eight Parameters of Columns (1) Through (8), In Any Centered Non-Afocal System of Spherical Surfaces in Air or Vacuum When Used as a Relay (see Appendix 7). *N*-subscripts (as in X'_N) Identify Object- and Image-distances as Newtonian (see Appendix 7). *X*, etc., without subscripts is Gaussian. See Eqs. [371] and [372] of Appendix 7 and of Columns (2)* through (5)'.

Column Nos.:	(1)	(2)*	(3)'	(4)*	(5)'	(6)*	(7)'	(8)	(9)
Parameter	$f \approx 0$	X_N	X'_N	Y_N	Y'_N	M	M'	M_Δ	Relay
In Reference To:	Finite Focal Length	Object O	Object O'	Image I	Image I'	Mag. O to I	Mag. O' to I'	Displacement Mag.	Action Regular Or Inv.
<i>Group Nos.</i>									
I.	P	P	P	N	N	P	P	P	Regular
II.	P	P	N	N	P	P	N	N	Inverse
III.	P	N	P	P	N	N	P	N	Inverse
IV.	P	N	N	P	P	N	N	P	Regular
V.	N	P	P	N	N	N	N	P	Regular
VI.	N	P	N	N	P	N	P	N	Inverse
VII.	N	N	P	P	N	P	N	N	Inverse
VIII.	N	N	N	P	P	P	P	P	Regular
Equations That Express Column Parameters									
	$-f^2 = X_N Y_N$ $= X'_N Y'_N$	$X_N = X + f$	$X'_N = X' + f$	$Y_N = Y - f$	$Y'_N = Y' - f$	$M = fX_N$ $= -Y_N/f$	$M' = fX'_N$ $= -Y'_N/f$	$M_\Delta = MM' = \Delta_o/\Delta_x$ $= f^2/X_N X'_N = Y_N Y'_N/f^2$ $= -Y'_N X_N = -Y_N X'_N$	see Eq. [373]
	see Eq. [371]	see Eq. [371]	see Eq. [371]	see Eq. [372]	see Eq. [372]	see Eq. [374]	see Eq. [374]	see Eq. [375] & [376].	Eq. [232]

Each of the preceding eight parameters is assumed $\neq 0^*$ and also $\neq \infty$. The Newtonian object- and image-distances are measured from the principal focal points, as described in the second and third footnotes (p. 158) to Appendix 7 and illustrated in Fig. 15. Table 12 is divided into two parts according to the sign of the focal length, whether P ($f > 0$) or N ($f < 0$). The sequence of the relaying actions in column (9) is the same in each part of the table.

The eight parameters, whose signs are related in Table 12, appear at the heads of the first eight parenthesized, Arabic numbered columns. The asterisked, even numbered columns relate the object O to image I and to the O-to-I magnification M . The single-primed, odd numbered columns similarly apply to the set O', I', M' . In the columns, positive values of the parameters at their heads (such as $X'_N > 0$) are indicated by the letter P; negative values (such as $M_\Delta < 0$) are indicated by the letter N. P-values of the Newtonian conjugate distances correspond, under the Gardner sign convention, to the object- and image-points being posterior to the respective principal foci from which they are measured. N-values similarly correspond to the points being anterior to the respective principal foci from which their distances are measured (see footnote to Sec. 16, Part 2; also Sec. 17, second and third footnotes (p. 158) to Appendix 7, and Fig. 15).

Consistent with the applicable relationships of Newtonian imagery that are developed in Appendix 7, the fixed signs of the eight parameters of Table 12 fall into eight distinct groupings that together represent *all* of the two-object relaying actions that are possible to any centered, non-afocal system of spherical lenses in air or vacuum. Each such grouping is represented in the table by a row that is group-numbered by a Roman numeral group number. At the bottom of each column is an equation or continued equation that is pertinent to the parameter at the head of the column. Taken together, these equations summarize Eqs. [371], [372], [373], [374], [375], and [376] of Appendix 7, and they should facilitate use of the table.

The reader can readily comprehend the preceding statements regarding the general form and content of Table 12 by observing that the rationale of its structure is based on the following three considerations abstracted from Appendix 7.

* The absolute difference between any one of them and zero, however, may be small without restriction, somewhat in the manner of an infinitesimal variable in the calculus.

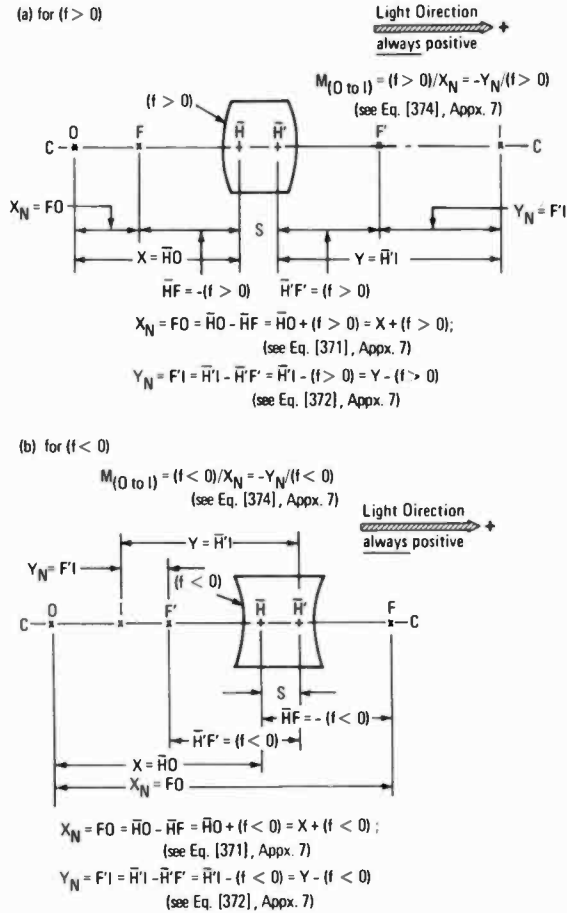


Fig. 15—The Newtonian conjugate distances X_N and Y_N and the Gaussian conjugate distances X and Y applied (a) to a non-afocal system of positive focal length ($f > 0$) and (b) to a non-afocal system of negative focal length ($f < 0$). Schematic only—not to scale. Applicable equations that support the expressions for X_N , Y_N , and M are Eqs. [371], [372], [373], and [374] of Appendix 7 also in Table 12, Columns (2)*, (4)*, (1), and (6)*, respectively. The expressions hold true independently of the location of object O on the system axis. O is the axial object-point; I is the axial image-point; M is the magnification (O to I). \bar{H} and \bar{H}' are, respectively, the “first” and “second” principal points of system; $S = \bar{H}\bar{H}'$, positive if $\bar{H}\bar{H}'$ is in direction of light travel, negative if otherwise or zero. F and F' are, respectively, “first” and “second” principal focal points of system.

1. The signs of X_N and Y_N (also of X'_N and Y'_N) must be opposed (see Eq. [373]).
2. When M_Δ is positive (the regular relaying action), M and M' have like signs, otherwise they have opposed signs (see Eq. [232]).
3. For a lens of *fixedly* signed focal length $\pm|f|$, reversal of the sign of M (or of M') also reverses the sign of *both* X_N and Y_N (or those of *both* X'_N and Y'_N , see Eq. [374]). Reversal of the signs of *both* M and M' reverses the sign of each of X_N , Y_N , X'_N , and Y'_N .

Any Roman-numeraled line of Table 12 conforms to the foregoing considerations and to the accompanying equation references. The following consideration is useful also, as a check of the table.

4. For a lens of non-fixedly signed focal length f , at *fixedly signed* magnification M (or M'), reversal of the signs of *both* X_N and Y_N (or of *both* X'_N and Y'_N) reverses the sign of the focal length (see Eq. [374]). If the sign of each of X_N , Y_N , X'_N , and Y'_N is reversed, the sign of the focal length remains unchanged, assuming signs of M and M' remain fixed.

Table 12 facilitates study of the relationships between the Newtonian parameters of a two-object relaying problem in the most general terms, without making detailed analytical deductions or numerical calculations. The table shows, for example, that if the signs of f and X_N remain unchanged, then reversal of the sign of X'_N will *always* reverse the signs of M' and M_Δ . It reverses the relaying action from regular to inverse or vice versa. On the other hand, if the sign of f remains unchanged, then reversal of the signs of *both* X_N and X'_N leaves the sign of M_Δ unchanged; that is, the relaying action remains either regular or inverse, the same as before any change of signs; but the signs of *both* M and M' are reversed.

A change of the sign of X_N , or of both X_N and X'_N , when the sign of f is *fixed*, always mandates certain changes in the signs of some or all of Y_N , Y'_N , M , and M' , according to the schedules of Table 12. In general, if the sign of only one of the eight parameters is fixed, then four of the sign groupings of the table are potentially applicable. If the signs of two independent parameters are fixed,* then only two of the sign groupings are possible. If the signs of any three parameters are fixed, one or two of the sign groupings of the table

* The parameters in the asterisked even-numbered columns are considered to be independent of those in the single-primed odd-numbered columns, and all are considered independent of the focal length.

may be available for consideration. If the sign of *no* parameter is predetermined to remain fixed, then all eight sign groupings are offered by Table 12 as possible bases for relaying or carrying through an axial displacement $\Delta_c x$ as an image displacement $\Delta_c y$.

No sign groupings of the four Newtonian parameters X_N , Y_N , X'_N , and Y'_N with the four parameters f , M , M' , and M_Δ other than those of Table 12 are optically possible, and any proposed sign groupings that are outside this schedule are non-optical and cannot be realized with any imaging system comprising centered spherical surfaces in air or vacuum. Such non-optical groupings define yet another category of excluded cases (see the discussions of excluded cases, Sec. 22, Part 2).

Although the use of the Newtonian conjugate distances X_N , Y_N , X'_N , and Y'_N has eased the initial task of assembling Table 12 and giving it a simple form, the Newtonian lens equations do have certain disadvantages when doing paraxial lens calculations. As an example of this, Eqs. [373] and [375] result in an inconveniently ambiguous algebraic sign when they are solved for f . The result is that further work must be done to establish the sign. On the other hand, solutions of any of the Gaussian equations of Table 1 for f result in a definite sign. It is true that the solutions of Gaussian equations (as for example Eq. [16], Part 1) sometimes involve a double sign, but in most cases its interpretation is reasonably simple and straightforward. The ambiguity of the value of f , in the Newtonian parameter system, appears general (see Eqs. [380] and [384], Appendix 7).

The discussions of the following Secs. 28, 29, and 29A will be based on the conclusions of the present Sec. 27.

28. Introductory Comments Respecting the Purposes and Procedures of the Following Sections Through Section 29A

In Sec. 27, the ideas of regular and inverse relaying actions for any non-afocal optical system were introduced. This led to an examination of the various optically valid sign groupings that may exist among the applicable signed parameters in relaying actions generally. The initial sign groupings were most easily developed from the Newtonian lens equations and were collected in Table 12.

The purpose of the following sections is to develop the various optically valid sign groupings that may exist among the applicable signed parameters, in non-afocal relaying actions generally, when the sign groupings are those of the parameters of the Gaussian equations.

There may be more than one way of doing this. In the procedure to be developed here, equations and inequalities are established that contain some of the parameters of *both* Newtonian and Gaussian equations. From analysis of these mixed relationships, the required Gaussian sign groupings as well as the corresponding Newtonian sign groupings may be separated out. While there were eight such Newtonian sign groupings in Table 12, the Gaussian sign groupings number eighteen in Table 15 (in Part 3, Section B, as yet unpublished). A simpler procedure to establish the Gaussian sign groupings would be desirable, but it has not been found.

The procedures of the following two sections and their associated two appendices are partially based on equations that are developed in Appendix 7. The use of inequality algebra in these procedures is facilitated by the use of fixedly signed variable parameters (signets) in the form of explicit inequalities whose second terms are zero.*

29. Working With Algebraically Ordered Relationships Between Signed Literal Values of X_N , X , and f and With Those Between Y_N , Y , and f . Also, Derivation of Mixed Newtonian and Gaussian Inequality Systems, With Literal Variables That Have Fixed Signs and Fixed Order. Their Separation Into Systems of Conjugate Newtonian and Conjugate Gaussian Inequalities.

It is useful to be able to quickly decide, without making any numerical calculations, if a proposed arrangement between any non-focal lens system and an object and its image (all in air or vacuum) is consistent or inconsistent with the relationships of Gaussian imagery that are represented by Eqs. [1] and [2] of Part 1. Such a decision is greatly assisted by developing a set of six mixed Newtonian and Gaussian inequality systems, *in each of which* X_N , X , Y_N , Y , f , and M are all fixed in sign, and *in each of which* the

* An inequality that relates a single variable to zero identifies the sign of the variable and will be called a signatory inequality, or simply a "signet." Signets of different kinds, as $(X > 0)$ and $(f < 0)$, may be combined into forms such as $-(X > 0) < (f < 0)$, which will be called metrical inequalities, or simply "metrics"; or, more particularly, since they contain no non-signets, non-numerical metrics, or simply "nn.-metrics." A form similar to $(M > 0) > n$, where n is some literal or numerical non-signet, is also a metric; or, more particularly, since it contains a non-signet, it is a numerical metric or simply an "n.-metric." By substituting signets into an ordinary algebraic equation, it may be solved for a metric (see Appendix 8), thus usefully relating ordinary algebra to the algebra of inequalities.

The terms "signet," "metric," "nn.-metric," and "n.-metric" will be used in the discussions and referenced appendices that follow.

relationships of algebraic order among the conjugate distances and also between them and the focal length are fixed.

I. Deriving Inequalities of Fixed Order (nn.-Metrics) That Relate Literal Variables With Fixed Signs (Signets)*

As a first step in characterizing the mixed Newtonian-Gaussian inequality systems, it is noted that the signs of X_N and X (as determined by the Gardner sign convention) are unlike when the axial object-point is between the first principal point and the first principal focal point of the system (see footnotes that follow Eq. [372] in Appendix 7; also Fig. 15). The signs are alike whenever the object-point is elsewhere on the axis. Also, the signs of Y_N and Y are unlike when the axial image-point is between the second principal point and the second principal focal point, but they are alike whenever the image-point is elsewhere on the axis.

Development of the desired literal inequality systems is at first approached through a group of inequalities that is derived in the text, in Appendix 8, and preliminarily collected in Table 13. The inequalities of that table are grouped according to the unlikeness or the likeness of the signs of X_N and X and of those of Y_N and Y . When the signs are alike there are two inequality subgroups, *a.* and *b.*, that are, respectively, applied to the cases of negative signs and of positive signs. Each group is identified by an Ineq.-number and also by a subgroup letter (*a.* or *b.*) where applicable. The groups will be called up from Table 13 as Ineq. [237] or as Ineq. [240] *b.* and so on. Each group or subgroup is also given an identifying Roman numeral case number that is sometimes more convenient to use.

The literal inequalities, in any one group or subgroup of Table 13, involve double (upper and lower) symbols of inequality. The subgroups also involve some single inequality symbols. The inequalities identified by a *given* Ineq.-number *must* either *all* be used with their upper (superscripted) inequality symbols, or else they *must all* be used with their lower (subscripted) symbols. For this reason it may sometimes be appropriate to call up an inequality as Ineq. [237]^{sup}, or as Ineq. [240]_{b.sub}, for example. The same two inequalities can also be respectively called up from the table as Case I^{sup} and as Case VI_{sub}. A single inequality symbol is *always* used as given.

* See footnote p. 136.

Magnification M is not an explicit variable in any of the inequalities, but its sign is implicit in the signs of X_N and f , or in those of Y_N and f that occur in each of them (see Eq. [374]). It is also implicit in the signs of X and Y (see Eq. [2]).* The sign of M for each inequality is determined accordingly from the relationships of Eq. [374], Appendix 7, and the appropriate sign or signs of the magnification is included in each of the lines 1 and 2 of Table 13. The rule respecting the manner of using the double or single inequality symbols that are applied to M is the same as in the preceding paragraph.

In any group or subgroup of Table 13, line 1 indicates the signs and relative order of X_N and X (or of Y_N and Y) as well as the corresponding signs (or sign) of f and M . Line 2 primarily states the relative order of f with respect to either X_N or X (or either Y_N or Y) as it depends on the sign of f ; the sign information respecting M in line 1 is repeated in this line. In no case is there a conflict between the signs and orderings of lines 1 and 2 in any given group or subgroup.

The dependence of the sign of f on the algebraic order of X_N and X derives from the solution of Eq. [371] Appendix 7 (and Table 12) for f , or

$$f = X_N - X \quad [233]$$

from which

$$f \geq 0 \text{ corresponds to } X_N \geq X. ** \quad [234]$$

Furthermore, from the solution of Eq. [372] Appendix 7 (and Table 12) for f

$$f = Y - Y_N \quad [235]$$

from which

$$f \geq 0 \text{ corresponds to } Y_N \leq Y. ** \quad [236]$$

* The sign of each of the given variables is represented by signets ($X > 0$), ($f < 0$), respectively, positive and negative, and similarly. The numerical value of any variable can be close to zero without restriction, somewhat in the manner of infinitesimal variables in the calculus. The signs of the variables are fixed, and they are unaffected by any and all permissible algebraic operations that involve the external algebraic signs and inequality symbols that relate the signets to each other (see footnote 3, Table 14).

** Note that in Table 13 the form of the entity ($f \geq 0$) never varies, the $>$ symbol always being uppermost (sup).

II. Analytical Development of Table 13 (Referred to Appendix 8).

Further details of the development of Table 13 are suggested in Appendix 8. Their use in constructing Table 13 is outlined in this and the following two paragraphs. In Table 13, Ineq. [237] line 1 is taken from Ineq. [389] Appendix 8. Also, Ineq. [239] line 1 is derived by treating Ineq. [236] in a manner parallel to the development of Ineq. [389]. On the other hand, Ineq. [237] line 2, for the condition of unlike signs of X_N and X , is derived from Ineqs. [391] and [393] jointly.

Inequalities [238]a. and b., lines 1 (Table 13), are respectively derived as the Appendix 8 Ineqs. [394] and [395]. But Ineq. [238]a. line 2 is conveniently derived from Ineqs. [396] and [397], Appendix 8, jointly. Ineq. [238]b. line 2 of the Table similarly derives from Ineqs. [398] and [399], Appendix 8, jointly.

The remaining inequalities of Table 13 are developed by a continuation of the general processes of Appendix 8, using Eq. [235], Ineq. [236], and the derived counterparts of Ineqs. [388] and [390] Appendix 8 that are in terms of Y_N and Y . Readers will wish to develop the details for themselves, as there suggested.

Any part of Table 13 may be quickly and easily checked by application of the general process of Appendix 8, as outlined in the preceding three paragraphs.

Note that in general the "forward" expression $m > n$ is the full equivalent of its "backward" form $n < m$ and that in practice one of these forms may be easier to work with than the other, depending on need or circumstance. For example, we may read Ineq. [237]^{sup} line 1, Table 13, as

$$(X_N > 0) > (X < 0); (f > 0); (M > 0);$$

in order to make the *unlikeness* of the signs of X_N and X more readily apparent. As this line 1 is actually written in Table 13, it has a different emphasis that makes the *relationship of order* of Ineq. [234], between X_N and X , stand out clearly in support of that between f and zero.

III. Conjugate Pairing of the Inequalities (nn.-metrics)* of Table 13.

Conjugate pairing is important to the construction of Table 14. In Table 13 the compactly presented Newtonian and Gaussian inequalities are conveniently but arbitrarily arranged according to

* See footnote in Sec. 28, p. 136.

cases, as defined in the left hand column of the table. The inequalities have their maximum significance and usefulness, however, if they are arranged in conjugate pairs or systems. A conjugate system is here broadly defined as any pair of inequalities in X_N and Y_N , from lines 2 of Table 13, that share the same focal length ($f \geq 0$) and, *independently of the sign of f* , share the same magnification ($M \geq 0$).

We start by considering the conjugate pairing of inequalities for which ($M < 0$). In Table 13 lines 2 there are two inequalities in X_N (Cases II^{sup} and III_{sub}) and two in Y_N (Cases V_{sub} and VI^{sup}) for which ($M < 0$). In Cases II^{sup} and VI^{sup} the corresponding focal length is ($f > 0$), and in Cases III_{sub} and V_{sub} it is ($f < 0$). These relationships provide the basis for the conjugate pairings No. 5 and 6 of Table 14.*

A further examination of Table 13 lines 2 reveals four inequalities in X_N and four in Y_N for which ($M > 0$). Conjugate pairing among these eight inequalities cannot be based on ($f \geq 0$) and ($M > 0$) alone, and it is necessary to arbitrarily expand the ($M > 0$) criterion into the double, or match-keying, n.-metric criterion ($M > 0$) ≥ 1 . Thus, by Eq. [374], Appendix 7, and Table 12, the match-keying n.-metric

[A] ($M > 0$) > 1 implies that (see Ineq. [237], Case I, Table 13)

$$[(M > 0) > 1] = \frac{(f \geq 0)}{(X_N \geq 0)}, \text{ which can be true only when}$$

$$(f \geq 0), (X_N \geq 0), \text{ and } |f| > |X_N|, \quad [241]$$

also it implies that (see Ineq. [239], Case IV, Table 13)

$$[(M > 0) > 1] = \frac{-(Y_N \leq 0)}{(f \geq 0)}, \text{ which can be true only when}$$

$$(Y_N \leq 0), (f \geq 0), \text{ and } |Y_N| > |f|. \quad [242]$$

Note: In Ineq. [239] the second implication of [A] is *not* true; see methods of third following paragraph.

Then, also by Eq. [374], the match-keying n.-metric

[B] ($M > 0$) < 1 implies that (see Ineq. [237], Case I, Table 13)

$$[(M > 0) < 1] = \frac{(f \geq 0)}{(X_N \geq 0)}, \text{ which can be true only when}$$

* It is emphasized that the "systems" of Table 14 are not merely systems of lenses; they are sets of inequalities in terms of X_N , Y_N , or X , Y , and f , (and M) with fixed signs and order in conjugately paired relationships. They include *all* of the possibilities of Gaussian imagery that are represented in Eqs. [1] and [2] of Part 1.

$$(f \geq 0), (X_N \geq 0), \text{ and } |f| < |X_N|, \quad [243]$$

also it implies that (see Ineq. [239], Case IV, Table 13)

$$[(M > 0) < 1] = \frac{-(Y_N \leq 0)}{(f \geq 0)}, \text{ which can be true only when}$$

$$(Y_N \leq 0), (f \geq 0), \text{ and } |Y_N| < |f|. \quad [244]$$

Note: In Ineq. [237] the first implication of [B] is *not* true; see methods of second following paragraph. These considerations then become the basis for the conjugate pairings of Systems No. 1 through 4 of Table 14, where two cases of Table 13, lines 2, can be conjugately paired only if $(M > 0) > 1$ for both, or else only if $(M > 0) < 1$ for both. Obviously Cases I and IV, Table 13, cannot be conjugately paired, for they have *unlike* n.-metric matching-keys.

From the preceding paragraphs, it is seen that the conjugate pairings depend on the orderings of $|X_N|$ and $|f|$ and those of $|Y_N|$ and $|f|$ in every case where $(M > 0)$. These orderings are inherent in the inequalities of each case of Table 13, and by means of Ineqs. [241] through [244] they formally identify the matching-key of each case, which is $(M > 0) \geq 1$. The ordering and match-keying will next be worked out for the cases of System No. 3 (Table 14) to illustrate the process. Readers can follow the same general process to confirm the correctness of the conjugate pairings in Systems No. 1, 2, and 4 of Table 14.

Referring to Table 13, Case I_{sub}, line 2, the M - and f -signets are

$$(M > 0), \text{ and } (f < 0); \text{ in addition, the corresponding nn-}$$

$$\text{metric is } (X_N < 0) > (f < 0).$$

$$\therefore -(X_N < 0) < -(f < 0)$$

$$\therefore |X_N| < |f|. *$$

\therefore By Ineq. [241], the ordering of $|X_N|$ and $|f|$ which has been found to inhere in Case I_{sub} identifies $(M > 0) > 1$ as its matching-key.

Also in Table 13, Case VI_{sub}, line 2, the M - and f -signets are

$$(M > 0), \text{ and } (f < 0); \text{ in addition, the corresponding nn-}$$

$$\text{metric is } -(Y_N > 0) < (f < 0).$$

$$\therefore (Y_N > 0) > -(f < 0)$$

$$\therefore |Y_N| > |f|. **$$

\therefore By Ineq. [242], the ordering of $|Y_N|$ and $|f|$ which has been found to inhere in Case VI_{sub} identifies the n.-metric $(M > 0) > 1$ as its matching-key. Since Case I_{sub} and Case VI_{sub} are found to have the

* $-(X_N < 0) = |X_N|$; $-(f < 0) = |f|$.

** $(Y_N > 0) = |Y_N|$; $-(f < 0) = |f|$.

Table 13—Relationships of fixed algebraic order between X_N , X , and f , all with fixed signs; also those between Y_N , Y , and f , all with fixed signs. Corresponding signs of M are indicated. All fixed signs are given in signet form and relationships of order in nn.-metric form (see footnote in Sec. 28).

Case Nos. and Descriptions	Applicable Inequalities and Signs of Corresponding Magnifications	Line Nos.	Ineq. Nos.
I. Signs of X_N and X Unlike. ($f = X_N - X$)	$(0 \leq X_N) \approx (X \leq 0)$; $(f \geq 0) \approx - (X \leq 0)$; $(M > 0)$; $(M \leq 0)$; $(M > 0)$; $(M \leq 0)$; $(M > 0)$; $(M \leq 0)$	line 1 line 2	[237]
II. Signs of X_N and X Alike; Both Negative. ($f = X_N - X$)	$(0 > X_N) \approx (X < 0)$; $(f \geq 0) < - (X < 0)$; $(M \leq 0)$	line 1 line 2	[238]a.
III. Signs of X_N and X Alike; Both Positive. ($f = X_N - X$)	$(0 < X_N) \approx (X > 0)$; $(f \geq 0) > - (X > 0)$; $(M \geq 0)$	line 1 line 2	[238]b.
IV. Signs of Y_N and Y Unlike. ($f = Y - Y_N$)	$(0 \approx Y_N) \approx (Y \approx 0)$; $(f \approx 0) \approx - (Y \approx 0)$; $(M > 0)$	line 1 line 2	[239]
V. Signs of Y_N and Y Alike; Both Negative. ($f = Y - Y_N$)	$(0 > Y_N) \approx (Y < 0)$; $(f \approx 0) > - (Y < 0)$; $(M \geq 0)$	line 1 line 2	[240]a.
VI. Signs of Y_N and Y Alike; Both Positive. ($f = Y - Y_N$)	$(0 < Y_N) \approx (Y > 0)$; $(f \approx 0) < - (Y > 0)$; $(M \leq 0)$	line 1 line 2	[240]b.

Note: 1. In considering solution or partial solution of a problem by use of any one among the six inequality groups (Case Nos.) of Table 13, either only the upper (sup) inequality symbols must be used, or only the lower (sub) ones. Single inequality symbols are always used as given.
 2. Should more than one inequality group (Case No.) be involved in considering a problem, the use of the sup or sub relationship must in each case be judged according to circumstance.
 3. See subsection III of Sec. 29, titled "Conjugate Pairing of the Inequalities of Table 13," for description of their use in Table 14.

Table 14—Systems of conjugate Newtonian inequalities and also their Gaussian counterparts, arranged according to the signs of f and M and displaying the applicable (fit) Newtonian and Gaussian conjugate distances. Case Nos. refer to Table 13, lines 2. Magnification ranges are explicitly indicated by fit n.-metrics, for all ($M > 0$). Such ranges are not required to be indicated for ($M < 0$).

System Nos.	Case Ident. Nos.	Newtonian nn.-metrics; or Conjugate Newtonian Inequalities	Gaussian nn.-metrics; or Conjugate Gaussian Inequalities	f-signets ($f \neq 0$)	M-signets With Fit n.-metrics ($M > 0$) ≥ 1
1	I ^{sup}	$(X_N > 0) < (f > 0);$	$-(X < 0) < (f > 0);$	$(f > 0)$	$(M > 0) > 1$
1	V ^{sup}	$-(Y_N < 0) > (f > 0).$	$(Y < 0) < (f > 0).$	$(f > 0)$	$(M > 0) > 1$
2	III ^{sup}	$(X_N > 0) > (f > 0);$	$-(X > 0) < (f > 0);$	$(f > 0)$	$(M > 0) < 1$
2	IV ^{sup}	$-(Y_N < 0) < (f > 0).$	$(Y > 0) < (f > 0).$	$(f > 0)$	$(M > 0) < 1$
3	I ^{sub}	$(X_N < 0) > (f < 0);$	$-(X > 0) > (f < 0);$	$(f < 0)$	$(M > 0) > 1$
3	VI ^{sub}	$-(Y_N > 0) < (f < 0).$	$(Y > 0) > (f < 0).$	$(f < 0)$	$(M > 0) > 1$
4	II ^{sub}	$(X_N < 0) < (f < 0);$	$-(X < 0) > (f < 0);$	$(f < 0)$	$(M > 0) < 1$
4	IV ^{sub}	$-(Y_N > 0) > (f < 0).$	$(Y < 0) > (f < 0).$	$(f < 0)$	$(M > 0) < 1$
5	II ^{sup}	$(X_N < 0) < (f > 0);$	$-(X < 0) > (f > 0);$	$(f > 0)$	$(M < 0)$
5	VI ^{sup}	$-(Y_N > 0) < (f > 0).$	$(Y > 0) > (f > 0).$	$(f > 0)$	$(M < 0)$
6	III ^{sub}	$(X_N > 0) > (f < 0);$	$-(X > 0) < (f < 0);$	$(f < 0)$	$(M < 0)$
6	V ^{sub}	$-(Y_N < 0) > (f < 0).$	$(Y < 0) < (f < 0).$	$(f < 0)$	$(M < 0)$

Note: 1. See also footnotes to Table 13; also see the graphical representations of Fig. 16.

2. Adjacent systems that are distinguished by no change in the signs of f and M , are separated by dotted lines. Adjacent systems distinguished by a change in the sign of f , but *not* of M , are separated by single solid lines. Adjacent systems distinguished by a change in the signs of *both* f and M , are separated by double solid lines.

3. In any inequality of Tables 13 and 14, the sign of any variable is *fixed* by the inequality symbol inside its parentheses. Such inequalities are called "signets," and they relate the variables to zero. The sign is *not* effectively changed by any later operation internal to any parentheses, that conforms to the rules of inequality algebra, providing the operation directly or indirectly involves an algebraic sign or inequality symbol which is initially outside those parentheses. See the footnote to Eq. [390], Appendix 8.

same matching-keys, their inequalities are properly paired as the conjugate inequalities of System No. 3, Table 14.

The mathematics of the pairing process and the resulting construction of Table 14 are based primarily on the Newtonian inequalities (nn.-metrics). Each such inequality has associated with it, in Table 13, a Gaussian inequality (nn.-metric) that is carried over with it to Table 14. The latter table, therefore, contains a column of six pairs of conjugate Newtonian inequalities, and a column of six pairs of corresponding conjugate Gaussian inequalities to make the table complete. In the interest of clarity, the Newtonian and Gaussian nn.-metrics are disassociated and shown separately, rather than compactly combined as in Table 13.

The organization of Table 14 makes it easy to trace the components of any system back to Table 13, should this be desired, and the tables are arranged on facing pages to simplify intercomparison.

Figure 16, which is a graphic representation of the six systems of Table 14, is described in detail under the next subheading. It must be remembered that each of the six systems of Table 14 and Fig. 16 represents *only one* of the combinations of fixed signs with limited ranges of numerical values that is possible to the six quantities X , Y , X_N , Y_N , f , and M , under the conditions of Gaussian imagery as defined by Eqs. [1] and [2], Part 1. The statement that is made, in effect, by the table and by the figure respecting *each* system is of the general form: "Under the conditions of Gaussian imagery, if f and M have the given fixed signs, and also if they have numerical values within the given or implied limits, then X , Y , X_N , and Y_N *must* have the indicated fixed signs, with the numerical value of each lying between the indicated or implied limits which may include zero or infinity." Any of the six quantities, and not merely f and M , may be chosen as the independent variables, to be assigned arbitrary fixed signs and numerical values or limits. Any combination of fixed signs and limited numerical ranges of the six quantities that does not fully conform to any one of the six systems of Table 14 and Fig. 16 is non-Gaussian and cannot represent any imaging system that consists of centered or coaxial spherical surfaces in air or vacuum. Thus, the "Excluded Cases" are defined in the broadest and most general terms possible (see Sec 22, Part 2).

It is instructive to note that the sign and limit differences between Systems No. 1 and 2 are dependent on the changes of M from the range $(M > 0) > 1$ to the range $(M > 0) < 1$. The same is true of the differences between Systems No. 3 and 4. In Systems No. 5 and 6 there are no sign and limit changes throughout the full range of M that is implied by $(M < 0)$.

IV. Graphic Representations of Systems No. 1 Through 6 (Table 14).

Figure 16 (a) through (f) diagrams Systems No. 1 through 6 of Table 14. For certain purposes it is easier to graphically visualize some of the relationships of the table by inspecting the figure than by directly consulting the table.

In each system of Fig. 16, the first and second principal points are respectively represented by H_1 and H_2 . This representation is only schematic, because the two principal points may have either order with respect to the direction of light travel and any finite separation (zero and negative values included) along axis c-c, depending upon system construction. These facts regarding order and

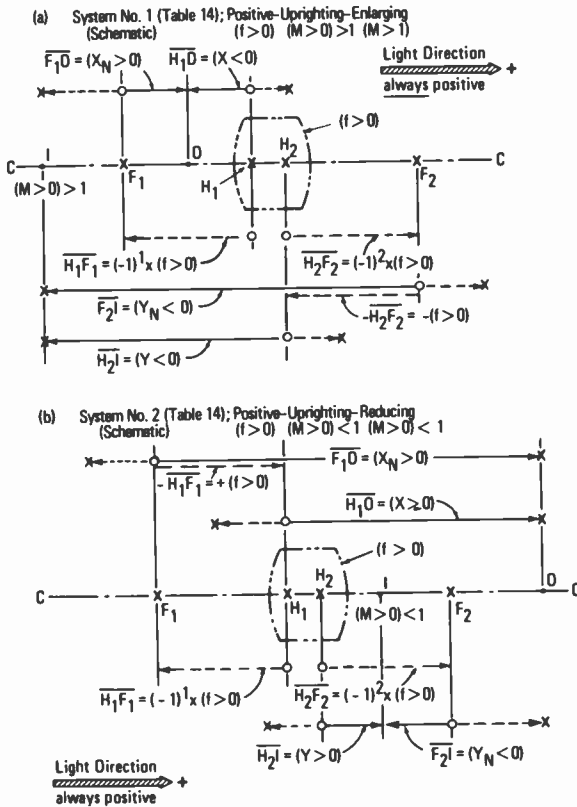


Fig. 16—Graphic representations of non-afocal Systems No. 1 through 6 (Table 14). See detailed description and explanation in text of Sec. 29, Subsection IV. Schematic only—not to scale.

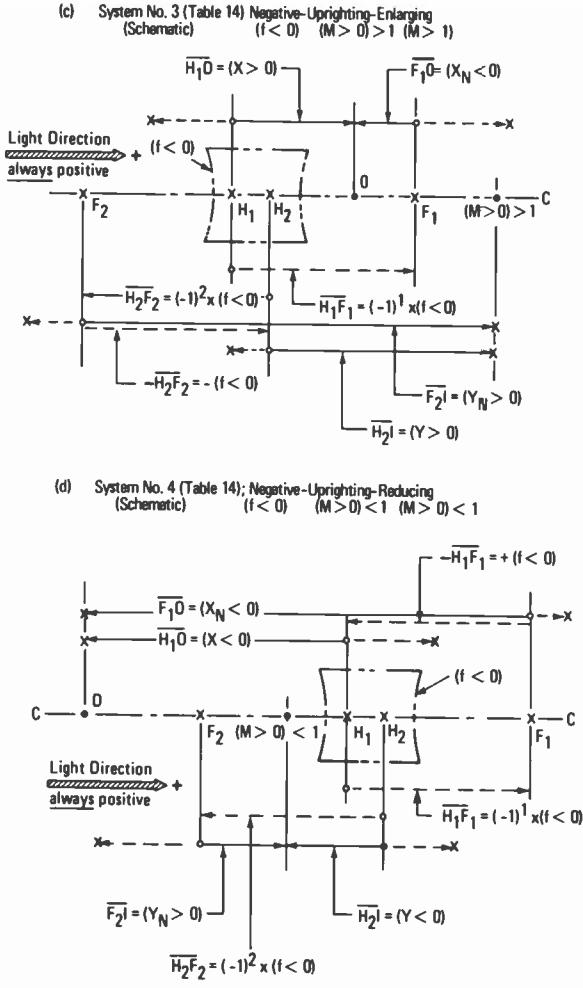


Fig. 16—Continued

separation of H_1 and H_2 are inherent in the character of Eq. [30] Part 1, for example.

The signed distance of the first principal focal point F_1 from H_1 as its point of origin, is $H_1F_1 = (-1)^1 (f \geq 0)$, and it depends on the sign of focal length f . Similarly, the signed distance of the second principal focal point F_2 from H_2 as its point of origin, is $H_2F_2 = (-1)^2 (f \geq 0)$.

Gaussian conjugate distances X (for object-point O) and Y (for

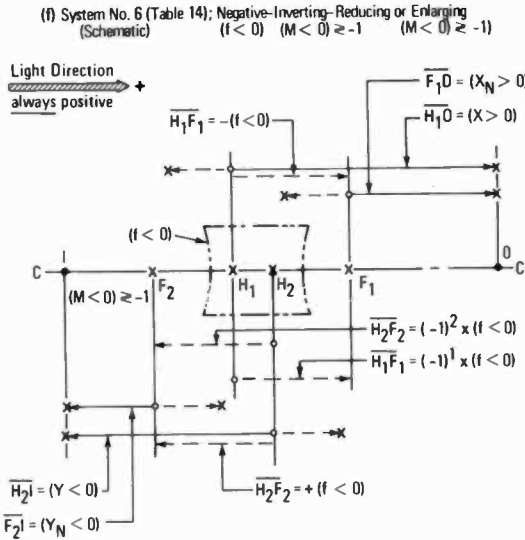
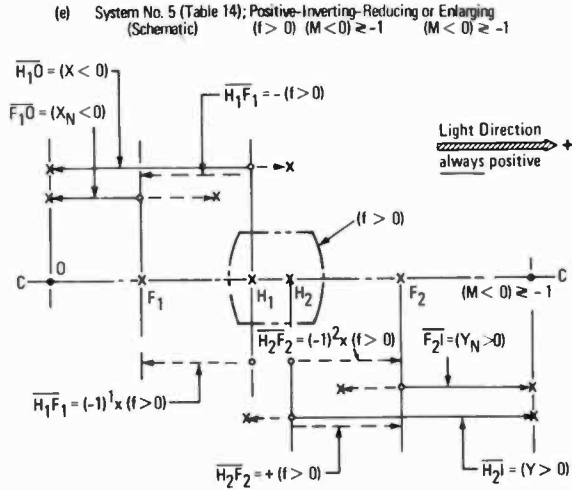


Fig. 16—Continued

image-point I), are measured from principal points H_1 and H_2 as their respective points of origin (or initial points). Newtonian conjugate distances X_N (for O) and Y_N (for I), are measured from F_1 and F_2 as their respective initial points.

Measurements from any arbitrary point of origin to any other point in the direction of light-travel represent positive distances. Measurements in the opposite direction represent negative dis-

tances. The dotted arrow distances $\overline{H_1F_1}$ and $\overline{H_2F_2}$ indicate the direction of F_1 from H_1 , etc., with respect to the light-travel direction, which is *always* positive. These statements fully conform to the Gardner sign convention of Part 1.

In each of the six systems of Fig. 16, *allowable* signed Newtonian and Gaussian object- and image-distances are represented by *solid* arrows. These are directed away from the planes of their above defined respective points of origin, which planes are indicated by open circles, and they are terminated in the planes of object O and image I. The positively directed arrows are clearly labeled ($X_N > 0$), ($Y > 0$), etc., and the negatively directed ones are labeled ($X_N < 0$), ($Y < 0$), etc., to indicate the signed Newtonian or Gaussian distances they represent.

Any *solid arrow* that terminates at a saltire (St. Andrew's Cross X) can be arbitrarily extended in its indicated direction without finite restriction (while of course carrying O or I with it).

Any *solid arrow* that represents a Newtonian conjugate distance X_N or Y_N , or a Gaussian conjugate distance X or Y , can be arbitrarily shortened without numerical restriction, *except* that the X_N -, Y_N -, X -, or Y -arrow may not be made shorter than any closely parallel, similarly directed dotted arrow that shares an initial point with it at F_1 or F_2 , or at H_1 or H_2 , and that is applicably dimensioned $(\pm)\overline{H_1F_1} = (\pm)(f \geq 0)$, or $(\pm)\overline{H_2F_2} = (\pm)(f \geq 0)$.* Where signs or directions of X and X_N or of Y and Y_N are opposed, shortening one arrow obviously requires lengthening the other.

Other "forbidden" locations for object- and image-points in *each* system of Fig. 16 are represented by *dotted* arrows whose freely possible extensions toward infinity are indicated by saltires at their terminal points which, of course, for the System No. in question *never* correspond to any actual (real or virtual) O or I. The logic of the prohibitions of such locations is that they represent a change or reversal of the sign of some associated distance X_N , Y , etc., whereas any distance (or for that matter, any other quantity) *in any one system* of Fig. 16 *can have only one fixed sign*. In other systems the fixed signs may be different.

In Fig. 16, the fixed signs (≥ 0) of the values of f and M that apply

* In these two equations, the parentheses that enclose the two \pm -symbols are intended to indicate that the signs are *not necessarily* associated in the conventional manner, i.e., with the upper signs of the two \pm -symbols *always* associated together, as well as with the upper one of the two inequality signs in the generalized signet ($f \geq 0$), etc. The use of the signs is entirely dependent on the circumstances that the two equations are intended to express, and *not necessarily* on any pre-existing convention of sign association.

to each system are clearly stated. All positive magnifications ($M > 0$) are designated as "uprighting," negative ones ($M < 0$) as "inverting," to indicate the orientation of the image with respect to the object. In every system where ($M > 0$) the magnification is given in the n.-metric form ($M > 0$) > 1 (or simply $M > 1$) or in the n.-metric form ($M > 0$) < 1 . The meaning of these forms was explained in the portion of this section of the text that appears under the subheading: "III. Conjugate Pairing of the Inequalities (nn.-metrics) of Table 13." Also, they respectively indicate "enlargement" and "reduction."

The apparent complexity of the figure is relieved somewhat by noting that:

- In Fig. 16, (a) & (b), the focal lengths of Systems No. 1 and 2 are both positive, and the magnifications are both positive.
- In Fig. 16, (c) & (d), the focal lengths of Systems No. 3 and 4 are both negative, and the magnifications are both positive.
- In Fig. 16, (e) & (f), the focal length of System No. 5 is positive but of No. 6 is negative, while magnifications are negative for both.

Phantom convex or concave outlines symbolize each physical optical system of Fig. 16, and visually identify its focal length as positive or negative, respectively.

Appendix 5—Development of Equations For The Primitive Non-Afocal Relay Optical System In Air or Vacuum, With One of Its Objects or One of Its Images At Infinity

This development will make frequent use of the replacement transformation of Sec. 6, Part 1. Since the equations to be transformed frequently involve the displacements $\Delta_c x$ and $\Delta_c y$, it is necessary to derive the replacements for these two quantities. We write from Eqs. [172] and [173],* Part 2,

$$\Delta_c x = x' - x \quad [337]$$

$$\Delta_c y = y' - y \quad [338]$$

By applying the replacement transformation of Sec. 6, Part 1, to the right sides of Eqs. [337] and [338] and noting the substitutions that

* Here, lower case x 's and y 's represent, respectively, object-distances measured from the first principal point of the anterior lens and image-distances measured from the second principal point of the posterior lens, of a system of two separated lenses that constitutes a primitive relay. $\Delta_c x = x' - x$; $\Delta_c y = y' - y$.

these equations permit, we easily arrive at the following transformation replacements for $\Delta_c x$ and $\Delta_c y$.

1. Replace $\Delta_c x$ by the replacement for its equivalent $x' - x$, which is
 $-y' - (-y) = -y' + y = -\Delta_c y$, which is the replacement for $\Delta_c x$.
2. Replace $\Delta_c y$ by the replacement for its equivalent $y' - y$, which is
 $-x' - (-x) = -x' + x = -\Delta_c x$, which is the replacement for $\Delta_c y$.

Table 3 of Part 1 should be extended by, in effect, incorporating these two statements as items 22 and 23.

For Case 1, Table 11, the development proceeds as follows: From Eq. [180], Part 2,

$$a = \frac{M(x' - \Delta_c x)(y + MM'\Delta_c x) - M'x'y}{MM'\Delta_c x} \quad [339]$$

By substituting $\Delta_c x = \Delta_c y/MM'$, from Eq. [175], and $MM'\Delta_c x = \Delta_c y$, from Eq. [166], both of Part 2,

$$a = \frac{M\left(x' - \frac{\Delta_c y}{MM'}\right)(y + \Delta_c y) - M'x'y}{\Delta_c y}$$

which reduces to

$$a = \frac{\frac{1}{M'}(MM'x' - \Delta_c y)(y + \Delta_c y) - M'x'y}{\Delta_c y} \quad [340]$$

in which, for a to be finite or zero, M' and $\Delta_c y$ are severally and arbitrarily finite but never zero, while M , x' , and y are severally and arbitrarily finite or zero. Thus, when $x = \infty$ and $M = 0$, as in Table 11

$$a = -\frac{1}{M'}(y + \Delta_c y) - \frac{1}{\Delta_c y}M'x'y \quad (x = \infty, \Delta_c x = \infty, M = 0) \quad [341]$$

in which, except that M no longer appears explicitly, the conditions that apply to Eq. [340] in order for a to be finite or zero remain unchanged. Usually, a is required to be positive.

For Case 2, Table 11, the development may proceed by either of two methods.

Method A: By using a combination of the replacement transformation and algebraic substitutions

On applying the replacement transformation to both sides of Eq. [340],

$$a = \frac{M' \left(\frac{-y'}{MM'} + \Delta_c x \right) (-x - \Delta_c x) - \frac{xy'}{M'}}{-\Delta_c x} \quad [342]$$

By then substituting $y' = y + \Delta_c y = y + MM' \Delta_c x$ (see Eqs. [173] and [166]) and also by substituting $-x - \Delta_c x = -x'$ from Eq. [172],

$$a = \frac{-M' x' \left(\frac{-y - MM' \Delta_c x}{MM'} + \Delta_c x \right) - \frac{x(y + MM' \Delta_c x)}{M'}}{-\Delta_c x}$$

which reduces to

$$a = \frac{y}{\Delta_c x} \left(\frac{x}{M'} - \frac{x'}{M} \right) + Mx \quad [343]$$

in which, for a to be finite or zero, M' is arbitrary but never zero, M and $\Delta_c x$ are severally and arbitrarily finite but never zero, while x , x' , and y are severally and arbitrarily finite or zero. Note that the finiteness of x and x' assures that of $\Delta_c x$ (see Eq. [337]). Thus, when $y' = \infty$ and $M' = \infty$, as in Table 11,

$$a = \frac{-x'y}{M\Delta_c x} + Mx \quad (y' = \infty, \Delta_c y = \infty, M' = \infty) \quad [344]$$

in which, except that M' no longer appears explicitly, the conditions that apply to Eq. [343] in order for a to be finite or zero remain unchanged. Usually, a is required to be positive.

Method B: By using algebraic substitutions *only*

According to Eq. [178], Part 2

$$a = \frac{Mxy' - M'x'y}{y' - y} \quad [345]$$

from which, by dividing numerator and denominator by MM' and substituting $\Delta_c y = y' - y$ from Eq. [173] and substituting $\Delta_c y/MM' = \Delta_c x$ from Eq. [175],

$$a = \frac{\frac{xy'}{M'} - \frac{x'y}{M}}{\Delta_c x}$$

and, since $y' = y + \Delta_c y$ from Eq. [173],

$$a = \frac{\frac{x(y + \Delta_c y)}{M'} - \frac{x'y}{M}}{\Delta_c x}$$

or

$$a = \frac{\frac{xy}{M'} + \frac{x\Delta_c y}{M'} - \frac{x'y}{M}}{\Delta_c x}$$

On again substituting $\Delta_c y = MM'\Delta_c x$ from Eq. [166] and reducing

$$a = \frac{y}{\Delta_c x} \left(\frac{x}{M'} - \frac{x'}{M} \right) + Mx. \quad [346]$$

Equations [343] and [346] are obviously identical. *Q.E.D.*

Method B serves to confirm Eq. [340], and also the replacement transformation of it in deriving Eq. [343] by Method A.

For Case 3, Table 11, the development proceeds as follows: By applying the replacement transformation to both sides of Eq. [343] (or Eq. [346])

$$a = \frac{x}{\Delta_c y} (-M'y + My') - \frac{y}{M} \quad [347]$$

in which, for a to be finite or zero, M and $\Delta_c y$ are severally and arbitrarily finite but never zero, while M' , x , y , and y' are severally and arbitrarily finite or zero. Note that the finiteness of y and y' assures that of $\Delta_c y$ (see Eq. [338]). Thus, when $x' = \infty$ and $M' = 0$, as in Table 11,

$$a = \frac{Mxy'}{\Delta_c y} - \frac{y}{M} \quad (x' = \infty, \Delta_c x = \infty, M' = 0) \quad [348]$$

in which, except that M' no longer appears explicitly, the conditions that apply to Eq. [347], in order for a to be finite or zero, remain unchanged. Usually, a is required to be positive.

For Case 4, Table 11, the development proceeds as follows: By slightly restating Eq. [342], which was the direct result of the replacement transformation of Eq. [340],

$$a = \frac{M'}{\Delta_c x} \left(\frac{-y'}{MM'} + \Delta_c x \right) (x + \Delta_c x) + \frac{xy'}{M'\Delta_c x} \quad [349]$$

in which, for a to be finite or zero, M is arbitrary but never zero, M' and $\Delta_c x$ are severally and arbitrarily finite but never zero, while x and y' are severally and arbitrarily finite or zero. Thus, when $y = \infty$ and $M = \infty$, as in Table 11,

$$a = M'(x + \Delta_c x) + \frac{xy'}{M'\Delta_c x} \quad (y = \infty, \Delta_c y = \infty, M = \infty) \quad [350]$$

in which, except that M no longer appears explicitly, the conditions that apply to Eq. [349] in order for a to be finite or zero, remain unchanged. Usually, a is required to be positive.

Among the foregoing expressions for a , Eqs. [340] and [349] are replacement transformations of each other. The same is true of Eqs. [341] and [350], also of Eqs. [343] and [347], and also of Eqs. [344] and [348]. These relationships are easily verified by the reader.

Appendix 6—Analysis of The Primitive Afocal Relay Optical System In Air or Vacuum, With One of Its Objects and Also The Image of That Object At Infinity

By Eq. [112], Part 2, the magnification of a primitive relay for an object at general distance x is

$$M = \frac{ff'}{(f + f' - a)x + f(f' - a)} \quad (\text{see also Eq. [13], Part 1}) \quad [351]$$

the solution of which for x is

$$x = \frac{f[f' - M(f' - a)]}{M(f + f' - a)} \quad (\text{see also Eq. [31]}) \quad [352]$$

The replacement transformation of Eq. [351] is

$$\frac{1}{M} = \frac{ff'}{-(f + f' - a)y + f'(f - a)} \quad [353]$$

the solution of which for y is (as also by direct replacement transformation of Eq. [352]),

$$y = \frac{f'(f - a - Mf)}{f + f' - a} \quad [354]$$

If $-\infty < [(f \text{ and } f') \neq 0] < +\infty$, and if $-\infty < (M \neq 0) < +\infty$, and if also $-\infty < a < +\infty$, then the only condition that will cause $x = y = \infty$ in Eqs. [352] and [354] is

$$f + f' - a = 0. \quad [355]$$

By Eqs. [45] and [113], Parts 1 and 2, this is also the condition that makes the primitive relay afocal or its focal length F infinite. By Eq. [351] it makes the magnification have a constant or absolute value $M = M_A = -f'/f$, which is independent of x .

When x becomes infinite, the resulting magnification of the system is not obvious from Eq. [351]. By Eq. [17], the expression for the magnification of a primitive relay may be written in terms of the distance D of the image from the object, and also in terms of the focal length f of the anterior lens, as

$$M = \frac{f(D - s - s' + x - a)}{f(x - a) - ax} \quad [356]$$

From Eq. [19], Part 1, substitution may be made for the coefficient of f in the numerator of Eq. [356], as follows

$$D - s - s' + x - a = \frac{f'[(f - a)x - fa]}{(f + f' - a)x + f(f' - a)} \quad [357]$$

When this substitution is made and a is removed by the substitution of $a = f + f'$ from Eq. [355], in order to introduce the afocal condition, Eq. [356] reduces to

$$M = \frac{ff'[f'x + f(f + f')]}{f^2[-f'x - f(f + f')]} \quad [358]$$

and by canceling the common factor in numerator and denominator, $M = -f'/f$, as in Eq. [216].

If the common factor in Eq. [358] is not canceled, then if $x = \infty$ the expression for M is indeterminate. But by L'Hospital's rule

$$M = \frac{ff' \left(f' \frac{dx}{dx} \right)}{-f^2 \left(f' \frac{dx}{dx} \right)}$$

and the indeterminate form, when $x = \infty$, is evaluated as

$$M = \frac{-f'}{f} = M_A = \text{constant} \quad [359]$$

just as for any finite value of x .

It is necessary to determine the location of the image of an infinitely distant object when the optical system is an afocal primitive

relay. We start with Eqs. [11] and [12], Part 1, which respectively state that

$$D - s - s' = \frac{-Mxa - (1 - M)(x - a)f}{f} \quad [360]$$

and

$$D - s - s' = \frac{x[a - (1 - M)f'] - a^2}{f' - a} \quad [361]$$

The left sides of these two equations are invariant under the replacement transformation, which fact allows us to equate the right side of Eq. [360] to the transformed right side of Eq. [361]. Thus

$$\frac{Mxa + (1 - M)(x - a)f}{f} = \frac{y[a - (1 - 1/M)f] + a^2}{f - a} \quad [362]$$

Solution of Eq. [362] for y involves extensive algebraical reductions, the essential steps of which are all indicated as follows:

$$\begin{aligned} 1. \text{ From Eq. [362], } & fy[Ma + f(1 - M)] + Mfa^2 \\ & = M^2xa(f - a) + Mf(1 - M)(x - a)(f - a) \end{aligned}$$

The afocal condition is *partially* introduced by substituting $a = f + f'$ (it is convenient to keep M explicit), after which the solution process continues as follows:

$$\begin{aligned} 2. & fy[M(f + f') + f(1 - M)] + Mf(f + f')^2 \\ & = M^2x(f + f')(f - f - f') + Mf(1 - M)(x - f - f') \\ & \quad (f - f - f') \\ 3. & fy[M(f + f') + f(1 - M)] + Mf(f + f')^2 \\ & = -M^2f'x(f + f') - Mxf'f(1 - M) + Mf'f(f + f')(1 - M) \\ 4. & fy[M(f + f') + f(1 - M)] \\ & = -Mf'x[M(f + f') + f(1 - M)] \\ & \quad + Mf(f + f')[f'(1 - M) - (f + f')] \\ & \quad - Mf'x[M(f + f') + f(1 - M)] \\ 5. & y = \frac{-Mf'x[M(f + f') + f(1 - M)]}{f[M(f + f') + f(1 - M)]} - \frac{Mf(f + f')(Mf' + f)}{f[M(f + f') + f(1 - M)]} \\ 6. & y = -M \left[\frac{f'}{f} x + (f + f') \right] \quad (f + f' = a, M = -f'/f) \quad [363] \end{aligned}$$

Equation [363] determines y for *any* x , finite or infinite.

Up to this point, the discussion has been in terms of the linear, transverse Gaussian magnification M . When the primitive relay system, in its afocal form, is employed as a telescope to view an

object at a finite distance, it is necessary to define the angular or telescopic magnification M_T and to derive its relation to the transverse magnification M . The derivation is illustrated by Fig. 14, above.

If a *small* object at distance x from the first principal point of the anterior lens of an afocal relay has a height h , it is imaged at distance y from the second principal point of the posterior lens and at image-height h' . The linear, transverse Gaussian magnification is

$$M = \frac{h'}{h} = M_A = \frac{-f'}{f} = \text{constant} \quad (\text{see Eq. [359]}). \quad [364]$$

The object subtends the angle $\theta = (h/x)$ at the anterior lens, and the image subtends the angle $\theta' = (h'/y)$ at the posterior lens. The telescopic magnification M_T may be defined as

$$M_T = \frac{\theta'}{\theta} = \frac{h'x}{hy} = \frac{Mx}{y} = M_A \left(\frac{x}{y} \right) = \frac{-f'x}{fy}. \quad [365]$$

In the afocal primitive relay, used as a telescope, $M = M_A = \text{constant}$, while x and y are variables that are related by Eq. [363]. It is of interest to relate M_T to M_A when x and y are infinite, for then Eq. [365] is indeterminate. On substituting into Eq. [365] from Eq. [363], solution for M_T gives

$$M_T = \frac{M_A x}{-M_A \left[\frac{f'}{f} x + f + f' \right]} \quad \begin{array}{l} (x = \text{finite}) \\ (M_A = -f'/f) \end{array} \quad [366]$$

from which, by applying L'Hospital's rule and making a suitable substitution from Eq. [359]

$$\lim_{x \rightarrow -\infty} M_T = \frac{M_A}{-M_A \frac{f'}{f}} = \frac{1}{M_A} \quad (x = \infty). \quad [367]$$

Equation [367] may be obtained more directly, by allowing $x = \infty$ in Eq. [363], then substituting the resulting *literal* expression $y = -Mf'x/f$ for y directly into Eq. [365] and reducing. The useful relationship of Eq. [366], for finite values of x , will then of course not appear, but the need to apply L'Hospital's rule will be avoided.

Equation [367] implies that if $|\theta'| > |\theta|$ so that angular telescopic magnification $|M_T| = (|\theta'|/|\theta|) > 1$, as would be the case in a useful Keplerian telescope (in lunar observation, for example), then $|h'| < |h|$ in order that linear magnification $|M_A| = (|h'|/|h|) < 1$! This may appear contrary to intuitive expectation.

By Eq. [363], y becomes infinite when x becomes infinite, but if $|h'| < |h|$ whereas $|\theta'| > |\theta|$, the implication is that the linear image at infinite distance y , in addition to being smaller, must be very much "closer" to the telescope than the linear object at infinite distance x .

This implication can be practically understood, in terms of very great finite (but practically infinite) object-distances, such as the lunar object-distance of roughly $x = -10^9$ ft.

If, in the afocal telescope, $f = 10$ in. and $f' = 1$ in., then linear magnification $M = M_A = -f'/f = -1/10 = -0.10$. Therefore, by Eq. [363]

$$y = -M \frac{f'}{f} x = (0.10)(0.10)(-10^9) = -10^7 \text{ ft,}$$

or only 1% of x !

Now let $h = 1$ ft. Then $h' = M_A h = (-0.10)(1) = -0.10$ ft. But $\theta = h/x = 1/-10^9$ rad. and $\theta' = h'/y = -0.10/-10^7 = 10^{-8}$ rad.; and angular magnification $M_T = \theta'/\theta = (10^{-8})(-10^9) = -10$. The linear magnification, on the other hand, is $M_A = -f'/f = -1/10 = -0.10$; and by Eq. [367]

$$M_T = \frac{1}{M_A} = 1/-0.10 = -10$$

which agrees with the value of M_T calculated in the earlier part of this paragraph.

This agreement demonstrates that the foregoing interpretation of the implications of Eq. [367] is correct. Any intuitive difficulty in accepting these implications involves not only the infinite distances from the telescope, of the object and image, but also the infinite distances from the telescope of the two principal points of any afocal system of two separated lenses (see Eqs. [32] and [33]). Readers may wish to give further study to the mathematical implications of the quadruple infinities that are encountered with this type of telescope.

Appendix 7—Relationships That Are Basic to The Analysis of The Regular and Inverse Relaying Actions of Any Non-Afocal, Centered Spherical Lens or Lens System In Air or Vacuum

This discussion is not restricted to the primitive relay, but applies to the imagery at finite magnification $M (\neq 0)$ of any object-point O , or to the similar imagery at magnifications M and M' of any two

object-points O and O' that are spaced a finite distance apart along the axis of any lens or optical system of finite focal length $f \neq 0$.

From V-2 and V-5 in Table 1, Part 1,

$$M = \frac{f}{f + X}, \text{ and } M' = \frac{f}{f + X'} \quad [368]$$

and also

$$M = \frac{f - Y}{f}, \text{ and } M' = \frac{f - Y'}{f} \quad [369]$$

We are interested in the relation of $X, Y, X',$ and Y' to $\pm\infty \neq f \geq 0$ for each of its combinations with $\pm\infty \neq M \geq 0$ and $\pm\infty \neq M' \geq 0$. There are eight combinations in all.

By eliminating M between Eqs. [368] and [369]

$$X + f = \frac{-f^2}{Y - f} \quad [370]$$

where X and Y are Gaussian conjugate distances, measured respectively from the first and second principal points of the lens or system. The discussion beyond this point is greatly simplified and clarified by expressing the relationships in terms of the corresponding Newtonian conjugate distances X_N and Y_N , which are defined, from Eq. [370], as

$$X_N = X + f \quad [371]$$

and

$$Y_N = Y - f \quad [372]$$

(See Eqs. [233] and [235] and Fig. 15) in accordance with the Gardner sign convention. X_N and Y_N are measured respectively from the first** and second† principal focal points of the lens or

* See footnote to Sec. 27, p. 128 regarding the upper case $X, Y, X',$ and Y' .

**The first principal focal point of a lens or system of finite local length f in air or vacuum, which is the principal focal point in the object space, is that axial object-point, whether real or virtual, that is imaged by the system as a real image at positive infinity or a virtual image at negative infinity. It is *always* distant $(-1)^1 f$ from the first principal point (see NOTE below).

† The second principal focal point of a lens or system of finite focal length f in air or vacuum, which is the principal focal point in the image space, is that axial image-point at which a real object-point at negative infinity, or a virtual object-point at positive infinity, is brought to a real or virtual focus by the system. It is *always* distant $(-1)^2 f$ from the second principal point (see NOTE below).

NOTE: Both of the preceding principal focal point definitions are just as applicable when f is negative as when it is positive.

system. They are positive when the measures are in the direction of the light travel; otherwise they are negative. This is in agreement with the Gardner sign convention. Thus, Eq. [370] may be re-expressed as

$$X_N Y_N = -f^2 \quad [373]$$

which is commonly known as the Newtonian form of the simple lens equation.* Its statement here is in conformity with the Gardner sign convention. Equation [373] immediately reveals that $X_N \neq 0$ and $Y_N \neq 0$ are *always* of unlike sign.

From Eqs. [368] and [369] we may now write

$$M = \frac{f}{X_N} = \frac{-Y_N}{f} \quad [374]$$

which shows that for any arbitrarily assigned algebraic value of X_N or of Y_N the sign of the magnification depends on the sign of the focal length.

Equations [371] through [374] are made to apply to object-point O' and to image-point I' by merely priming X , Y , X_N , Y_N , and M while keeping f plain. By accordingly substituting into Eq. [232] from Eq. [374], we have

$$\frac{\Delta_c y}{\Delta_c x} = MM' = M_\Delta = \frac{f^2}{X_N X'_N} = \frac{Y_N Y'_N}{f^2}. \quad [375]$$

Eq. [375] shows the sign of M_Δ to be independent of the sign of f when X_N and X'_N or Y_N and Y'_N are given.

By substituting into Eq. [375] the value of f^2 from Eq. [373], we obtain

$$MM' = M_\Delta = \frac{-Y_N}{X'_N} = \frac{-Y'_N}{X_N}. \quad [376]$$

Simple addition of Eqs. [371] and [372] produces

$$X_N + Y_N = X + Y \quad [377]$$

showing that the sum of the Newtonian conjugate distances is *always* equal to the sum of the Gaussian conjugates, providing the Gardner sign convention is strictly observed.

* By substituting $X_N = X + f$, and $Y_N = Y - f$ into Eq. [373], the equation reduces to the form $xy/(x - y) = f$, which is the Gaussian expression for focal length f of Table 1 (II-1), Part 1. Thus, an expression or system of expressions that is consistent with Eq. [373] is also consistent with Eq. [1], Part 1.

Focal length is easily calculated from X_N and X , or from Y_N and Y , as is clear from Eqs. [371] and [372]. Its calculation from X_N and Y or from Y_N and X is also of interest. By Eqs. [372] and [373]

$$Y_N = Y - f \quad [378]$$

and

$$X_N Y_N = -f^2 \quad [379]$$

from which, by elimination of Y_N ,

$$f^2 - X_N f + X_N Y = 0$$

or

$$f = \frac{X_N}{2} \pm \sqrt{\frac{X_N^2}{4} - X_N Y} \quad (X_N \neq 0)^* \quad [380]$$

Thus it is seen, that focal length f has real, non-zero values providing only that

$$X_N^2 \geq 4X_N Y \quad (X_N \geq 0, f \text{ real}). \quad [381]$$

No physical optical system can exist for, or be defined by, values of X_N and Y that do not satisfy Ineq. [381]. When $X_N > 0$, the condition for real values of f simplifies to

$$X_N \geq 4Y \quad \left(\text{or } Y \leq \frac{X_N}{4} \right) \quad (X_N > 0, f \text{ real}). \quad [382]$$

On the other hand, when $X_N < 0$, we first restate Ineq. [381] as

$$-X_N^2 \leq -4X_N Y$$

and then on dividing by $-X_N$, which is positive, the condition for real values of f simplifies to

$$X_N \leq 4Y \quad \left(\text{or } Y \geq \frac{X_N}{4} \right) \quad (X_N < 0, f \text{ real}). \quad [383]$$

When Y_N and X are the independent variables, a similar procedure shows that the focal length becomes

* In Eq. [380], the value $f = 0$ will result if $X_N = 0$, regardless of the numerical value assigned to Y . However, by Eq. [371], $f = -X$ whenever $X_N = 0$. This shows f to be arbitrary in such a case and not necessarily zero. In fact, no physical lens or optical system can have a "zero" focal length (see the final paragraphs of this appendix).

$$f = -\frac{Y_N}{2} \pm \sqrt{\frac{Y_N^2}{4} - Y_N X} \quad (Y_N \neq 0) \quad [384]$$

while the conditions for real f become

$$Y_N^2 \geq 4Y_N X \quad (Y_N \geq 0, f \text{ real}) \quad [385]$$

or, when $Y_N > 0$, the simplified condition

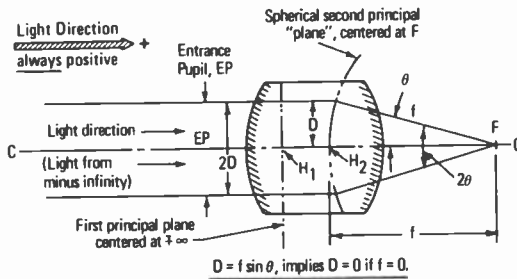
$$Y_N \geq 4X \quad \left(\text{or } X \leq \frac{Y_N}{4}\right) \quad (Y_N > 0, f \text{ real}) \quad [386]$$

or, when $Y_N < 0$, the simplified condition

$$Y_N \leq 4X \quad \left(\text{or } X \geq \frac{Y_N}{4}\right) \quad (Y_N < 0, f \text{ real}). \quad [387]$$

It is easily demonstrated (see Fig. 21)* that no physical lens or optical system can have a "zero" focal length. Let the entrance pupil (EP) diameter of any optical system be $2D$ and the system focal length be f . Let the *angular* exit pupil diameter, measured at the second principal focal point F (see footnote, p. 158), be 2θ . It is well known in the literature of optical systems that if the system is corrected for coma (pupillary zonal variation of focal length) and for spherical aberration (pupillary zonal variation of the axial position

* Figures 17, 18, 19, and 20 are in Part 3, Section B, as yet unpublished.



NOTE: In aplanatic systems generally, the first principal "plane" is spherical and centered at the axial object-point; the second principal "plane" is also spherical and centered at the axial image-point. They do intersect the axis at the Gaussian principal points, H_1 and H_2 , and the axial object- and image-points are Gaussian.

Fig. 21—Schematic diagram to illustrate proof of the photometric impossibility of an optical system having a zero focal length. Not to scale.

of the second focal point), the system is aplanatic and the following relationship applies:

$$\frac{D}{f} = \sin \theta \quad (0 \leq \sin \theta \leq 1)$$

$$\therefore D = f \sin \theta$$

Thus, a "zero" focal length dictates a zero entrance pupil diameter, and *no light* can pass through such an optical system. This is the meaning of the statements, in Secs. 9 and 12: Examples 4 and 5, Part 1, that "for photometric reasons, no physical lens or optical system can have a "zero" focal length."

The relationships that have led to the conclusion of the preceding paragraph are among those of optical system photometry, and are best appreciated by consulting references 23–28, in Part 2 of this paper.

Appendix 8—Derivation of Relationships of Algebraic Order Between Fixedly Signed Object-Distances and Focal Lengths, and Also Between Fixedly Signed Image-Distances and Focal Lengths

I. Since X in Ineq. [234] may have either sign, the full dependence of the sign of f on the condition of *unlike* signs for X_N and X is expressible as

$$f \geq 0 \text{ corresponds to } X_N \geq 0 \geq X \quad (\text{signs of } X_N \text{ and } X \text{ opposed}) \quad [388]$$

or, to make the relationship of order between X_N and X more explicit, the correspondence is expressed in the better form of Ineq. [234], as

$$(0 \leq X_N) \geq (X \leq 0); (f \geq 0). * \quad (\text{Used in Case I line 1, Table 13}) \quad [389]$$

The condition of *like* signs for X_N and X , and also for Y_N and Y , is a little more involved and will be discussed separately in Section II, below; in such cases the signets** in X_N and X , etc. *must* each have a single inequality symbol.

* This compactly expresses two groups of four inequalities each; one group employs *only* the upper inequality symbols of Ineq. [389], and the other only the lower. The same practice appears throughout this appendix. Wherever a single inequality symbol appears, it is *always* used as given. (See the discussion of Sec. 29, Subsec I, and footnote 1 of Table 13).

** Footnote to Sec. 28, p. 136, defines and describes the terms "signet" and "metric."

By substitutions of the signed quantities in Ineq. [388] or in Ineq. [389] into Eq. [233]

$$(f \geq 0) = (X_N \geq 0) - (X \leq 0), \dagger \quad [390]$$

for oppositely signed X_N and X ,

where signets $(X_N \geq 0)$, $(X \leq 0)$, and $(f \geq 0)$ are corresponding, inherently signed entities that *must* retain their precise internal structure or its equivalent,† including their delimiting parentheses, as the work continues. The essential internal structures of these entities are unaffected by any algebraic operations that are correctly performed upon them.† By transposing the entity $(X \leq 0)$, Eq. [390] yields the equation, for *oppositely signed* X_N and X ,

$$(X_N \geq 0) = [(X \leq 0) + (f \geq 0)] \geq 0, *$$

from the right side of which we obtain the Gaussian inequality

$$(f \geq 0) \geq - (X \leq 0). ** \quad \bullet \quad \text{(Used in Case I line 2, Table 13)} \quad [391]$$

Eq. [390] similarly yields, on further transposition

$$(X \leq 0) = [(X_N \geq 0) - (f \geq 0)] \leq 0, * \quad [392]$$

from the right side of which we obtain the Newtonian inequality

$$(f \geq 0) \geq (X_N \geq 0). ** \quad \text{(Used in Case I line 2, Table 13)} \quad [393]$$

II. The condition of *like* signs for X_N and X requires two inequalities, similar in form to Ineq. [389] for its expression. These are (see Ineqs. [234] and [388]) for X_N and X *both negative*

† By the conventions of the algebra of inequalities, $(X \leq 0)$ is the full equivalent of $(0 \geq X)$. Another rule of equivalence, for example, is that $-(X \leq 0)$ is the full equivalent of $+(-X \geq 0)$; it may sometimes be used to advantage. For example, $(X_N \geq 0) - (X \leq 0) = (-X \geq 0) - (-X_N \leq 0)$, should such a restatement be useful. Note carefully that in this type of transformation, any definitely indicated initial or true sign of any variable remains fixed or unchanged (see footnotes to Table 14, and footnote to Eq. [234]). In other words, no signet relationship is changed by such transformations.

* Both sides of an equation *must* be ≥ 0 , or else they *must* be ≤ 0 .

** Readers unaccustomed to algebraic operations with inequalities should consult mathematics textbooks or references for the simple rules that apply.

$$(0 > X_N) \geq (X < 0); (f \geq 0), \dagger \quad \begin{array}{l} \text{(Used in Case II} \\ \text{line 1, Table 13)} \end{array} \quad [394]$$

and for X_N and X both positive

$$(0 < X_N) \geq (X > 0); (f \geq 0), \dagger \quad \begin{array}{l} \text{(Used in Case III} \\ \text{line 1 Table 13)} \end{array} \quad [395]$$

Beginning with Eq. [233] and Ineq. [394] the development exactly parallels that which produced the relationships of Eq. [390] through Ineq. [393], and it yields the Newtonian inequality (for X_N and X both negative)

$$(f \geq 0) > (X_N < 0) \quad \begin{array}{l} \text{(Used in Case II} \\ \text{line 2, Table 13)} \end{array} \quad [396]$$

and also the Gaussian inequality (for X_N and X both negative)

$$(f \geq 0) < -(X < 0). \quad \begin{array}{l} \text{(Used in Case II} \\ \text{line 2, Table 13)} \end{array} \quad [397]$$

The inequalities that are derived in the same manner from Ineq. [395], for the case of X_N and X both positive, are the Newtonian inequality

$$(f \geq 0) < (X_N > 0) \quad \begin{array}{l} \text{(Used in Case III} \\ \text{line 2, Table 13)} \end{array} \quad [398]$$

and the Gaussian inequality

$$(f \geq 0) > -(X > 0) \quad \begin{array}{l} \text{(Used in Case III} \\ \text{line 2, Table 13)} \end{array} \quad [399]$$

A closely similar procedure that stems from Eq. [235] and Ineq. [236] is followed in deriving the Newtonian and Gaussian inequalities of Table 13 in Y_N and Y , respectively. Details are left to the reader.

† Ineqs. [394] and [395], like Ineq. [234], are more easily comprehended in the light of Eq. [233] if X_N and X are not expressed in signet form, although use of that form introduces no material difference.

Patents Issued to RCA Inventors—Fourth Quarter 1983

October

- A. E. Bell** Reinforced Bubble Recording Medium and Information Record (4,408,213)
- G. N. Butterwick** Method for Processing a Lithium-Sodium-Antimony Photocathode (4,407,857)
- A. W. Buzgo** Spacer for Use in Testing Information Recorded Discs (4,408,320)
- T. L. Chase and G. M. Ehemann, Jr.** Photographic Method for Printing a Viewing-Screen Structure Using a Light-Transmission Filter (4,408,851)
- D. Chin and R. J. Maturo** Tuning Display for a Television Receiver (4,410,913)
- R. J. D'Amato** Electrode for an Electron Gun (4,409,513)
- P. Datta and E. S. Pollniak** High Density Information Disc Lubricants (4,410,748)
- J. M. Ferguson, T. Y. Chen, and W. G. Gibson** Video Disc Player Having Vertical Timing Signal Generator (4,409,626)
- R. E. Flory** Simplified Transmission System for Sequential Time-Compression of Two Signals (4,410,981)
- S. M. Fox** Attitude Control System for Spacecraft Utilizing the Thruster Plume (4,407,469)
- J. C. Halbrook** Degassing a CRT With Modified RF Heating of the Mount Assembly Thereof (4,410,310)
- J. R. Hale** Glass Support Rod for Use in Electron-Gun Mount Assemblies (4,409,279)
- J. R. Harford** Noise Sensitivity Reduction Apparatus for a TV Receiver AGC System (4,408,229)
- R. W. Klipp and H. C. Johnson** Frequency Synthesizer With Learning Circuit (4,410,860)
- H. P. Kleinknecht, W. E. Ham, and H. Meier** Optical Measurements of Fine Line Parameters in Integrated Circuit Processes (4,408,884)
- W. F. Kosonocky** Charge Transfer Circuits With Dark Current Compensation (4,412,343)
- F. B. Lang** Television Receiver High Voltage Protection Circuit (4,412,254)
- P. A. Levine** Apparatus for Processing CCD Output Signals (4,412,190)
- J. Maa** Etching of Tantalum Silicide/Doped Polysilicon Structures (4,411,734)
- L. W. Martinson** Digital Dual Half Word or Single Word Position Scaler (4,411,009)
- G. N. Mehrotra and G. Vanarsdall** Video Disc Player Having Stylus Cleaning Apparatus (4,408,315)
- M. W. Muterspaugh and G. A. Whittedge** Impedance Transformation Network for a SAW Filter (4,410,864)
- E. J. Nossen** Digital Phase Demodulation and Correlation (4,412,302)
- J. A. Olmstead** Operational Amplifier With Feed-Forward Compensation Circuit (4,410,857)
- D. C. Pastore** Multichannel Magnetic Head for a Recorder-Reproducer System (4,408,240)
- W. T. Patton and R. J. Mason** Coaxial Line to Waveguide Coupler (4,409,566)
- D. L. Pruitt** DC-to-DC Switching Converters (4,408,267)
- R. L. Pryor** Protection and Anti-Floating Network for Insulated-Gate Field-Effect Circuitry (4,408,245)
- R. G. Raush and R. A. Alleman** Externally Adjustable Seal and Bearing Structure (4,407,531)
- A. D. Robbi and J. O. Sinniger** Digital Timing System for Spark Advance (4,408,296)
- K. Ruhland** Pseudo Random Number Generator Apparatus (4,408,298)
- F. N. Sechl** Bandpass Filter With an Active Element (4,409,557)
- R. L. Shanley**, 2nd Switching Circuit for Television Receiver On-Screen Display (4,412,244)
- J. Shefer and C. A. Catanese** Electron Gun With Improved Beam Forming Region (4,409,514)
- T. R. Smith** Memory-Type Sync Generator With Reduced Memory Requirements (4,412,250)

E. M. Sutphin, Jr. Apparatus for Testing Linearity of an FM Transmitter (4,412,348)
B. K. Taylor and G. H. Riddle Video Disc Player With Self Calibrating Stylus Translator (4,412,319)
G. E. Theriault Multiband Tuning System for a Television Receiver (4,408,348)
S. Tosima and S. Harada Method for the Evaluation of Solderability (4,409,333)
S. R. Vinekar, J. Hettiger, and K. L. Friedline Burst Gate Keying and Back Porch Clamp Pulse Generator (4,410,907)

November

A. A. Ahmed Plural Output Switched Current Amplifier as for Driving Light Emitter Diodes (4,417,240)
E. J. Alvero and W. R. Kelly System and Method for Determining the Light Transmission Characteristics of Color Picture Tube Shadow Masks (4,416,521)
R. L. Angle Electrically Alterable, Nonvolatile Floating Gate Memory Device (4,417,264)
W. E. Barnette and R. W. Jebens Lens Positioning Controller for Optical Playback Apparatus (4,418,405)
B. F. Bogner Broadband Non-Contacting RF Shielding Gasket (4,414,425)
D. Boetz and M. Ettenberg W-Guide Buried Heterostructure Laser (4,416,012)
J. J. Brandinger Video Disc Pickup Stylus (4,418,407)
W. C. Brooks Electroforming Apparatus for Use in Matrixing of Record Molding Parts (4,415,423)
E. F. Cave and J. J. Cowden Stylus Manufacturing Method (4,417,423)
P. Datta and R. N. Friel Conductive Video Discs (4,416,807)
W. J. Davis Raster-Scanned CRT Display System With Improved Positional Resolution for Digitally Encoded Graphics (4,415,889)
R. A. Dischert Television Display With Doubled Horizontal Lines (4,415,931)
R. A. Dischert Adaptive Reconstruction of the Color Channels of a Color TV Signal (4,417,269)
R. M. Evans Tuning System for a Multi-Band Television Receiver (4,418,428)
R. D. Faulkner, D. V. Henry and D. L. Muth Electron Multiplier Having an Improved Planar Ultimate Dynode and Planar Anode Structure for a Photomultiplier Tube (4,415,832)
R. E. Flory Clamp for Line-Alternate Signals (4,414,572)
W. F. Heagerty, G. T. Caracciolo, and W. F. Gehweiler Radiation Hardened Accessible Memory (4,418,402)
R. N. Hurst Indicator Control Signal Generator for Video Tape Recorder (4,413,288)
K. C. Kelleher Turntable Speed Control (4,417,332)
K. C. Kelleher Video Disc Player With RFI Reduction Circuit Including Sync Tip Clamp (4,418,363)
K. Knop and M. T. Gale Multiple Image Encoding Using Surface Relief Structures as Authenticating Device for Sheet-Material Authenticated Item (4,417,784)
H. G. Lewis, Jr. Digital Color Television Signal Demodulator (4,415,918)
F. D. Marschka Control-Screen Electrode Subassembly for an Electron Gun and Method for Constructing the Same (4,414,485)
J. H. McCusker, B. J. Thaler, and W. H. Tsien Coating Adhesion Testing (4,413,510)
M. W. Muterspaugh Tuning System for a Multi-Band Television Receiver (4,418,427)
G. H. Olsen Semiconductor Light Emitting Device (4,416,011)
A. N. Prabhu and K. W. Hang Air-Fireable Thick Film Inks (4,415,624)
J. J. Prusak and B. P. Patel Method for Molding an Article (4,414,167)
O. H. Schade Jr. Offset Compensation Apparatus for Biasing an Analog Comparator (4,417,160)
R. L. Scheihorn Method of Connecting Surface Mounted Packages to a Circuit Board and the Resulting Connector (4,417,296)
I. Shidlovsky and W. E. Harty High Density Information Disc Lubricants (4,416,789)
C. H. Strolle, T. R. Smith, and G. A. Reitmeyer Calculation of Radial Coordinates of Polar-Coordinate Raster Scan (4,415,928)
J. C. Tallent, 2nd and J. Hettiger Manually Gain Presettable Kinescope Driver in an Automatic Kinescope Bias Control System (4,414,577)
B. K. Taylor Stylus Arm for Video Disc Player (4,418,408)
M. Toda and S. Osaka Photoelectric Drive Circuit for a Piezoelectric Bimorph Element (4,417,169)

- D. D. Vanormer** Method for Preventing Blocked Apertures in a Cathode Ray Tube Caused by Charged Particles (4,416,642)
C. C. Wang and **R. F. Bates** High Density Information Disc (4,414,660)
R. A. Wargo Television Ghost Signal Detection During the Video Information Interval (4,413,282)
D. H. Willis and **R. C. Clayburn** Television Receiver Ferroresonant Power Supply With Permanent Magnet Biasing (4,415,841)
C. M. Wine Video Player Apparatus Having Caption Generator (4,418,364)

December

- T. J. Christopher** and **C. B. Dieterich** Digital on Video Recording and Playback System (4,419,699)
B. J. Curtis and **M. Ebnoether** Reverse Etching of Chromium (4,421,593)
W. Denhollander Horizontal Deflection Circuit With Linearity Correction (4,423,358)
A. R. Dholakia and **V. J. Ruggeri** Grinding Apparatus (4,418,500)
A. R. Dholakia Stylus Lifting/Lowering Actuator With Air Damping (4,423,500)
R. A. Dischert and **C. B. Oakley** Compatible Component Digital System (4,419,687)
W. A. Dischert Method and Apparatus for Rotating a Stylus During Lapping (4,419,848)
J. G. Henderson Television Frequency Synthesizer for Nonstandard Frequency Carrier (4,422,096)
J. E. Hicks Horizontal Deflection Circuit (4,419,608)
S. T. Jolly Method for Forming an Epitaxial Compound Semiconductor Layer on a Semi-Insulating Substrate (4,421,576)
C. J. Kaiser Substrate for Optical Recording Media and Information Records (4,423,427)
H. P. Kleinknecht Automatic Photomask Alignment System for Projection Printing (4,422,763)
H. Kressel and **S. T. Hsu** Memory Array With Redundant Elements (4,422,161)
C. W. Leung, **R. H. Dawson**, **M. A. Blumenfeld**, and **D. P. Blondi** Low Temperature Elevated Pressure Glass Flow/Re-flow Process (4,420,503)
H. G. Lewis, Jr. and **A. Acampora** Digital Signal Processor With Symmetrical Transfer Characteristic (4,422,094)
A. L. Limberg Voltage-Followers With Low Offset Voltages (4,420,726)
P. T. Lin Apparatus for Coating Recorded Discs With a Lubricant (4,421,798)
J. F. McSparran Shock and Vibration Resistant Electrical Switch (4,423,296)
K. S. Reid-Green and **W. Z. Marder** Numerically Controlled Method of Machining Cams and Other Parts (4,423,481)
R. G. Stewart and **M. Mazin** Read Only Memory (ROM) Having High Density Memory Array With On Pitch Decoder Circuitry (4,419,741)
R. G. Stewart and **M. Mazin** Apparatus for Decoding Multiple Input Lines (4,423,432)
M. L. Tarnq Multi-Layer Passivant System (4,420,765)
A. A. Todd Testing Semiconductor Furnaces for Heavy Metal Contamination (4,420,722)
L. C. Upadhyayula Voltage Comparator Using Unequal Gate Width FET's (4,420,743)
A. E. White Apparatus and Method for Automatically Replenishing Liquid and Measuring the Rate of Evaporation of a Liquid (4,418,576)
B. J. Yorkanis and **W. E. Sepp** Delay Circuit Employing Active Bandpass Filter (4,422,052)

AUTHORS

James Andrus joined RCA in 1973. He has been engaged in research into various aspects of surface and thin-film Chemistry. He holds a BS degree in Chemistry from Delaware Valley College, and is now pursuing a degree in Electrical Engineering.



Simon M. Boardman received an Associate degree in Electronics Technology from Temple University in 1961 and a BS in Business Administration from Rider College in 1978. Mr. Boardman worked in the micro-circuit thin-film applications laboratory and thick-film service group at IRC, from 1961 to 1965. From 1965 to 1968 he worked for Fairchild Hiller Corporation in the physical chemistry group, having responsibility for the thin-film services and assisted with the PC facility, doing NASA and defense contracts. Mr. Boardman joined RCA Laboratories in 1968. He has worked on various device development projects and is currently engaged in the development of polymer thick-film materials.



Mr. Boardman is a member of ISHM.

Dan Botez received the BS degree (with highest honors) and the MS and PhD degrees in Electrical Engineering from the University of California, Berkeley, in 1971, 1972, and 1976, respectively. His doctoral studies were concerned with the characteristics of layers deposited over preferentially etched channels in GaAs, as well as with novel optical devices made possible by this method. For one year following graduation, he was a Postdoctoral Fellow at the IBM Watson Research Center. In 1977 Dr. Botez joined the Technical Staff at RCA Laboratories, Princeton, NJ, where his work resulted in "thick-window" high-radiance surface-emitting LEDs and in the development of a novel type of single-mode-stabilized cw diode laser: the constricted double-heterostructure (CDH) laser. The CDH laser has demonstrated cw and pulsed operation up to the highest ambient temperatures ever reported and represents the least temperature sensitive diode laser commercially available. His recent work has resulted in the constricted double-heterojunction large-optical-cavity (CDH-LOC) laser, which to date is the most powerful single-mode semiconductor cw laser and has made possible the optical recording of information at the highest data rates ever achieved.



In 1979 he received an RCA Laboratories Outstanding Achievement Award for contributions to the development of a high-density optical recording system employing an injection laser. In 1982 he was appointed a Research Leader in the Opto-Electronics group. Dr. Botez holds ten patents and has seven patents pending. He is a member of Phi Beta Kappa and the IEEE.

Donald J. Channin received his BS degree from Case Western Reserve University in 1964 and his PhD degree from Cornell University in 1970. His PhD thesis was based on high-frequency phonon studies in solids at cryogenic temperatures, in which he used thermal pulse and microwave techniques. In 1970, Dr. Channin joined RCA Laboratories, Princeton, NJ. There he worked first on acousto-optic laser light deflection and modulation. Subsequent work on optical waveguides led to the development of several electro-optic waveguide devices and the analysis of scattering phenomena. His work on liquid crystals has included the development of an integrated-circuit inspection process and a new technique for scanned displays.



During 1977-1978 Dr. Channin spent a year at the University of São Carlos, Brazil, as a Visiting Professor. His research there involved acousto-optic effects in liquid crystals. Since his return to RCA Laboratories he has been doing research on modulation and high-frequency effects in injection lasers and has been responsible for developing components and systems for optical communications. He has participated in efforts to establish standards in the field of fiber optics and is chairman of a JEDEC committee on fiber-optic transducers. In 1983, he was appointed Research Leader in the Optoelectronic Devices and Systems Research group.

Dr. Channin received an RCA Laboratories Outstanding Achievement Award in 1973 and 1975. He has published many technical papers and holds nine U.S. patents. He is a Senior member of the IEEE and a member of the American Physical Society, the Optical Society of America, Sigma Xi, and Tau Beta Pi.

Kenneth W. Hang studied Ceramic Engineering at the University of Illinois, graduating with a BS degree in 1966, an MS degree in 1967, and a PhD degree in 1970. He then joined RCA Laboratories, Princeton, NJ, as a Member of the Technical Staff, specializing in glass research, both synthesis and materials measurements. Promoted to Senior Member of the Technical Staff in 1983, he is associated with the Optical Systems and Display Materials Research Laboratory. Dr. Hang has been responsible for the synthesis and characterization of glasses for passivating the surface of silicon power devices. He also developed a process for passivating power transistor glass. He invented and developed a glass ceramic coating on steel that has application as a thick-film hybrid circuit substrate. In 1972, 1978, and 1982 he shared RCA Laboratories Outstanding Achievement Awards.



Having published several papers on ferroelectric ceramics, Dr. Hang also wrote and presented a paper on the physical and chemical properties of alkali-containing glasses subjected to surface ion depletion at blocking anodes. He holds 10 U.S. patents.

Shigeo Harada joined RCA Research Laboratories Inc., Tokyo, in 1966, where he performed research in the field of material synthesis, crystal growth and display materials. His recent area of interest has been solder evaluation techniques. In 1982, Mr. Harada transferred to Tokyo Laboratories, Sharp Corporation.



Sheng T. Hsu received the B.S. degree in electrical engineering from National Taiwan University, Taipei, Taiwan, in 1958, the M.S.E.E. degree from National Chiao-Tung University, Hsienchu, Taiwan, in 1960 and the Ph.D. degree in electrical engineering from the University of Minnesota, Minneapolis, in 1966. From 1966 to 1970, he was with Fairchild Semiconductor Research and Development Laboratory, Palo Alto, California, as a Member of the Technical Staff. From 1970 to 1972, he was an Assistant Professor of the Department of Electrical Engineering, University of Manitoba, Winnipeg, Man., Canada. He is now a staff member of RCA Laboratories, Princeton, N.J., working on semiconductor devices and VLSI technologies.



Edward O. Johnson received a BSEE degree from Pratt Institute of Brooklyn in 1948 and attended graduate courses at the Swiss Federal Institute of Technology and at Princeton University. In 1948 he joined RCA Research Laboratories where he worked in plasma physics to help develop gas plasma analogues to the transistor, double probe methods which have been widely used in ionospheric and plasma research, semiconductor surface measurement techniques, and concepts for understanding the limits of solid-state device performance. In various managerial capacities from 1959 to 1972, he was with the Solid-State and Tube Products Divisions, and from 1973 to 1975 with Licensing Operations. From 1975 to 1982 he was director of the RCA Research Laboratories in Tokyo, Japan. In 1982 he transferred to Corning Research, Inc., in a similar capacity.



In 1953, with W. M. Webster, he received the IEEE Editor's Award, and in 1960 the Eta Kappa Nu Recognition. In 1966 he was a member of the U.S. Department of Commerce Panel on Electric Automobiles. He has received several RCA achievement awards and has over 30 issued patents.

Richard B. Maynard received the BS degree in Chemistry from Western Washington State University in 1974. In 1979 he received his PhD degree in Inorganic Chemistry from the University of Hawaii at Manoa. His doctoral studies dealt with synthetic organouranium chemistry and bio-inorganic chemistry of vitamin B₁₂. For two years following graduation, he was a post-doctoral Research Associate at the University of Virginia where he synthesized and characterized a variety of metallacarborane and -borane compounds. In 1981 Dr. Maynard joined RCA Video Components and Display Division, Lancaster, Pa, as a Member Technical Staff in the Mask Processes and Materials Engineering Group. He is currently involved with the chemical processes utilized in the production of shadow masks for color picture tubes.



Dr. Maynard has authored or co-authored approximately twenty-five papers, mainly in the areas of organometallic and inorganic chemistry, and is a member of the American Chemical Society.

John J. Moscony received a BS and MS in Chemistry from St. Joseph's College, and a PhD in Chemistry from the University of Pennsylvania. He held a David Sarnoff Fellowship at the University of Pennsylvania from 1962–1965. Dr. Moscony joined RCA in 1957 and from that time until 1962, he worked on materials development projects related to thermoelectric and thermionic energy converters. In 1965 he joined the Chemical and Physical Laboratory at RCA Lancaster. As a Senior Engineer and Engineering Leader, he worked on many materials and process programs associated with the production of color television picture tubes. Some of his successful projects include work on vacuum processing, high voltage stability studies, and advanced development work on phosphors, glass, frit, getters, implosion protection, and shadow masks. Since 1979, Dr. Moscony has been Manager of the Mask Technology group of the Lancaster Technology Transfer Laboratory, and Leader Technical Staff of the Materials and Process Mask Group.



He is a member of the American Chemical Society and the American Association for the Advancement of Science.

Lubomyr S. Onyshkevych received the BEE degree from The City University of New York in 1955, the MSEE degree from the Massachusetts Institute of Technology in 1957, and the EE degree (an industrial equivalent of a doctorate) from MIT in 1962. From 1955 to 1957, he worked at MIT's Research Laboratory of Electronics in the area of multiaperture magnetic logic. In 1957, he joined RCA Laboratories, Princeton, NJ, investigating magnetic logic and memory systems, parametric oscillators, and tunnel diodes. He received an RCA Laboratories Outstanding Achievement Award in 1959. In 1959, he returned to MIT to continue his studies and during 1961–1963, worked at MIT's Lincoln Laboratories on thin-magnetic-film memories. Mr. Onyshkevych rejoined RCA Laboratories in 1963. Since then he has been working on ultrasonics, magnetic bubble memories, sonic-film memories, surface-wave acoustic devices, ferroresonance, TV deflection circuits, porcelain-steel substrates, electronic packaging, and TV receiver mechanical design. In 1967, he received another RCA Laboratories Outstanding Achievement Award and, in 1979, he was appointed Head, Electronic Packaging Research group.



Mr. Onyshkevych is a member of the Institute of Electrical and Electronics Engineers, Tau Beta Pi, Sigma Xi, and Eta Kappa Nu. He has published numerous papers and holds 12 U.S. patents and several foreign patents.

Ashok N. Prabhu earned a B. Tech. degree in Metallurgical Engineering from the Indian Institute of Technology, Bombay, in 1970. At Purdue University he received an MS degree in 1972 and a PhD degree in 1975, both in Metallurgical Engineering. His PhD thesis involved studying the correlation between the electrical properties and the microstructure in RuO₂-containing thick-film resistors. During 1975–76, at Northwestern University, Dr. Prabhu worked on ionic conductors as an IBM Research Fellow. He joined Engelhard Industries in 1976 as a Senior Applications Metallurgist and was involved in the research and development work in hybrid microelectronic



materials and processes, especially thick film resistors, conductors, dielectrics and specialty metallizations. Since joining RCA Laboratories, Princeton, NJ, in 1979, Dr. Prabhu has continued his work on microelectronic materials, studying interactions between thick-film materials and porcelain-coated substrates. He was responsible for formulating and developing materials for producing process-induced components on the RCA porcelain-coated metal substrates. He has also worked on polymeric resistor materials and, more recently, has been involved in the low-cost, high-density, fabrication and assembly processes of printed-circuit boards, as well as studies of metallized thermoplastics, and the interconnections between surface-mount IC packages and various substrates.

Dr. Prabhu holds nine U.S. patents. He has authored or coauthored 12 technical papers. He is a member of the IEEE, International Electronic Packaging Society, the International Society for Hybrid Microelectronics, and a former member of Sigma Xi.

L. T. Sachtleben received his B.Sc. Degree in Physics and Mathematics from Antioch College. His work in optics began in the field of sound motion pictures, from which point he has continued as a generalist in optics at the RCA plants in Camden and Indianapolis. He has written or co-authored numerous published papers, and 47 patents have been issued to him. He is a member of SMPTE, OSA, AAPT, and NCTM.



Margaret H. Saunders graduated from Millersville University in 1977 with a B.S. degree in Physics. She joined the RCA Picture Tube Division in 1977 in the Process and Materials Development Group, where she worked on shadow mask development and manufacturing support. She received the Technician of the Year Award in 1979 for Outstanding Contributions to Mask Manufacturing Technology. At present she is working on photochemical machining methods for new materials and computer modeling for scrap reduction and increased productivity in Mask Manufacturing.



Stefan A. Siegel received a BSEE degree summa cum laude in 1974 from the Polytechnic Institute of New York. He has done graduate work at the University of Pennsylvania and is completing his MSEE degree at Rutgers University. Mr. Siegel joined RCA Laboratories, Princeton, NJ, in 1979. He has designed fiber-optic transmitter and receiver modules for both high-speed digital communication systems and video-frequency analog links. His background in microwave techniques has enabled him to assist in the design and development of a 2- to 6-GHz analog fiber-optic link. His work has also included the development of fiber coupling and lensing techniques.

He is the author or coauthor of several technical papers, holds two U.S. patents, and is a member of Sigma Xi and Eta Kappa Nu.



Soitiro Tosima received the B.Sc. degree in physics from Kyushu University in 1951, and the D.Sc. degree in physics from Osaka University in 1962. From 1953 to 1961, he was a Research Associate in the Physics Department of Kyushu University. He joined RCA Research Laboratories, Tokyo, in 1961. In 1964, he spent six months as a visiting research scientist at RCA Laboratories in Princeton. In 1965, Dr. Tosima became manager of the Applied Physics Group. His principal areas of interest have been the theories of transport phenomena in semiconductors, semimetals, and ferromagnetic semiconductors, particularly at high electric fields; instabilities in solid state plasmas; and magnetic bubbles. More recently his areas of interest have been high intensity surface acoustic waves and the physics of the soldering process. In 1982 he transferred to Corning Research, Inc., in Japan.



